SYNTHESIS, SELF-ASSEMBLY AND APPLICATIONS OF TRIBENZOPENTAPHENE DERIVATIVES AND TRIPHENYLENE-BASED CONJUGATED FOLDAMERS

A DISSERTATION IN
Chemistry
And
Pharmaceutical Sciences

Presented to the Faculty of the University
of Missouri-Kansas city in partial fulfillment of
the requirements for the degree

DOCTOR OF PHOLOSOPHY

by
CHING-EN CHOU

M.S. University of Missouri-Kansas City, 2013
B.Eng. Tamkang University 2003

Kansas City, Missouri
2013

SYNTHESIS, SELF-ASSEMBLY AND APPLICATIONS OF TRIBENZOPENTA-PHENE DERIVATIVES AND TRIPHENYLENE- BASED CONJUGATED FOLDAMERS

Ching-En Chou, Candidate for Doctor of Philosophy Degree

University of Missouri-Kansas City, 2013

ABSTRACT

Polycyclic aromatic hydrocarbons (PAHs) are interesting discotic liquid crystalline materials. Their often planar or near-planar geometry and extended π-delocalization render them appealing π-π stacking building blocks which can be utilized to dictate controlled self-assembly processes. In addition, the potentially high charge mobility along the stacked PAH column may find applications in sensors, field effect transistors and photovoltaic cells. In this dissertation, efficient synthetic approaches to tribenzopentaphene (TBP) derivatives are reported and their optical, electrochemical, self-assembly, and photovoltaic properties are studied. It is shown that TBP derivatives are good electron donors which, when coated on pre-grown perylenediimide (PDI) nanofibers can significantly enhance the photocurrent response of the PDI nanofibrils. The peripheral substituents on the TBP core are found to exhibit significant effect on its self-assembly properties which in turn affects the photocurrent response of the PDI/TBP heterojunction nanofibrils. Heterjunction solar cells using TBP derivatives as the donor and PDI or PCBM as the acceptor have also been fabricated and a power conversation efficiency of 0.12% has been achieved.

Conjugated oligomers and polymers which can self-organize into a helical conformation have been extensively studied. Such studies have not only led to much better understanding of the principles behind noncovalent folding, but also brought about a number of exciting applications from selective and specific guest binding, functional group organization, to reactive sieves. The major driving forces responsible for the folding of π-conjugated systems are π-π stacking and solvophobic interactions. The strength of the π-π interaction depends on the size and the electronic nature of the aromatic systems. In general, the larger the size of the planar aromatic system is, the stronger the π-π interaction will be. Interestingly, studies on conjugated foldamers have so far been limited to single-ring aromatic systems, in which the mere existence of π-π interactions is questionable. Polycyclic aromatic systems (PCA), as far as we know, have not been utilized in conjugated foldamers. It is envisioned that, with PCAs in the conjugated polymer backbone, the polymer will not only exhibit much stronger propensity for folding due virtually to their stronger π-π stacking interactions, but also may lead to conjugated systems with very interesting electronic and optical properties. In the second part of this dissertation, we report the synthesis and optical properties of triphenylene-containing conjugated foldamers. Systematic optical property studies show that such polymers indeed fold in a variety of solvents. Depending on the solvents, the polymer may also adopt a random coil conformation or interchain aggregation. Among the three conformations, the folding conformation is found to exhibit the highest fluorescence quantum yield.

APPROVAL PAGE

The undersigned, appointed by the Dean of the School of Graduate Studies, have examined the dissertation titled "Synthesis, Self-Assembly, and Applications of Tribenzopentaphene Derivatives and Triphenylene Based Conjugated Foldamers." Presented by Ching-En Chou, candidate for the Doctor of Philosophy Degree, and hereby certify that in their opinion it is worthy of acceptance.

Supervisory Committee

Zhonghua Peng, PhD., Committee Chair
Department of Chemistry

James R. Durig, PhD.
Department of Chemistry

Nathan A. Oyler, PhD.
Department of Chemistry

Kun Cheng, PhD.
Department of Pharmaceutical Science

Da-Ming Zhu, PhD.
Department of Physics

CONTENTS

ILLUSTRATIONS

ILLUSTRATIONS

TABLE

ACKNOWLEDGEMENTS

I would like to express my sincere gratitude and deepest appreciation to my research advisor and my committee chair, Professor Zhonghua Peng, for giving me a great opportunity to join his research group. He has trained and taught me how to work independently and think logically. He always gave patient guidance, enthusiastic encouragement and useful critiques of my research work. Without his guidance and persistent help this dissertation would not have been possible.

I would also like to extend my thanks to other dissertation committee members, Professor James R. Durig, Professor Nathan A. Oyler, Professor Da-Ming Zhu, and Professor Kun Cheng, for their professional guidance and valuable support in reviewing my dissertation.

I would like to offer my special thanks to Professor Ling Zang and Dr. Yanke Che at the University of Utah, for photoconductivity measurements, Professor Andrew Keightley at the School of Biological Science, UMKC for MALDI-TOF mass measurements, Dr. Vladimir M. Dusevich at the School of Dentistry, UMKC, for SEM measurements. I am also thankful for Dr. Yong Li at the Department of Chemistry, UMKC for Photovoltaic Device fabrications. My thanks also go to Mrs. Florence Middleton at the Department of Chemistry, UMKC for proofreading my dissertation.

I wish to thank all the members of the Peng Group, both past and present: Dr. DeGang Wang, Dr. Mahuya Bagui, Mr. Jeffrey Hsu, Dr. Sanjiban Chakraborty, Mr. Shaohua Li, Miss Lu Jin, Mr. Kuldeep Chandrashekhar Shetye. I enjoyed working with them.

Last but more importantly, I am particularly grateful to my parents, Mr. Yin-Kun Chou, Mrs. Mei-Hua Wu, and my elder sister Mrs. Yi-Ling Chou who always give me the greatest support and unconditional love.

Dedicated to my parents

CHAPTER 1

SYNTHESIS AND CHARACTERIZATION OF NEW DISCOTIC LIQUID CRYSTAL TRIBENZOPENTAPHENE DERIVATIVES

1.1 Introduction

1.1.1 A Brief History of Discotic Liquid Crystals

Liquid crystals (LCs) were serendipitously discovered toward the end of nineteenth century when European scientists observed unusual behavior via polarized light passing through liquid-like biological materials. Rudolph Virchow, C. Mettenheimer and G. Valentin were the first group of scientists who found the unique liquid crystal behavior in biological systems, but unfortunately they did not know then that this promising phenomena was a "new" state of matter.[1]

In 1888, Friedrich Reinitzer, an Austrian botanist, was studying experiments on a cholesterol-based substance (Figure1.1), trying to find the correct formula and molecular weight of cholesterol. When he tried to determine the melting point of cholesterol, he observed two distinct melting points. It became a cloudy liquid at 145.5 ^{o}C and this opaque liquid turned clear at 178.5 ^{o}C. Although Reinitzer could not explain the phenomenon he observed, his work and the following reports caught the attention of other scientists, especially Otto Lehmann.[2] Otto Lehmann, a professor of physics in Germany, continued liquid crystal research. He was the first person to study liquid crystals using a microscope that included polarizers and a hot stage. He determined that some molecules do not melt directly, but possess a specific phase which has the ability to flow like a liquid while maintaining the molecular structure and optical properties of a

solid crystal. Lehmann first called them "soft crystals", later he referred to them as "crystalline fluids". When he realized that the opaque phase was a homogeneous phase of matter whose properties were between liquid and solid, he began to name this new state of matter liquid crystal (LC) in 1889. He also observed that LCs enable orientation in a certain direction as a solid surface came in contact with LCs. This discovery is the key to the development of liquid crystal displays. Although he is not the first scientist to discover LCs, he made the key contribution to this field.

Lehmann's work, however, was not widely accepted then by other scientists. Similar researches occurred at the same time in Germany and France. In 1907, an important German chemist, Daniel Vorlander, published a book entitled "*Influence of molecular configuration on the crystalline-liquid state"*,[3] in which he stated that "…*the crystalline-liquid state results from a molecular structure which is as linear as possible*". Compounds which exhibited LC behavior were rodlike molecules, now called calamitic molecules. Over the next seven decades linear rodlike molecules were widely accepted as the major liquid crystal mesogen. In 1977, when a novel display technology based on rodlike liquid crystals was about to be commercialized and the general belief that only rodlike molecules can form LCs was prevalent, Sivaramakrishna Chandrasehar and coworkers reported that not only rod-like molecules, but also disc-like molecules can form LC phases. He wrote "*what is probably the first observation of themotropic mesophism in pure, single-component systems of relatively simple plate-like, or more appropriately disc-like, molecules.*"[4-8] They synthesized some benzene hexa-n-alkanoates (Figure1.1) and used optical, thermodynamic, and x-ray analysis to confirm that these materials formed similar LC phases as rod-like molecules. This created a whole new field

of LC research and attracted many scientists to continue the fascinating work. Soon after this study by Chandrasekhar, two French scientists, Dubois and Levelut, further showed that liquid crystals can be formed by other disc-like molecules.[8]

Calamitic Liquid-Crystal Display (LCD) nowadays plays an important part of our daily life. While it seems that discotic liquid crystals cannot compete with their rodlike counterparts in terms of electrooptic performance, the unique structural and electronic features of discotic liquid crystals create a completely different types of possible applications such as molecular electronics and high-efficiency organic photovoltaics (see more detailed discussion in chapter two).

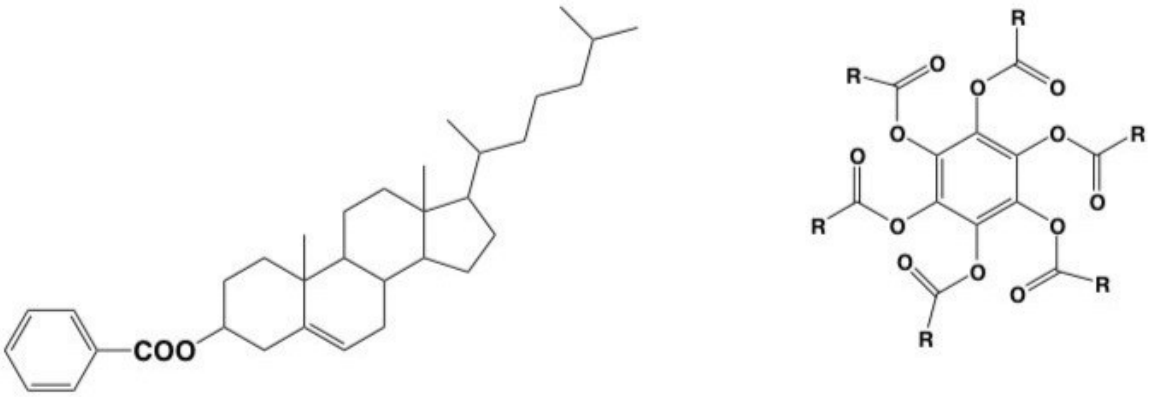

Cholesterol **Hexa-n-alkanoate**

Figure 1.1. The first discovered rod-like and disc-like LC molecules.

1.1.2 Classification of Liquid Crystals

There are a number of different ways to classify LCs. Based on the molar mass of the constituent molecules, there are monomeric, oligomeric (low molar mass) and polymeric (high molar mass) LCs; Based on how the liquid crystalline phases are formed, there are lyotropic (by adding solvent) and thermotropic (by heating to various temperature) LCs; Based on the nature of the constituent molecules, there are organic, inorganic, and organometallic LCs; Based on the physical shape of the molecules, there are rod-like, disk-like, banana-like LCs; Based on the orientation and organization of molecules in the liquid crystalline phase, there are nematic, smectic, columnar, helical, etc. phases. Figure 1.2 summarizes the various LC classifications. The most commonly used LC classification is thermotropic LCs (phase formation due to temperature) lyotropic LCs and amphotropic LCs ((both thermotropic and lyotropic).[10]

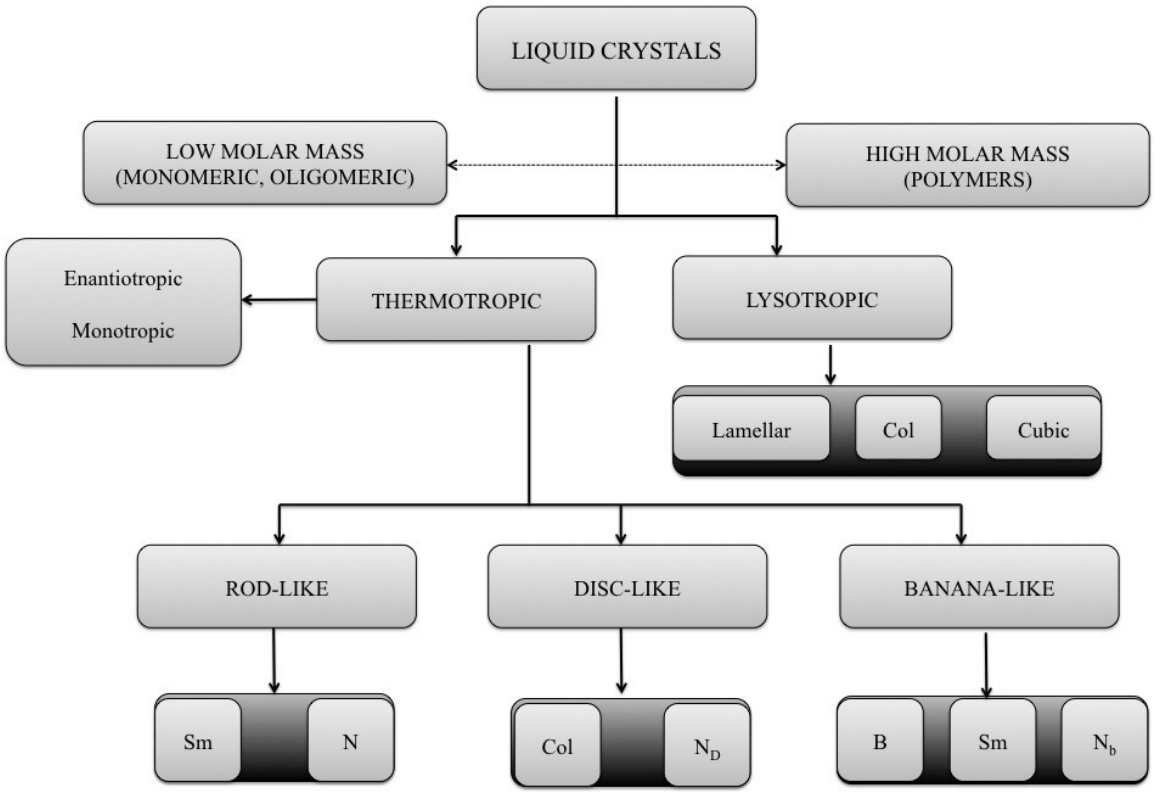

Figure 1.2. Classification of LCs.

1.1.3 Description of Discotic Liquid Crystal

Disk-like molecules form discotic liquid crystals which are quite different from LCs formed by rod-like molecules. The most important feature of the disk-like molecule is that it can spontaneously self-assemble into a 1D structure, which can further self-organize to various 2D lattices; the third dimension has no translational order (Figure 1.3).

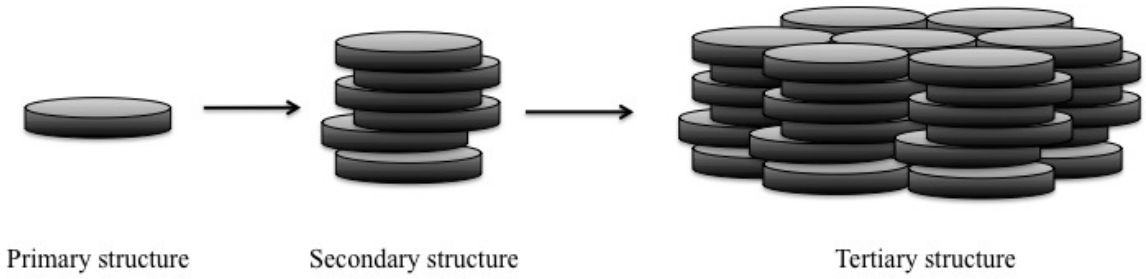

Figure 1.3. Self-assembly and self organization of discotic LCs.

Mesophases of the disk-like molecules can typically be classified into four types: (1) nematic, (2) smectic, (3) columnar, and (4) cubic. The major mesophases of disk-like molecules are usually the columnar meophase, followed by the nematic mesophase, whereas smectic and cubic mesophases are rarely observed. In most cases, a disc-like molecule forms only one type of mesophase. However, a few examples showing polymorphism have been reported.[11] It is worth noting that although columnar mesophases are the most common characteristics in disk-like molecules, they are not unique to discotic molecules. Discotic LC mesogens are typically made of a central

discotic core, with a number of saturated alkly chains. The liquid crystallinity results from the microsegregation of the two constituents: the crystalline character is built up by the discotic conjugated core interaction while the liquid character comes from the melting of the saturated alkyl side chains. Such discotic LCs spontaneously arrange into 1D columns, and these columns can orient easily. The discotic LC mesophase is sensitive to subtle changes in the number, size and nature of the lateral chains as well as the central core. A general template for discotic mesogens is shown in Figure 1.4.[16,55]

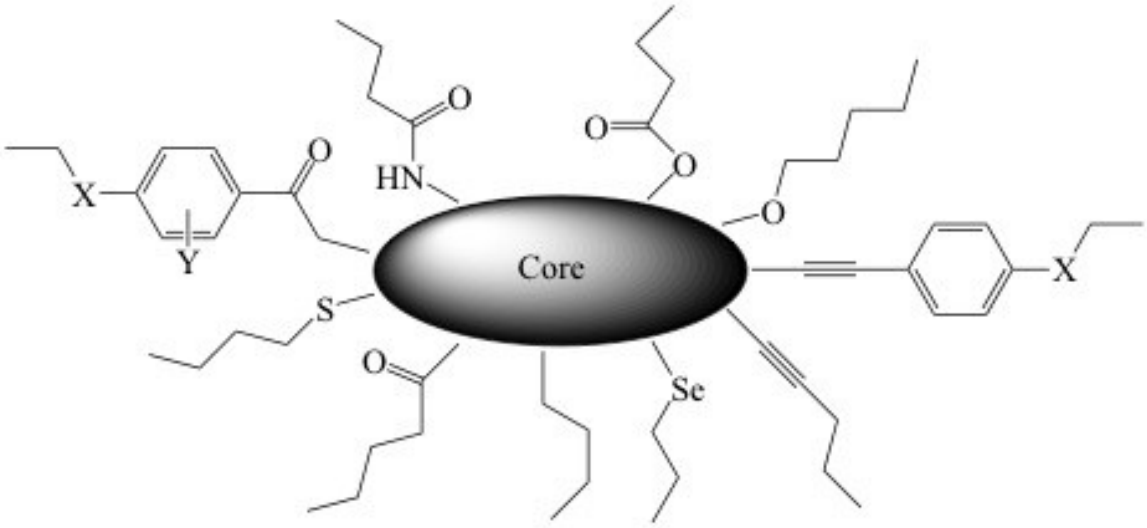

Figure 1.4. General template for DLC molecular architecture.[55]

1.1.4 Overview of Discotic Liquid Crystals

Early studies of discotic molecules began with the smallest possible aromatic core such as benzene and triazine.[9] It soon became evident that larger cores prone to more efficient π-stacking are necessary, variation of the size of the conjugated core is one of the major aspects explored so far in the design of discotic mesogens.[9] Through the years, numerous monomeric discotic mesogens have been studied. Until now, over 60 different cores and about 3000 derivatives of discotic liquid crystals have been synthesized. Some of the most common columnar liquid crystals, which consist of a rigid central core are shown in the Figure 1.5a. Some of the common discoid cores include benzene,[12] pyridine,[13] triazine,[12] triphenylene,[185] diazatriphenylene,[14] hexa-azatriphenylene,[15] pyrene,[158] dibenzochrysene,[159] dibenzonapthacene,[160] tristriazolotriazine,[161] rufigallol,[179] truxen,[181] triazatruxene, or triindole,[197] tricycloquinazoline,[198] hexa-azatrinaphthylene (HATNA),[199] perylene diimide,[47] coronene diimide,[200] phthalocyanine (Pc),[201] pophyrin,[202] , and hexa-peri-hexabenzocoronen (HBC).[130-131]

Compared with other discotic liquid crystal molecules, hexaalkyl hexa-peri-hexabenzocoronene (HBC) has drawn particular attention because of its high charge carrier mobility. Research on HBC derivatives has paved the way for other very large liquid crystalline polycyclic aromatic hydrocarbons (PAHs) shown in Figure 1.5b. In 2008, Mullen's group has successfully synthesized discotic liquid crystals of large aromatic polycyclic hydrocarbon cores which contain 24 to 132 aromatic carbon atoms and can be viewed as graphite subunits. This important milestone has stimulated further research developments in the field of organic electronics.

a)

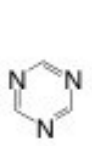

Triazine

Triphenylene

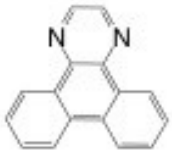

Diazatriphenylene

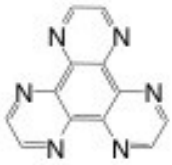

Hexaazatriphenylene

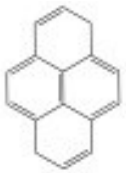

Pyrene

Dibenzochrysene

Dibenzonapthzcene

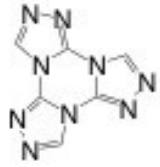

Tristriazolotriazine

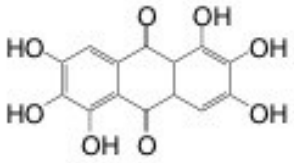

Rufigallol

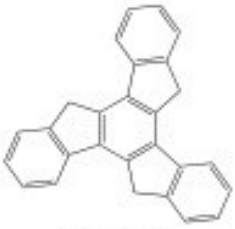

Truxene

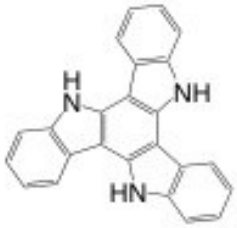

Teiazatruxene/ Triindole

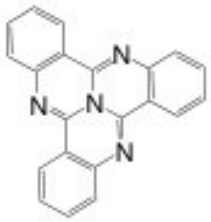

Tricycloquinazoline

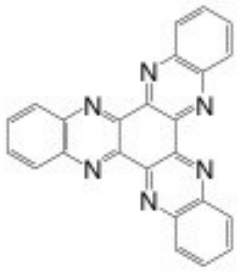

Hexaazatrinaphthylene HATNA

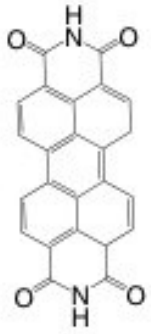

Perylene diimide

Coronene diimide

Phthalocyanine

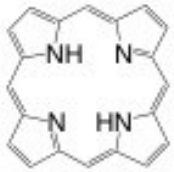

Porphyrin

b)

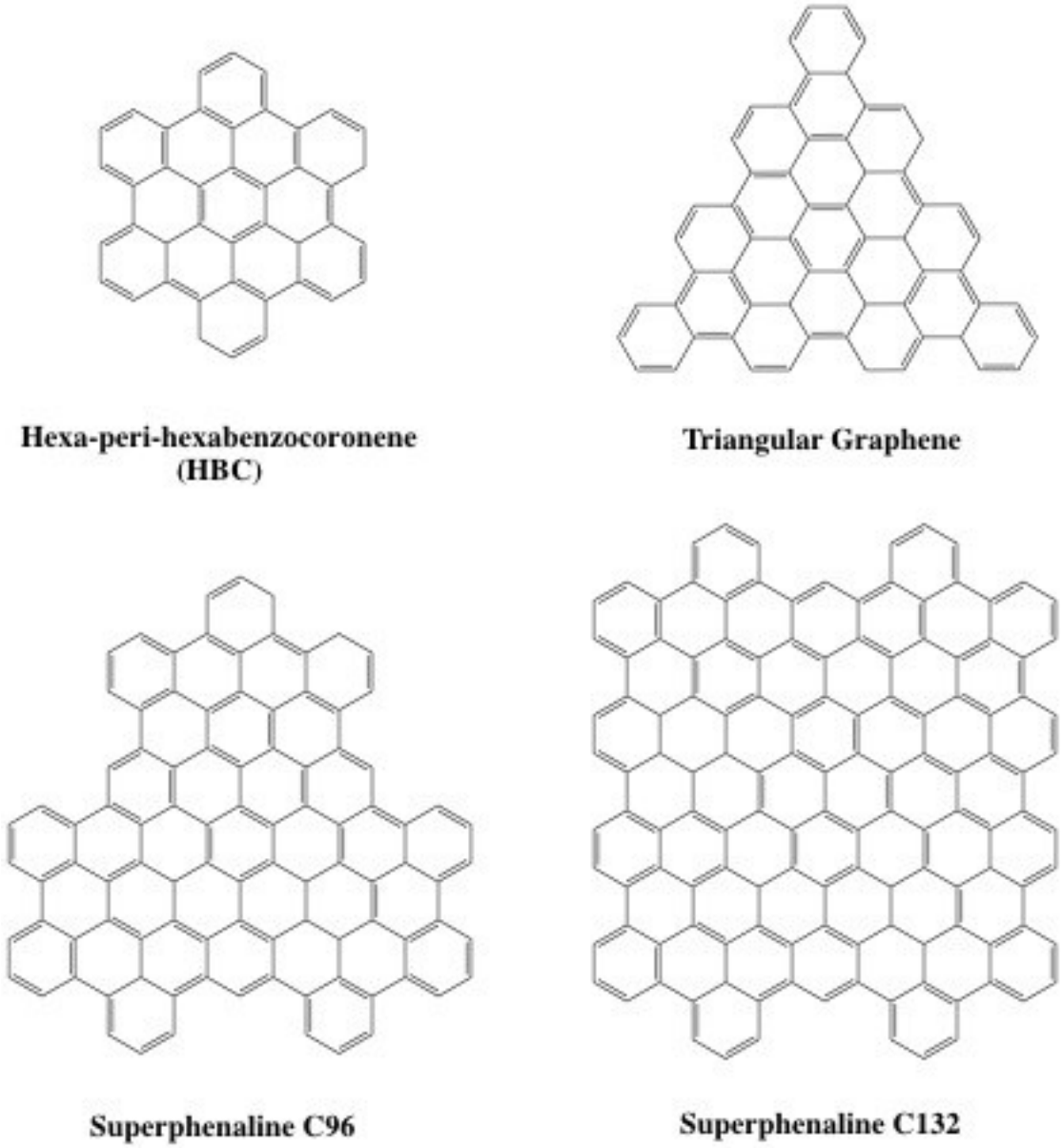

Figure 1.5. a) Some selected core units for columnar discotic liquid crystals, b) Superphenalene-based discotic liquid crystals.

1.2 Objectives

Among the various cores shown in Figure 1.5, the most extensively studied core system is triphenylene (TP). This symmetric polycyclic aromatic hydrocarbon (PAH) has been known and systematically studied for more than a century.[17] Another important common discotic mesogen is hexa-peri-hexabenzocoronene (HBC), one of the largest and highly symmetrical all-benzenoid PAHs. HBC and its derivatives are appealing because many of the proposed application potentials of discotic liquid crystals such as sensors, field effect transistors, photovoltaic solar cells have been successfully demonstrated.[18-25] While a number of PAHs such as triphenylenes, hexabenzocoronenes, etc., have been extensively studied as molecular electronic materials, derivatives with a tribenzopentaphene (TBP) core have drawn little attention.[26-28] In this chapter, we report the synthesis and characterization of four new TBP derivatives whose structures are shown in Figure 1.6. Their optical, electrochemical, self-assembly, and thermal features were comparatively studied.

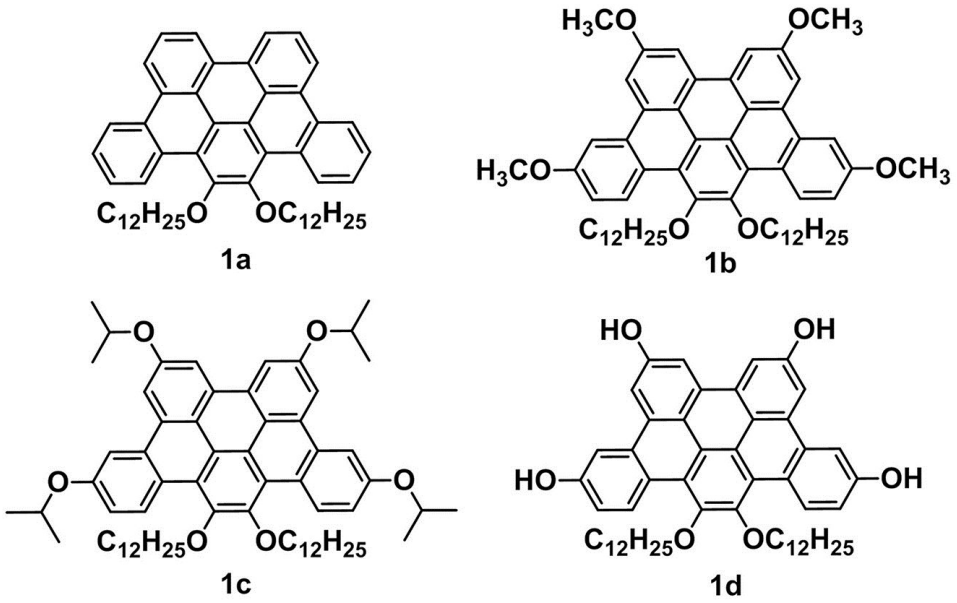

Figure 1.6. Four tribenzopentaphene derivatives.

1.3 Synthesis of Tribenzopentaphene (TBP) Derivatives

All four compounds have two dodecyloxy chains at the bay positions which make them soluble in common organic solvents, even if there is no other substituents (Compound **1a**).[25] Compounds **1b** and **1c** bear four methoxy and isopropoxy groups, respectively, while compound **1d** has four hydroxyl groups around the periphery. Compound **1a** was synthesized first, because to date there is no alkoxyl substituted TBP reported in the literature. Scheme 1.1 shows the synthesis of compound **1a**. The commercially available pyrocatechol was synthesized first by 1-bromododecane to give compound **2**. It was then subjected to an iodination reaction to realize 1,2-diiodo-4,5-bis(dodecyloxy)benzene or compound **3**. In a separate synthesis, a biphenyl boronic acid derivative (compound **4**) was synthesized from bromo-biphenyl. The cross-coupling reaction of compounds **3** and **4** was performed in toluene under conventional Suzuki-

Miyaura reaction conditions in the presence of a Pd(0) catalyst to produce compound **5** in 49% yield. The tribenzopentaphene core or compound **1a** was accomplished by oxidative cyclization of compound **5** using $FeCl_3$ as the oxidizing agent. [33-34] It is worth noting that under longer reaction time and using more $FeCl_3$ led to chlorinate side products. The best results were obtained by using 10 equivalents of $FeCl_3$ in a nitromethane/dichoromethane solvent mixture at 0 °C.

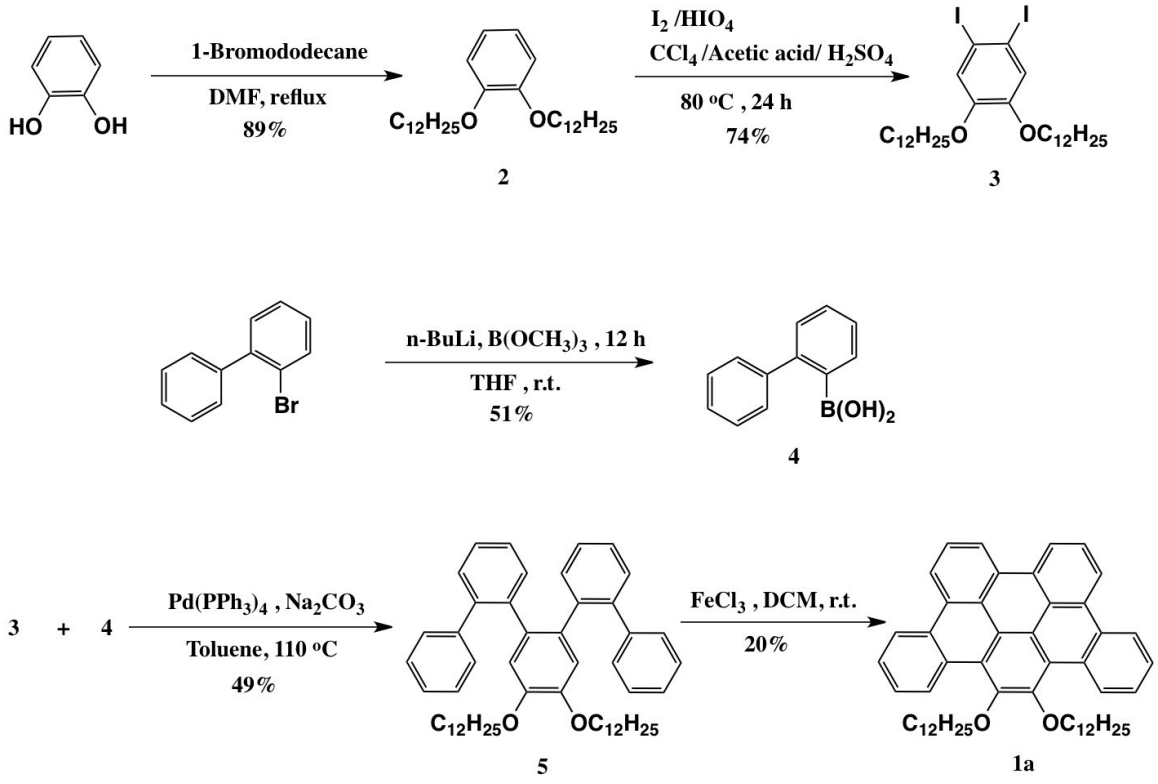

Scheme 1.1. Synthesis of tribenzopentaphene.

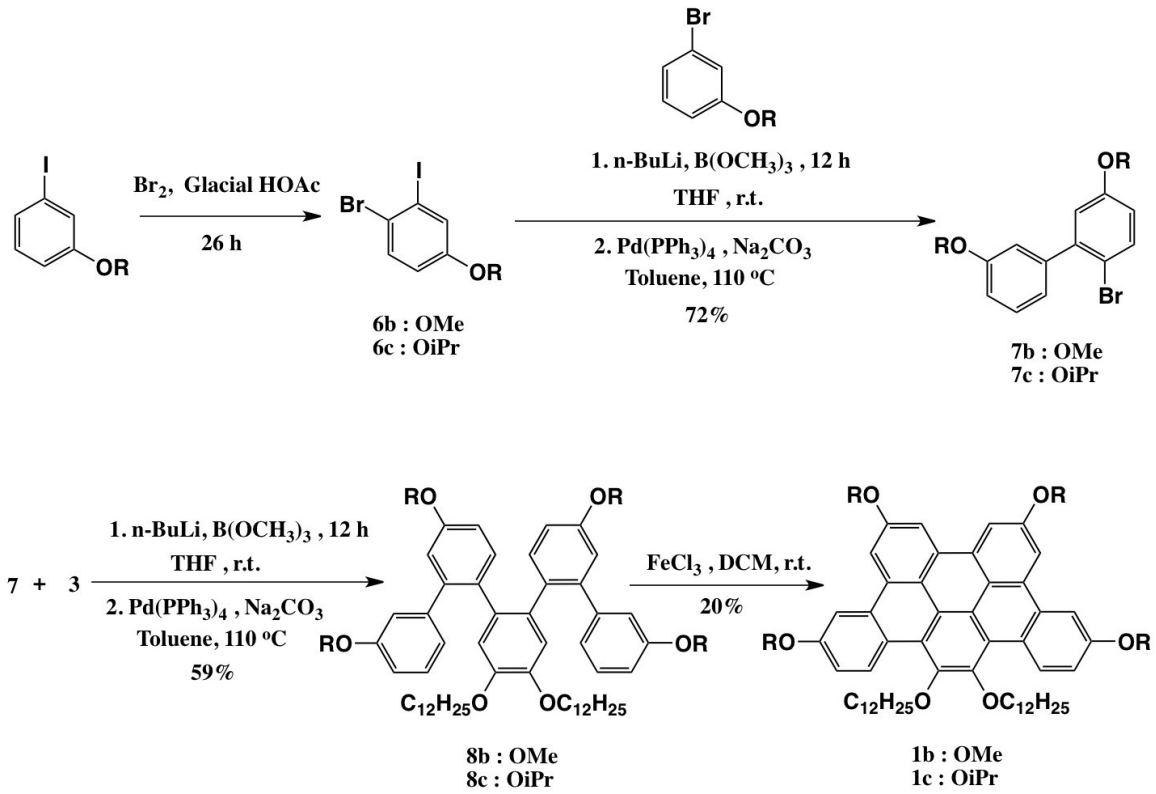

Scheme 1.2. Synthesis of methoxy and isoproxy substituents tribenzophentaphene.

Compounds **1b** and **1c** were synthesized by a similar route (Scheme 1.2). The key steps are the Suzuki-Miyaura coupling of biarylboronic acid derivatives (**7b**, **7c**) with 1,2-bis(dodecyloxy)-4,5-diiodobenzene (compound **3**) to form o-quinquephenyls (**8b**, **8c**)[29-32] and the subsequent Scholl oxidative cyclization to yield the TBP core.[33-34] The Suzuki-Miyaura coupling went smoothly and could proceed directly from 2-bromobiaryl derivatives (**7b**, **7c**) as a one-pot synthesis with good overall yields (around 50%).[35] The Scholl reactions of alkoxy substituted oligophenylenes are often complicated as previously shown by many researchers.[36-37] Competing side reactions such as incomplete cyclization, electrophilic aromatic halogenation, inter-molecular oxidative coupling, etc., often lead to a messy reaction mixture from which the pure desired product is difficult to isolate. After experimenting with different oxidants ($MoCl_5$,[38] $FeCl_3$, and DDQ[39]),

solvent combinations, oxidant/substrate ratios, and temperatures, the best results were obtained using 5 equivalents of $FeCl_3$ in a nitromethane/dichoromethane solvent mixture at 0 °C. Under these conditions, compounds **1b** and **1c** were obtained in 20-30% yields. Compound **1d** was synthesized from **1c** in excellent yields using B-bromo-9-BBN as the dealkylation reagent.

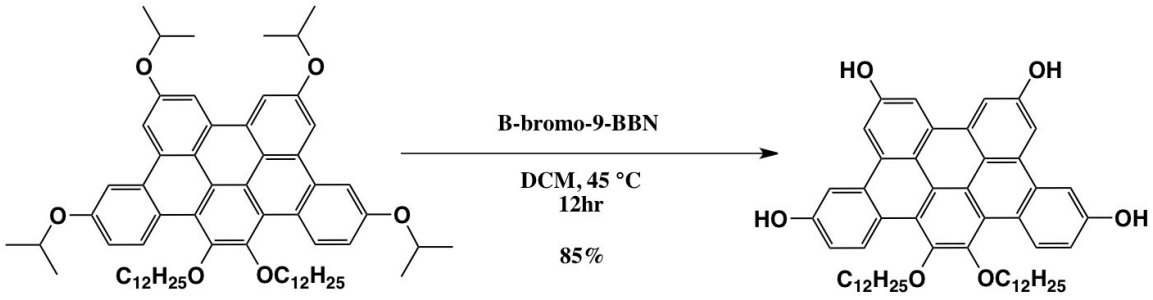

Scheme 1.3. Dealkylation of TBP.

1.4 Structural Characterization

Compounds **1a**, **1b** and **1c** are soluble in common organic solvents such as chloroform, methylene chloride, and THF, while compound **1d** is soluble in acetone and THF. Their structures and purity have been confirmed by ^{1}H & ^{13}C NMR, MALDI-TOF MS measurements, and elemental analysis. Figure 1.7 shows the ^{1}H NMR spectra of the aromatic region of the four TBP compounds, where sharp and well resolved signals are observed. The assignment of all signals was made based on the chemical shifts, multiplicity, integrations and confirmed by their 2D COSY spectra (Figure 1.8-1.11).

Compounds **1b** and **1c** show five aromatic signals: two doublets and three singlets (or two *dd* and three *d* under high resolution), while compound **1d** shows two additional singlets in the aromatic region which can be attributed to the two types of hydroxyl protons. It is noted that the two adjacent aromatic protons “a” and “e” in all four compounds have very different chemical shifts, differing by nearly 2.5 ppm in compounds **1b**, **1c** and **1d**. The unusually high chemical shift of protons “a” is likely due to H-bonding with the alkoxy O atom.

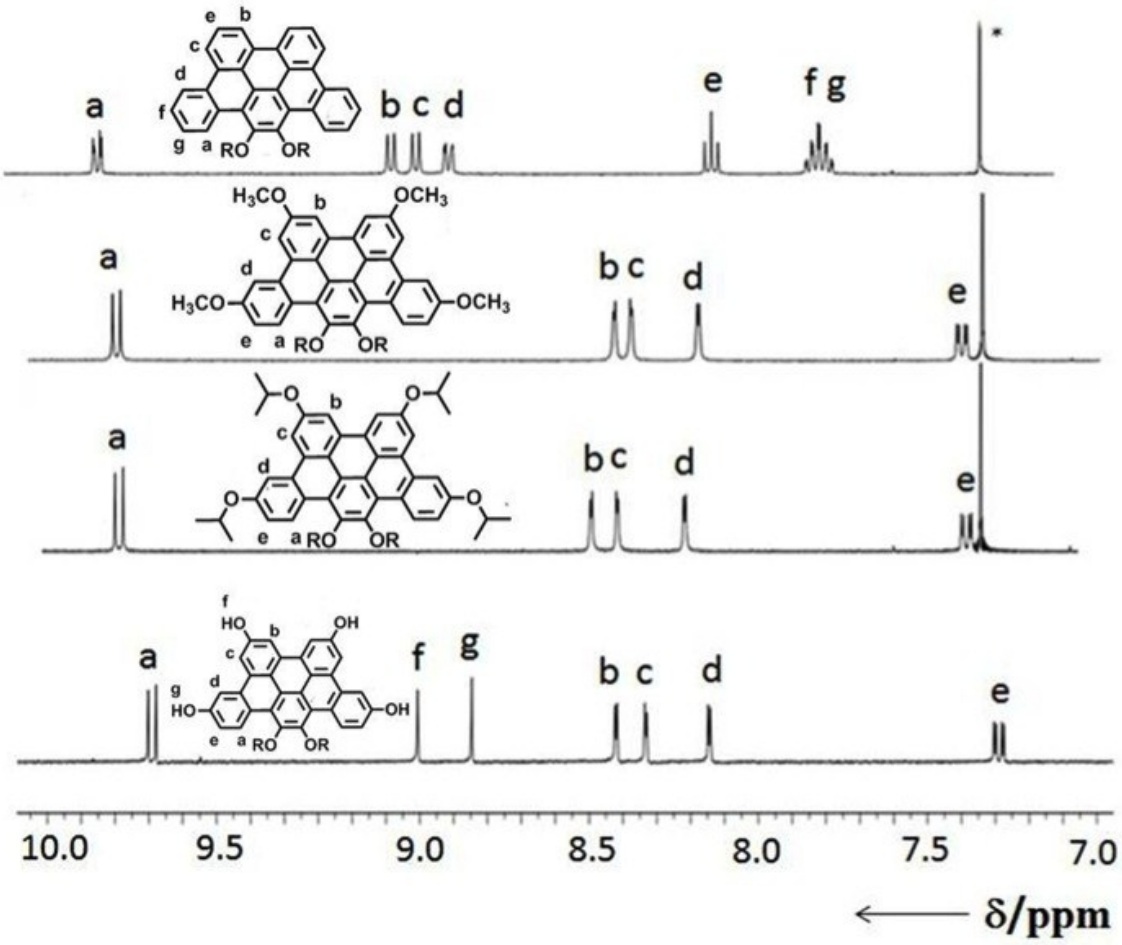

Figure 1.7. ^{1}H NMR spectra (aromatic region) of the four TBP compounds.

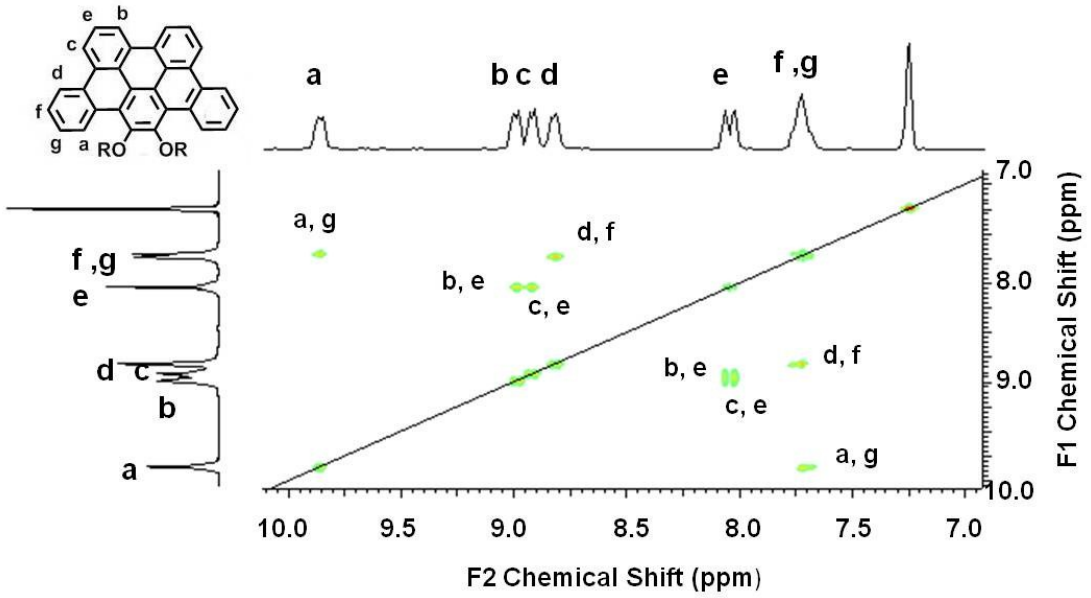

Figure 1.8. Selected region from 400 MHz 2D COSY ($CDCl_3$, 298K) ^1H NMR spectrum of **1a.**

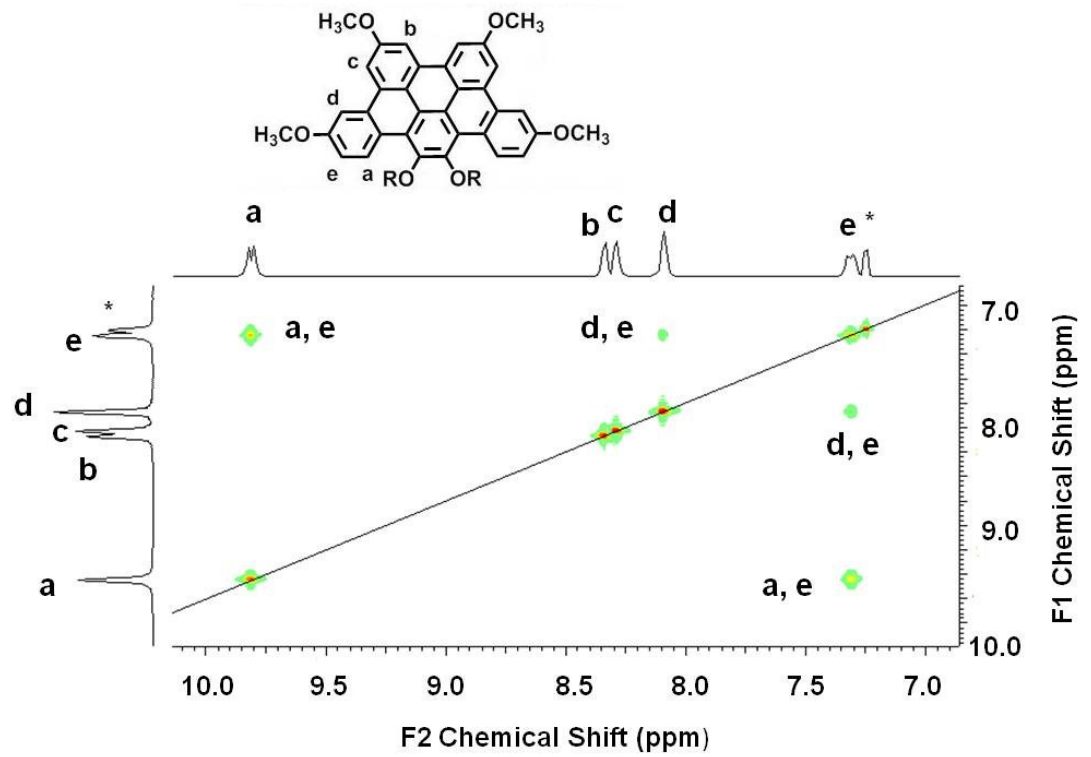

Figure 1.9. Selected region from 400 MHz 2D COSY ($CDCl_3$, 298K) ^1H NMR spectrum of **1b.**

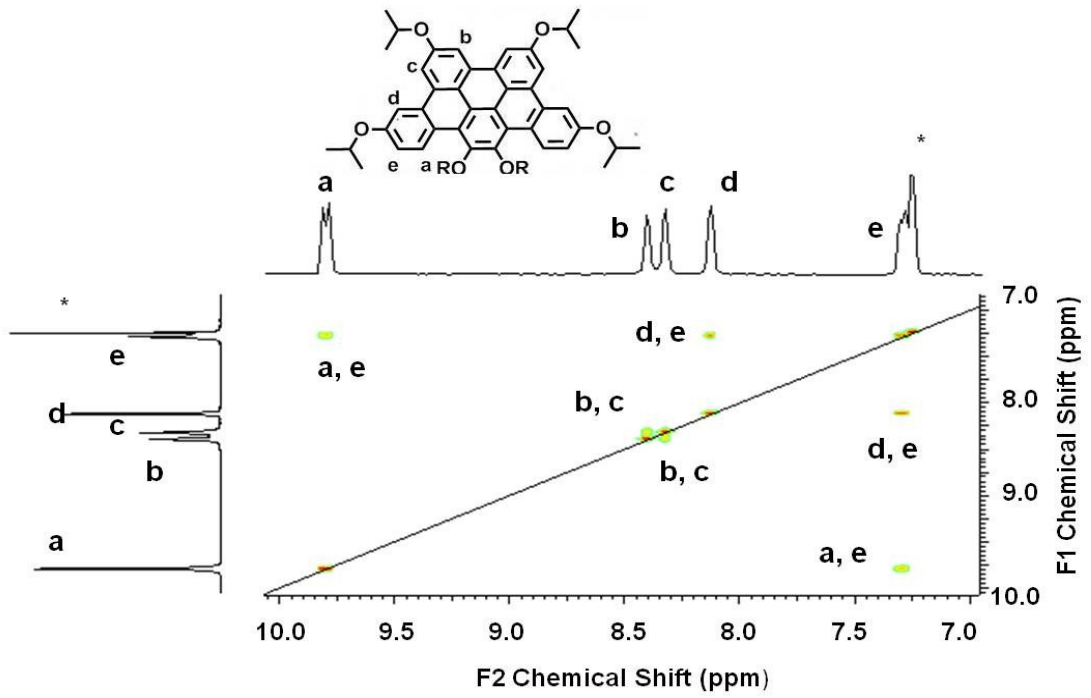

Figure 1.10. Selected region from 400 MHz 2D COSY ($CDCl_3$, 298K) ^1H NMR spectrum of **1c.**

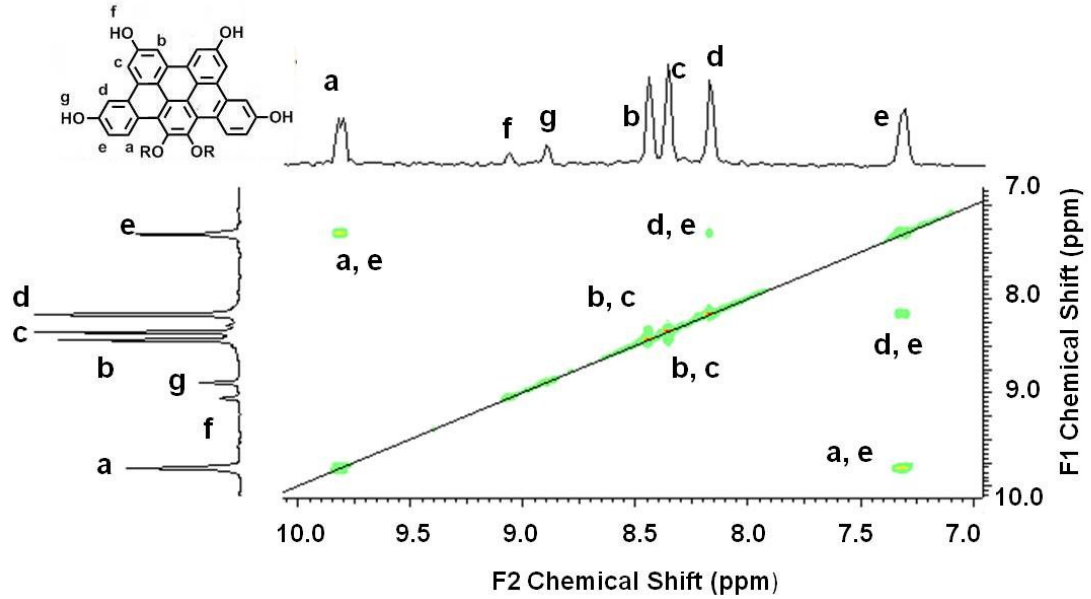

Figure 1.11. Selected region from 400 MHz 2D COSY ($CDCl_3$, 298K) ^1H NMR spectrum of **1d.**

All four TBPs have been subjected to MALDI-MS analysis. As shown in Figure 1.12-1.15, compounds **1b, 1c** and **1d** all give three major peaks: 526.91, 695.01, 865.15 for **1b**, 639.15, 807.31, 977.49 for **1c** and 470.84, 638.94, 808.07 for **1d**. The three peaks can be assigned to the molecular ion losing 2, 1, or 0 n-dodecyl chains, respectively. For Compound **1a**, because a mixture of silver trifluoroacetate/dithranol matrix was used, MALDI-MS gives two additional peaks which are attributed to ($M+Ag^+$). The purity of the four TBP derivatives were also confirmed by the elemental analysis (Table 1.1).

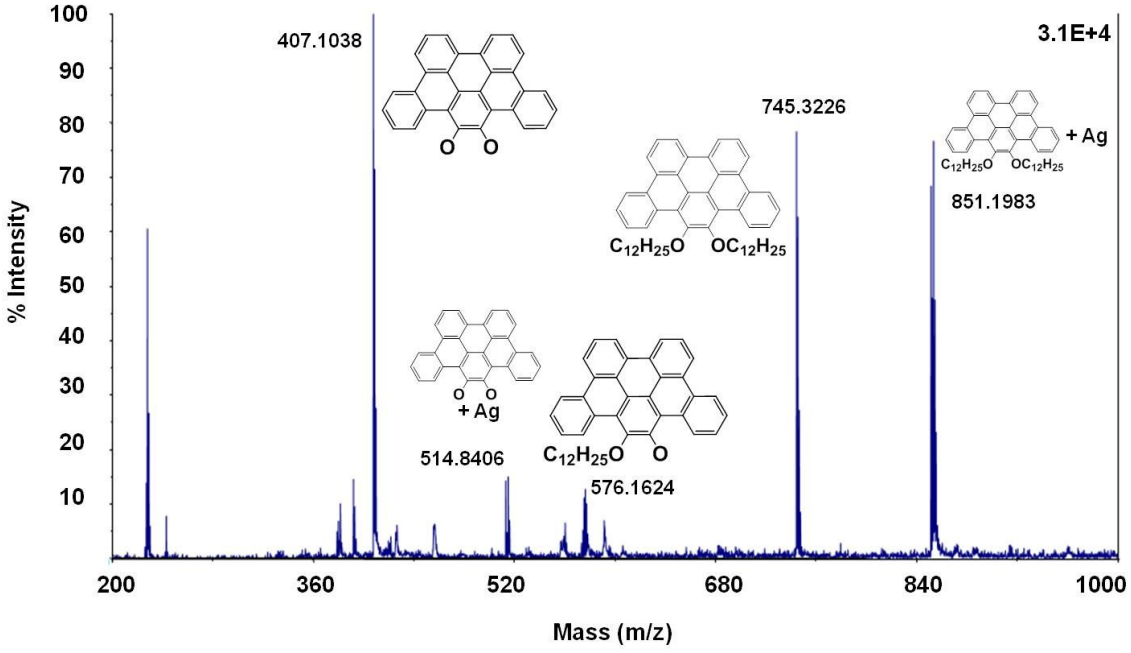

Figure 1.12. MALDI-TOF Spectra of **1a**

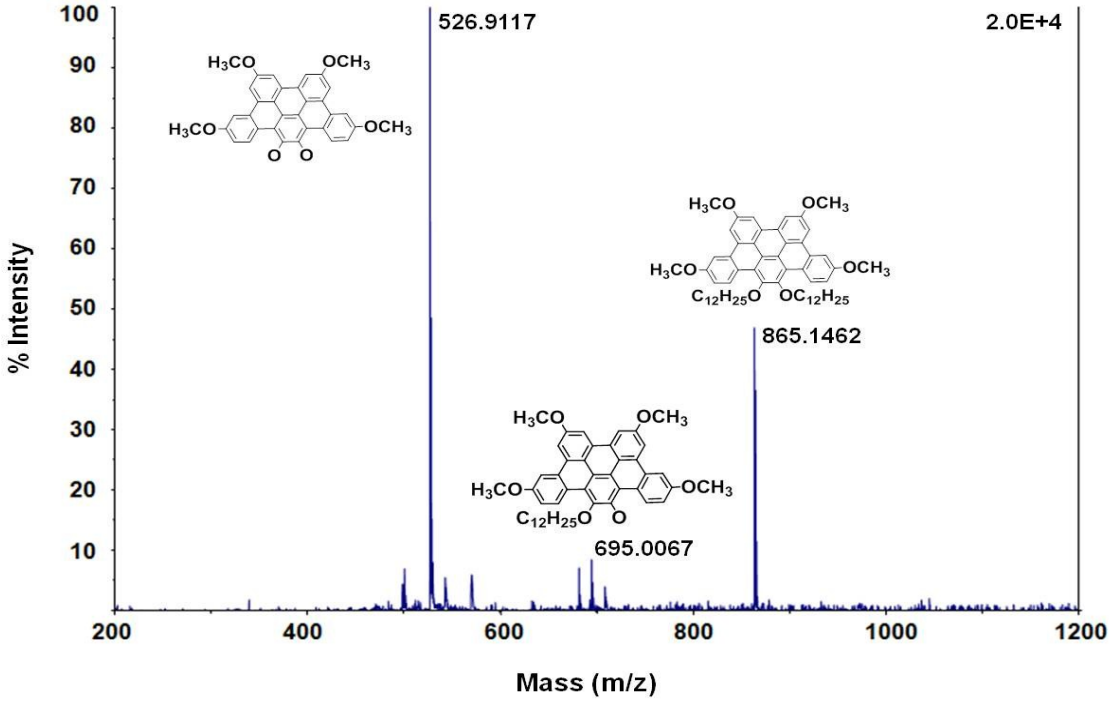

Figure 1.13. MALDI-TOF Spectra of **1b**

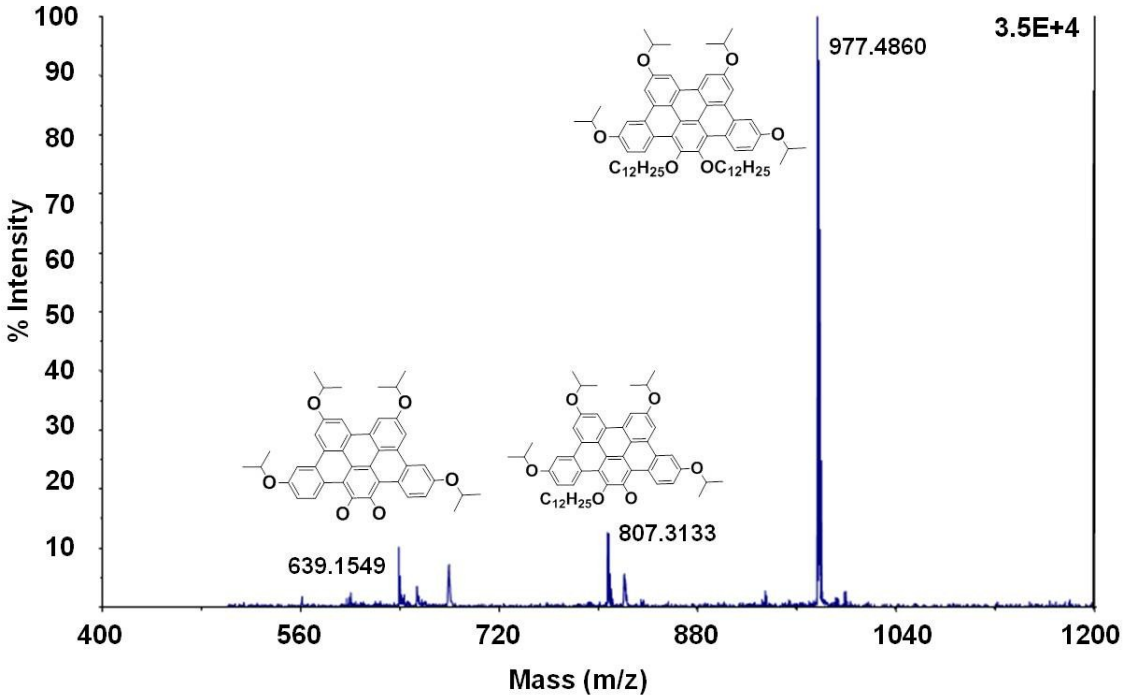

Figure 1.14. MALDI-TOF Spectra of **1c**

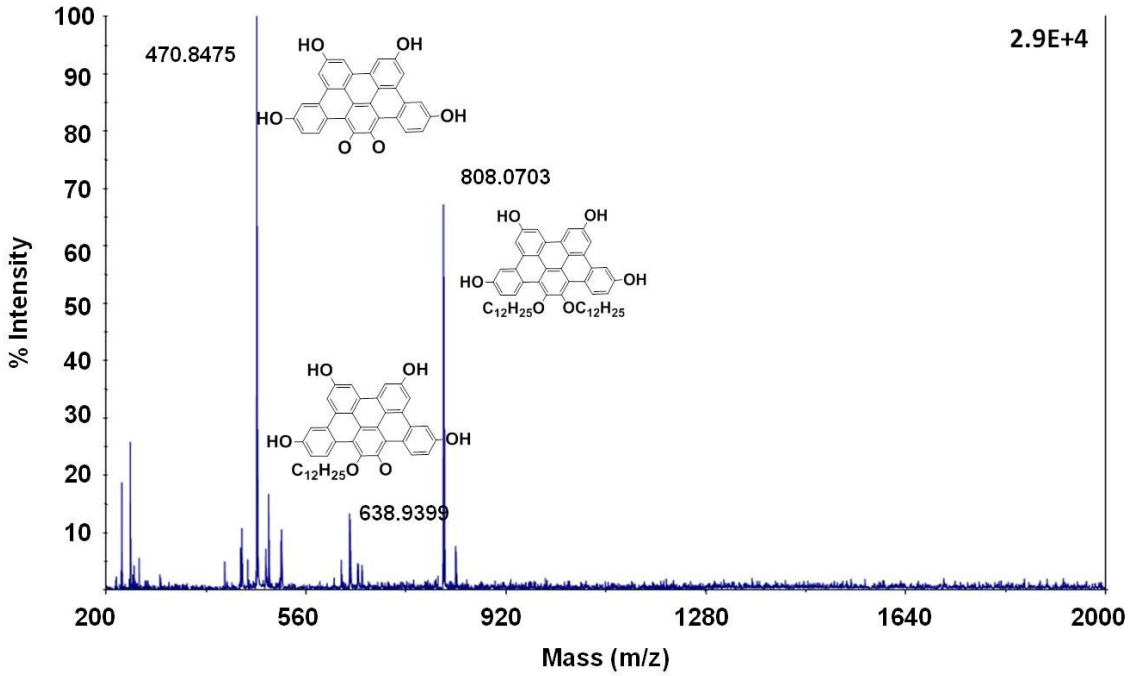

Figure 1.15. MALDI-TOF Spectra of **1d**

Table 1.1. Elemental Analysis of TBPs

Compound	**1a**	**1b**	**1c**	**1d**
Anal. Calcd.	C:87.05;H:8.66	C:80.52;H:8.39	C:81.1;H:9.07	C:80.16;H:7.97
Found	C:86.79;H:8.42	C:80.56;H:8.29	C:80.89;H:8.81	C:79.89;H:8.02

1.5 Optical Properties of Tribenzopentaphene Derivatives

The optical properties of all TBP derivatives were studied by UV/Vis absorption, fluorescence excitation, and fluorescence emission measurements in chloroform and as solid films.

Absorption spectra: Figure 1.16 shows the UV-Vis absorption spectra of the four TBPs in chloroform and as solid films. In solution, all four compounds showed a strong band at around 315 nm and a number of less intense bands at longer wavelengths. For **1a** with only two alkoxy substituents at the bay positions, two moderately strong bands at 354 nm and 370 nm and one much weaker band at 410 nm are observed. The 410 nm, 354/370 nm, and 312 nm bands are α, *p*, and β bands, respectively, following Clar's classification.[40] The energy ratio of the β band over the α band is 1.314, slightly deviated from the 1.35 ratio normally observed for uniplanar PAHs, indicating the twisting of some rings which results in the loss of some resonance energy.[41] It is noted that the three prominent bands (β and *p* bands) of **1a** (312, 354 and 370 nm bands) closely match those of its alkyl analog (two alkyl groups instead of two alkoxy groups at the bay positions).[28] The α band of **1a** is however bathochromically shifted by 15 nm, compared to that of its alkyl analog.

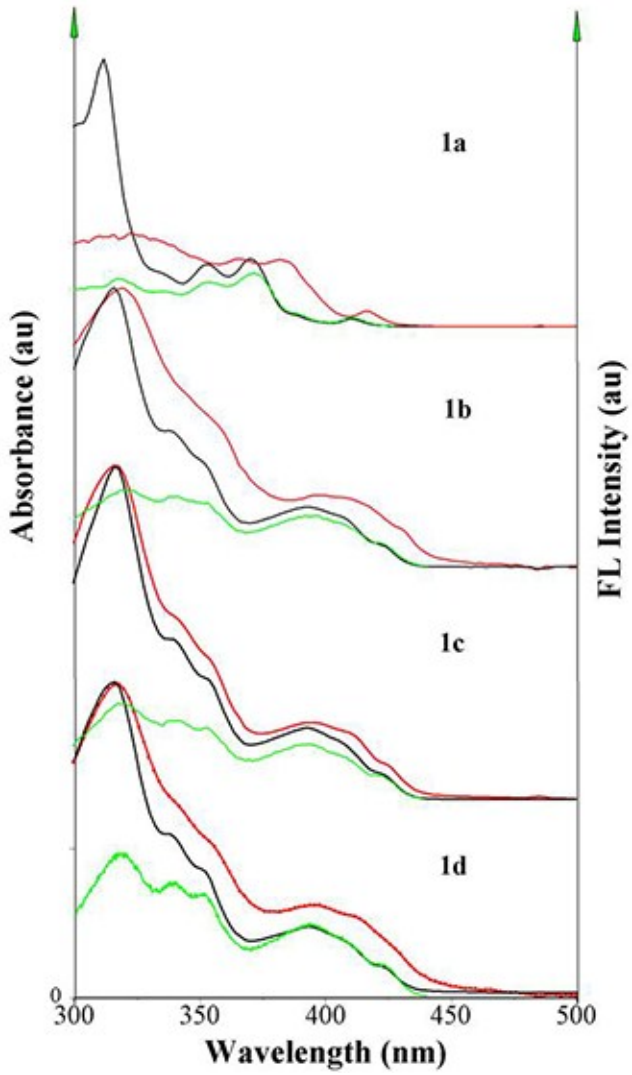

Figure 1.16. UV-Vis absorption (black) and excitation (green) spectra of the four TBP compounds in chloroform solutions. The red curves are the absorption spectra of the TBP films.

When four additional alkoxy (or hydroxyl in the case of **1d**) groups are attached to the outskirt of the TBP core, significant bathochromic shift (~ 40 nm) of the *p* band is observed which is now partially overlapped with the weaker α band as shown in the absorption spectra of **1b**, **1c** and **1d** in Figure 1.16. The α band is also red-shifted but to a much less extent (~12 nm) while the β band shows negligible shift. When the absorption spectra of films are compared to those of solutions, one notices a 8-nm red-shift in band-edge for **1a**, **1b** and **1d** but only 3-nm red-shift in **1c**, indicating much weaker inter-TBP π-π stacking interactions due to the steric blocking effect of those bulky isopropoxy groups.

Table 1.2. Fluorescence quantum yields of tribenzopentaphene derivatives measured in dilute chloroform solution.

Compound	**1a**	**1b**	**1c**	**1d**
λ_{ex} **(nm)**	370	394	394	394
Φ_{fl}	0.156	0.270	0.296	0.170

Fluorescence spectra: The fluorescence quantum yields for all four tribenzopentaphene derivatives are listed in Table 1.2. All four TBPs show moderately strong fluorescence (FL) in solutions. Figure 1.17 shows the emission spectra of both solutions and films of the four TBPs. The solution FL emission spectra of **1b**, **1c** and **1d** are nearly identical with a maximum emission wavelength λ_{max} of 432 nm, while the emission λ_{max} of **1a** is 418 nm. The fluorescence quantum yields of **1a**, **1b**, **1c** and **1d** in chloroform are 0.16, 0.27, 0.30, and 0.17, respectively (370 nm excitation for **1a** and 394 nm excitation for the other three compounds). The TBP films are also fluorescent. While the films of **1a**, **1b** and **1d** all gave a red-shifted, broad, and featureless emission band, the emission of film **1c** shows two bands closely matching its solution emission spectrum, again indicating the much weaker π-π stacking interaction in **1c** than in **1a**, **1b** and **1d**. When the excitation spectra are compared to the absorption spectra (Figure 1.16), one sees close matching of the two spectra in the α and *p* bands region for all four compounds. The β band in the excitation spectra is, however, much weaker than that in the absorption spectra, indicating inefficient energy transfer from the excited β band to the emissive S_1 state.

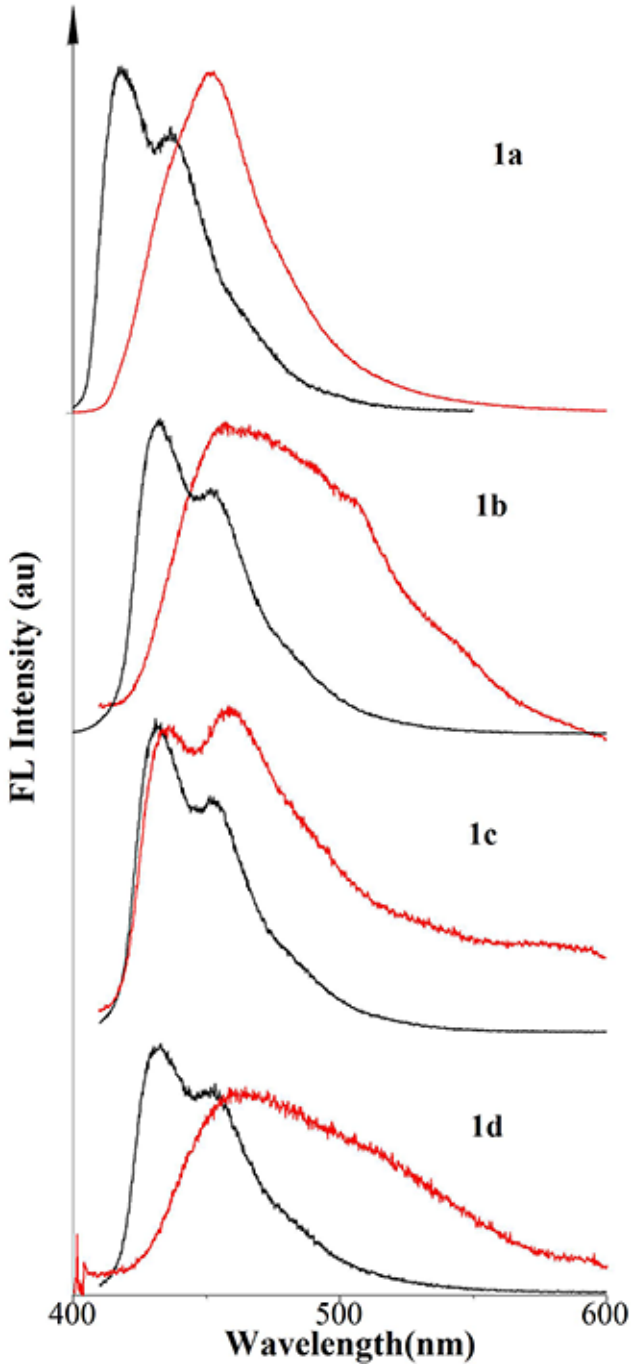

Figure 1.17. Fluorescence emission spectra of the four TBP compounds in chloroform solutions (black) and as solid films (red).

1.6 Electrochemical Properties of Tribenzopentaphene Derivatives

Cyclic voltammetry measurements were carried out in oxygen-free dichloromethane solutions for all compounds except for **1d** which was measured in an acetone solution 0.1 M tetrabutylammonium hexafluorophosphate was used as the electrolyte. A 1 mm^2 Pt disk was used as the working electrode, a silver wire was used as the reference electrode, and a Pt wire was applied as the counter electrode. Each measurement was calibrated with ferrocene (Fc) in dichloromethane or acetone. For reversible redox process, each anodic and cathodic potential was averaged as $E^{red/ox}_{1/2}=1/2\ (E_{pc} + E_{pa})$ to obtain the half potentials. For irreversible waves, anodic or cathodic onset potential was directly used. HOMO and LUMO energy levels were estimated on the basis of the reference energy level of ferrocene (4.8 eV below the vacuum level). The HOMO and LUMO energy was calculated based on the following equation: $E_{HOMO}/ E_{LUMO} =4.8 + (E_{1/2} – E^{FC}_{1/2})$ eV. Optical band gap of each compound was calculated from their UV/Vis absorption spectra by $E_{opt}= 1240/ \lambda$ (nm) eV. Optical band gap was used to calculate the HOMO or LUMO energy levels for compounds where only oxidation or reduction peak was found in CV measurement.

Table 1.3. Redox potentials of tribenzopentaphene derivatives.

Compounds	E_0^{ox} (V)	E_0^{red} (V)	E_{OPT} (eV)	E_{HOMO} (eV)	E_{LUMO} (eV)
1a	1.08	0.96	2.97	-5.67	-2.76
1b	0.79	0.62	2.86	-5.35	-2.49
1c	0.63	0.50	2.86	-5.21	-2.35
1d	0.78	-	2.86	-5.38	-2.52

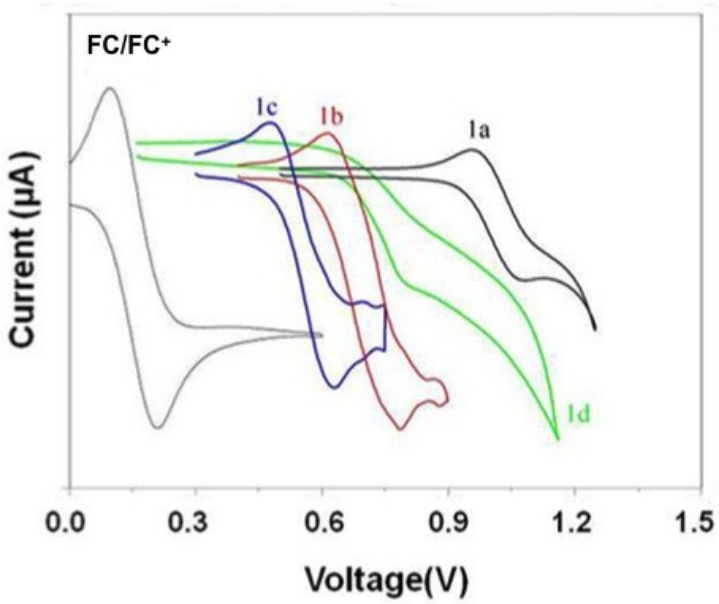

Figure 1.18. Cyclic voltammograms of **1a**, **1b**, and **1c** in CH_2Cl_2 and **1d** in acetone solutions (The voltammogram of **1d** was corrected based on Fc/Fc^+ internal standard in acetone).

As shown in Figure 1.18, TBPs **1a**, **1b** and **1c** all show a reversible oxidation wave with half-cell potentials of 0.87, 0.55, and 0.42 V, respectively, while **1d** shows a semi-reversible oxidation wave with an oxidation peak potential (E_{pa}) of 0.78 V and an estimated half-cell potential of 0.73 V. Under identical conditions, a reversible oxidation wave ($E_{1/2}$ = 0.15 V) is observed for the ferrocene/ferrocenium couple. Using the ferrocene energy level of 4.8 eV below vacuum, the HOMO energy levels of **1a**, **1b**, **1c**, and **1d** were calculated to be -5.67, -5.35, -5.21 eV, and -5.38 eV, respectively. The gradual increase in HOMO energy levels from **1a** to **1d** to **1b** to **1c** reflects the increasing electron-donating effect of the alkoxy substituents. No reduction wave was observed for all four compounds within the scan range of 0 to -2 V.

1.7 Molecular Self-assembly of Tribenzopentaphene Derivatives

When methanol or hexane vapor was diffused into the chloroform solutions of **1a**, **1b**, **1c**, and THF solution of **1d**, the clear solutions became opaque in a day or two. The opaque solutions were drop-cast onto silicon wafer, vacuum dried and then sputter-coated with a thin layer of gold. Field-emission scanning electron microscopy (SEM) XL30 (FEI Company, Hillsboro, OR) was used with an accelerating voltage of 5.0 kV. The SEM images (Figure 1.19) of the **1a** and **1b** films show fiber structures which are tens and even hundreds of microns long and have a fairly uniform diameter of around 200 nm. The fiber structures in **1a** appear to be flexible as they are coiled, bent, and entangled together, while the fiber structures of **1b** seem more rigid as they are mostly straight and oriented along the same direction. Compound **1d**, on the other hand, aggregates to give microspheres with an average diameter of around 500 nm. Compound **1c** yields no well-defined aggregated structures. The different self-assembled structures of the four TBP compounds reflect clearly the effect of the different ring substituents. With small peripheral groups (Hs for **1a** and MeO- for **1b**), strong π-π stacking interactions are expected which drive the formation of long fiber structures. Compound **1d** has four hydroxyl substituents. In addition to π-π stacking interactions perpendicular to the TBP ring, there may exist strong H-bonding in lateral directions. Furthermore, the amphiphilicity of compound **1d** may dictate the self-assembled structures as well. The overall result is the formation of microspheres. With four bulky isopropoxy groups, compound **1c** lacks strong π-π stacking interactions which significantly slows its self-assembly process. Such results are consistent with the NMR and optical property studies.

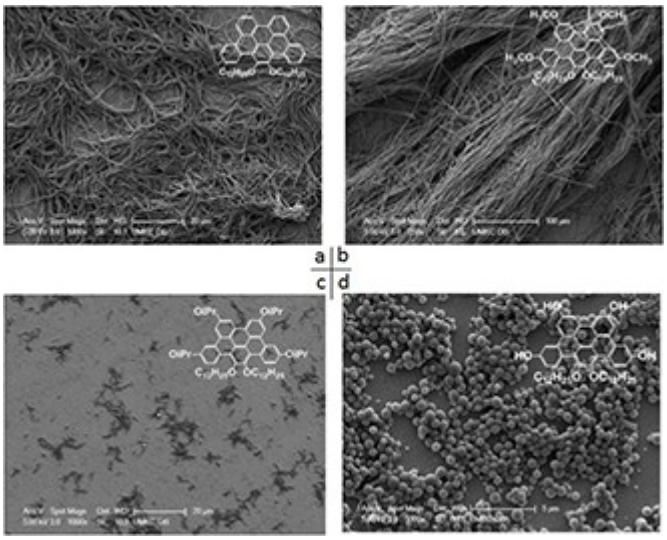

Figure 1.19. SEM images of self-assembled structures of **1a** (a), **1b** (b), **1c** (c) and **1d** (d).

1.8 Thermotropic Liquid Crystalline Behaviors and Optical Textures of Tribenzopentaphene Derivatives

Thermal phase behavior of the TBP derivatives **1a-1c** was studied using differential scanning calorimetry (DSC) and polarized optical microscopy (POM). The DSC data for compound **1a-1c** were organized in Table 1.4. Compound **1d** was not studied due to its poor air stability. Figure 1.20**a-c** shows the DSC thermograms of compounds **1a-1c**. All samples were first heated to 200 °C, a temperature higher than their melting temperatures but significantly lower than their decomposition temperatures, followed by controlled cooling from 200 °C to 0 °C and were subsequently subjected to the second heating run. Both the heating and the cooling rate was set at 10 °C/min. During the first heating run, both **1a** and **1b** show two endothermic transitions. Coupled with polarized optical microscopy studies, the second transition for both compounds can be assigned to the melting transition (to the isotropic liquid phase) while the first transition can be assigned

Table 1.4. Phase transition temperatures and enthalpies of TBPs from DSC[a].

Thermal transition T(°C) [Enthalpy changes ΔH(J/g)]	
First heating	Second heating
1a Cr 78 (36) Col_1 101.6 (30) I	Cr 64.7 (10) Col_1 101.4 (29.7) I
1b Cr 90 (20) Col_1 120.7 (27.5) I	Cr 59 (21) Col_1 85.8 (10.3) Col_2 120.7 (27.5) I
1c Cr 59.8 (35.8) I	

[a]Abbreviations: Col_1 Col_2 columnar phase, Cr for crystalline phase, I for isotropic phase.

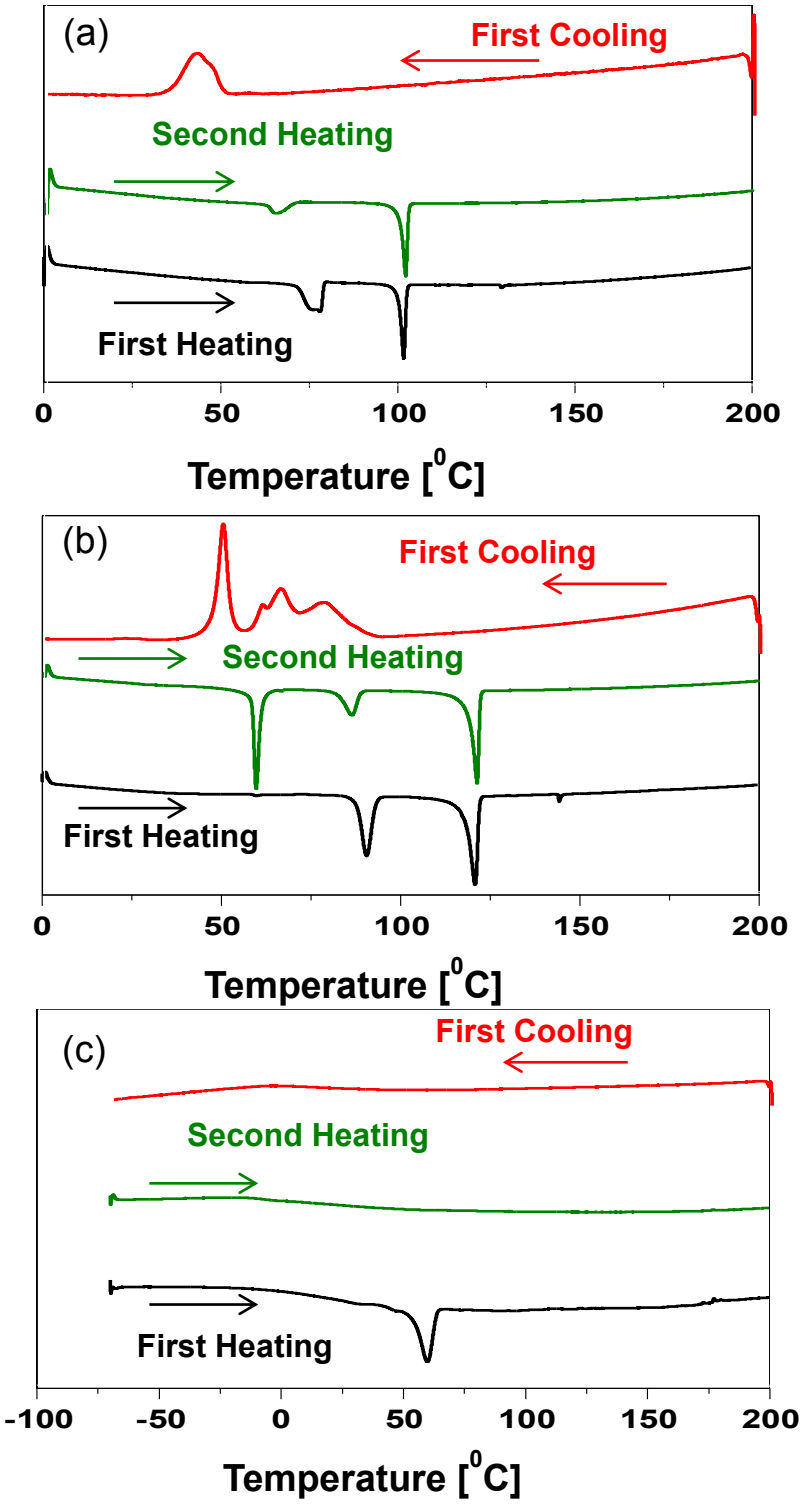

Figure 1.20. DSC thermograms of **1a** (a), **1b** (b), and **1c** (c).

to the phase transition from the crystalline solid to the columnar liquid crystal mesophase. Both phase transition temperatures of **1b** are higher than those of **1a**. **1c**, however, showed only one endothermic phase transition at around 60 ^{o}C which was found to be the melting transition. In the second heating run, **1a** again showed two phase transitions. Interestingly, **1b** showed, in addition to the two transitions seen in the first heating run, a new sharp endothermic peak at a lower temperature (~59 °C). This new transition indicates the formation of a new mesophase when the sample was cooled from the melt. Indeed, the cooling run of **1b** showed a sharp and strong exothermic peak at around 50 °C. The corresponding peak is missing in the cooling thermogram of **1a**. The second heating run of **1c** shows no thermal transition peak other than a broad glass transition, indicating there is no crystalline order in the freshly cooled sample. The cooling thermogram of **1c** similarly exhibits no phase transitions.

Figure 1.21 shows the polarized optical miscroscopy images of **1a**, **1b** and **1c**, taken at the specified temperatures during cooling from their respective isotropic phase. A series of images taken at varied temperatures during cooling can be found in Figure 1.22-1.24. Each sample was sandwiched between two glass slides and then heated to its isotropic phase, and heating/cooling rate was set to 1 ^{o}C / mins. As shown in Figure 1.21a, spherulitic textures with maltese crosses are clearly observed in **1a**. The texture is a typical signature for discotic liquid crystal[42] and indicates a columnar mesophase (Col).[42-43] The spherulite formation of discotic molecules has been reported mostly on low molecular weight mesogens[44] or substantially smaller cores of discotic molecules except for 2-decyltetradecyl hexabenzocorene (HBC).[42] **1b** showed spherulitic textures as

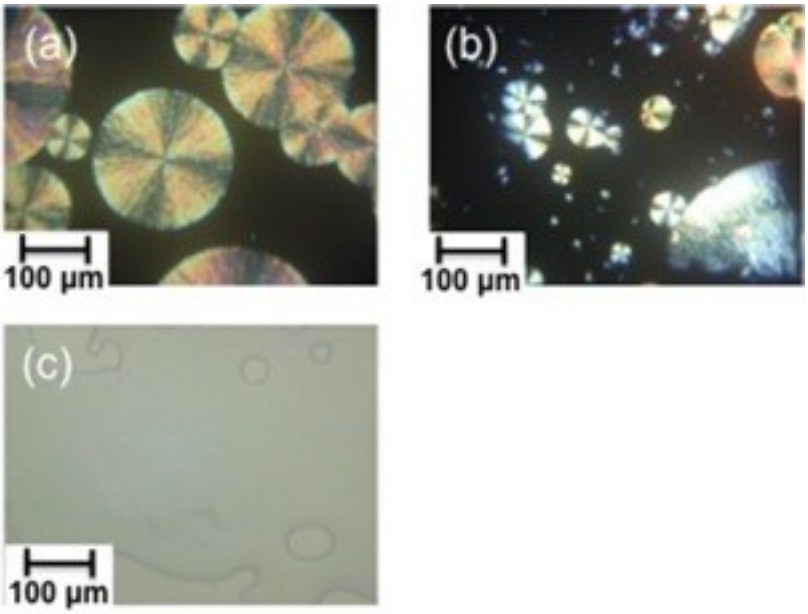

Figure 1.21. Polarized optical microscopy images of **1a** at 78 °C (a), **1b** at 83 °C (b) **1c** at 25 °C (c).

well but they are smaller, less regular with broken "fan" structures. **1c** on the other hand showed no texture (Figure 1.21c) under cross-polarizers during cooling indicating no directional ordering. These results indicate that both compounds **1a** and **1b** form thermotropic discotic liquid crystals. **1a** forms well-ordered columnar liquid crystal phase with a diameter of 200 nm, which indicated an exceptionally long range ordered self assembly. **1b** however forms both ordered and disordered columnar mesophases with a diameter of less than 50 nm, presumably due to the four methoxy groups which may disrupt close π–π stacking of the TBP rings. Compound **1c**, on the other hand, lacks π–π interaction due to the steric effect of the four bulky isopropyl groups, leading to disordered solids. However, it is worth noting that compound **1c** will slowly solidify after a few weeks, and its texture using the same slide of sample was discovered after two months (Figure 1.25).

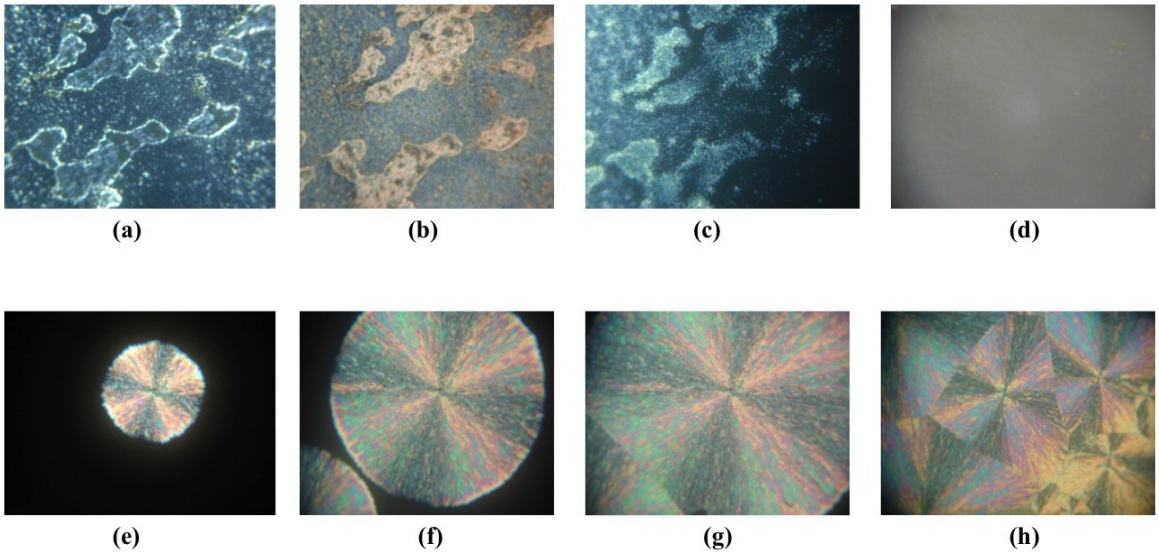

Figure 1.22. Polarized optical microscopy images of compound **1a** in heating process at 25 ºC (a), at 65 ºC (b), at 103 ºC (c), at 108 ºC(d), and cooling process at 64 ºC (e), at 63 ºC (f), at 62 ºC (g), at 33 ºC (h).

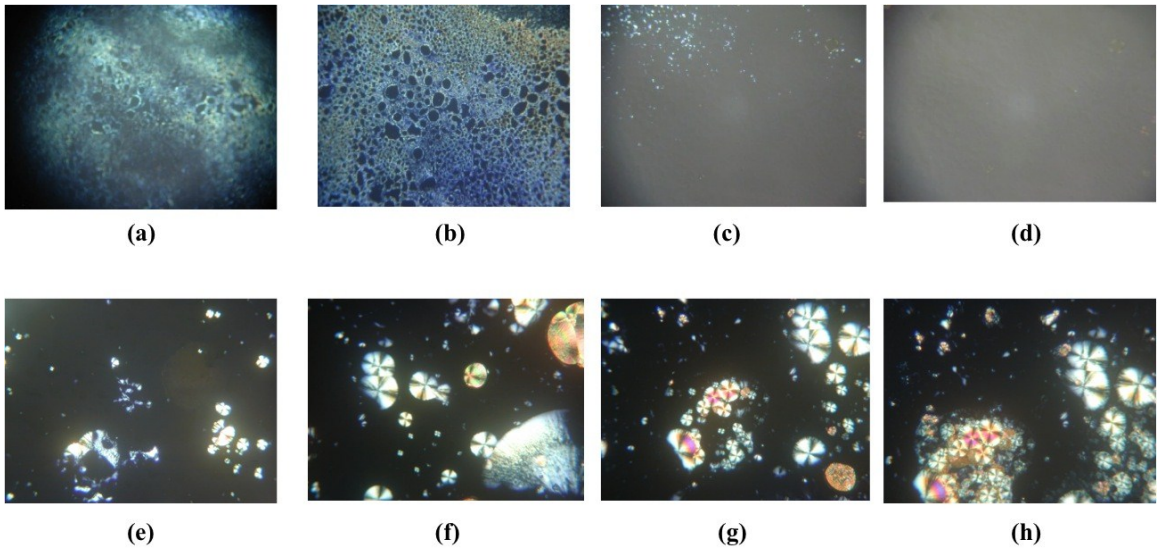

Figure 1.23. Polarized optical microscopy images of compound **1b** in heating process at 27 ºC (a), at 85 ºC (b), at 122 ºC (c), at 124 ºC(d), and cooling process at 89 ºC (e), at 83 ºC (f), at 55 ºC (g), at 45 ºC (h).

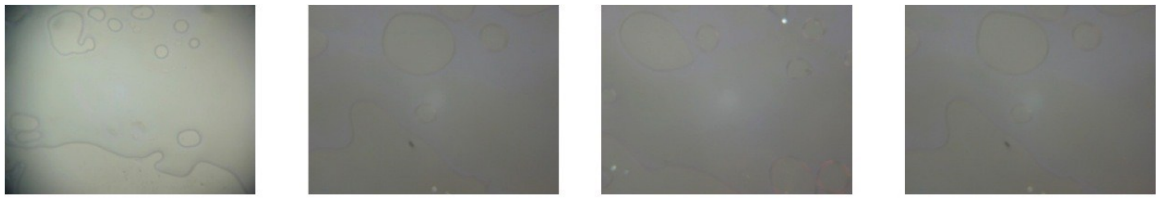

Figure 1.24. Polarized optical microscopy images of compound **1c** in heating process at 25 ºC (a), at 75 ºC (b), and cooling process at 45 ºC (c), at 27 ºC(d).

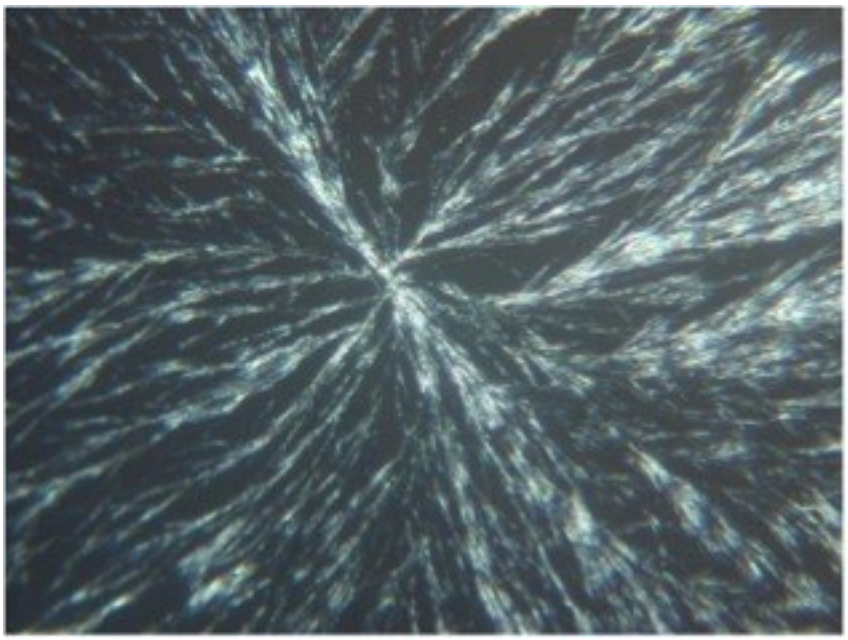

Figure 1.25. Polarized optical microscopy images of compound **1c** after 2 months at room temperature.

1.9 Conclusions

In summary, four alkoxy-substituted TBP derivatives have been synthesized and characterized. All four compounds are moderately fluorescent in dilute solutions when excited at their α or p bands. Excitation at the β band (~315 nm, the strongest absorption band), however, gave much lower fluorescence quantum yields. The TBP rings exhibit strong π-π stacking interactions in **1a, 1b** and **1d** but not so much in **1c** due to the steric effect of the four bulky isopropoxy groups. Driven by the strong π-π stacking interaction, **1a** and **1b** self-assemble into microfibers. With additional hydrogen bonding and amphiphilic interactions coming into play, compound **1d** aggregates into microspheres. Compound **1c** on the other hand fails to assemble into well-defined structures under similar conditions. Their thermal behaviors were investigated by DSC and POM. Compounds **1a** and **1b** form thermotropic dicotic liquid crystal phases while **1c** does not. While **1a** forms an exceptionally long range ordered columnar mesophase, **1b** forms both ordered and disordered columnar mesophases.

1.10 Experimental Section

General.

All the reactions were carried out under Nitrogen protection in flame-dried glassware. The solvents were used after fresh distillation over drying agents indicated and were transferred under nitrogen: THF (Na/benzophenone), CH_2Cl_2 (CaH_2). All the other reagents were purchased from Sigma-Aldrich and were used without further purification. 1-Bromo-2-iodo-4-methoxybenzene (**2b**), and 1-bromo-2-iodo-4-isopropoxybenzene (**2c**) were synthesized according to literature procedures.[45] Compounds **3a-3c** were synthesized by palladium-catalyzed Suzuki coupling reactions of aryl boronic acid and aryl halide of literature method.[29-32]

Instrumentation.

The ^1H and ^{13}C NMR spectra were recorded on a Varian INOVA 400 MHz FT NMR Spectrometer in the solvent indicated; chemical shifts (δ) are given in ppm relative to TMS, coupling constant (*J*) in Hz. The solvent signals were used as references[46] ($CDCl_3$: δ_C = 77.16 ppm; residual $CHCl_3$ in $CDCl_3$: δ_H = 7.26 ppm; Acetone-d6: δ_C = 206.26, 29.84 ppm; residual acetone in acetone-d6: δ_H = 2.05 ppm). UV-Vis absorption spectra were measured using a Hewlett-Packard 8452A Diode Array Spectrophotometer. Emission and excitation spectra were measured using a Shimadzu RF-5301PC Spectrofluorophotometer. Fluorescence quantum yield for solution was determined using quinine sulfate in 1N H_2SO_4 (φ = 0.58) as the standard. Cyclic voltammetry (CV) studies were carried out in freshly distilled dichloromethane for **1a**, **1b**, **1c** and acetone for **1d** under argon protection at room temperature using a BAS Epsilon EC Electrical Station employing a 1 mm^2 Pt disk as the working electrode, a silver wire as the reference

electrode, and a Pt wire as the counter electrode. $[Bu_4N]PF_6$ was used as the supporting electrolyte. The scan rate for all the measurements was set at 50 mV/s. Ferrocene was used as an internal standard. MALDI-TOF measurements were carried out on a Voyager DE Pro (Perspective Biosystem/ABI) Mass Spectrometer, operating in linear and reflector mode. Dithranol (1,8-dihydroxyanthrone) and a mixture of silver trifluoroacetate/dithranol (1:25, w/w) were used as the matrix. DSC measurements were performed on a PerkinElmer DSC8000 with a heating and cooling rate of 10 ^oC/ min. A Nikon polarizing optical microscopy equipped with a gas flow heating/cooling stage and a Nikon CoolPix 950 camera was used to record the POM images. Each sample was sandwiched between two glass slides and was then heated to its isotropic phase. After annealing for 30 min, the sample was cooled from the isotropic phase to room temperature at a cooling rate of 1 °C /min. POM images were recorded at selected temperatures.

1,2-bis(dodecyloxy)benzene (2). A mixture of pyrocatechol (6.40 g, 58.1 mmol), K_2CO_3 (40.1g 290 mmol), and 1-bromododecane (30.4 g, 122.01 mmol) in DMF(150 mL) was heated to 80°C overnight with stirring under a nitrogen atmosphere. After cooling to room temperature, the solvent was removed under distillation. The residue was purified by flash column chromatography on silica gel to give the title product as white crystals in 90% yield. ^{1}H NMR (400 MHz, $CDCl_3$): 6.89 (br, 4H, Ar-H), 4.00 (t, J = 8 Hz, 4H, OCH2-), 1.87-1.77 (m, 4H), 1.53-1.44 (m, 4H), 1.38-1.32 (br, 8H), 0.91 (t, $_J$ = 8 Hz, 6H, -CH_3).

1,2-Bis(decyloxy)-4,5-diiodobenzene (3). A 1,2-bis(dodecyloxy)benzene (10g, 22.2 mmol), iodine (5.19 g, 20.5 mmol) and iodic peroxide (2.34 g 13.3 mmol) were dissolved in a mixture of AcOH/H_2O/H_2SO_4 (60 mL, volumetric ratio of 100/20/3). After stirring for 6 h at 70 °C, color of the reaction mixture changed from purple to red. 10% Na_2SO_3 aq. was added to the mixture. The resulting brown sprecipitates were collected by filtration and re dissolved in CH_2Cl_2, and washed with water and brine. The organic phase was dried over $MgSO_4$, the solvent was evaporated under vacuum, the product was purified by recrystalization twice from methanol to afford 1,2-bis(decyloxy)-4,5-diiodobenzene (12.3 g, 80%). ^{1}H NMR (400 MHz, $CDCl_3$): δ7.25 (s, 2H), 3.92 (t, *J* = 8 Hz, 4H,), 1.79 (quint, *J* = 8 Hz, 4H), 1.50–1.20 (m, 28H), 0.89 (t, *J* = 6.8 Hz, 6H).

1-bromo-2-iodo-4-methoxybenzene (6b). Bromine (4.13 mL, 80.7 mmol) was added dropwise to a solution of 3-iodoanisole (15.0 g, 64.1 mmol) in 98 mL glacial HOAc and the resulting orange mixture was stirred at room temperature for 26 h. For work up, the solution was diluted with 250 mL 5% $Na_2S_2O_3$ and extracted with 50 mL hexane 5 times and followed by 50 mL brine. The organic solution was combined and dried with magnesium sulfate then concentrated to an orange oil. The product was purified by column chromatography (100% hexane on silica gel) to afford colorless oil (16.44g, 82%). ^{1}H NMR (400 MHz, CDCl3): δ 7.46 (d, *J* = 8 Hz, 1H), 7.38 (d, *J* = 2 Hz, 1H), 6.76 (dd, *J* = 8 Hz, 2 Hz, 1H), 3.76 (s, 3H).

1-bromo-2-iodo-4-isopropoxybenzene (6c). The above procedure was followed. The liquid was purified by column chromatography on silica gel (hexane : CH_2Cl_2=5:1, v/v) to afford colorless oil (70%). ^{1}H NMR (400 MHz, CDCl3): δ 7.44 (d, *J* = 8 Hz, 1H),

7.36 (d, *J* = 2 Hz, 1H), 6.73 (dd, *J* = 8 Hz, 2 Hz, 1H), 4.45 (m, 1H), 1.30 (d, *J* = 4 Hz, 6H).

2-bromo-5,3-bis(methoxy)-biphenyl (7b). To a solution of 3-bromoanisole (8.0 g, 42.8 mmol) in dry THF (50 mL) at -78°C was added dropwise 2.5M n-BuLi in hexane (25 mL, 64.2 mmol) and continuously run for another hour under N_2 protection. Trimethyl borate (7.1g, 68.4 mmol) was then added to the solution, and the resulting mixture was warmed to room temperature and stirred overnight. toluene (45 mL), ethanol (45 mL) and water (20 mL) were then added, followed by N_2 bubbling for 45 mins. 3-iodo-4-bromoanisole (11.2 g, 35.8 mmol), sodium carbonate (22.8 g, 214.8 mmol) and $Pd(PPh_3)_4$ were then added. After the reaction mixture was stirred at 90 °C for 48 h under nitrogen atmosphere, some water was added to the resulting solution, and then the mixture was extracted with dichloromethane several times. The organic phase was dried over magnesium sulfate. After filtration and solvent evaporation, the residue liquid was purified by column chromatography on silica gel (hexane : CH_2Cl_2=10:1) to afford colorless oil (7.5 g, 72%). ^{1}H NMR (400 MHz, $CDCl_3$): δ7.56-7.55 (d, 1H, Ar-H), 7.38-7.35 (t, 1H, Ar-H), 7.01-7.00 (d, 1H, Ar-H), 6.97-6.95 (m, 2H, Ar-H), 6.91 (s, 1H, Ar-H), 6.81-6.79 (d, 1H, Ar-H), 3.87 (s, 3H, CH_3), 3.83 (s, 3H, OCH_3). ^{13}C NMR (400 MHz, CDCl3): δ159.5, 159.2, 143.7, 142.9, 134.1, 129.4, 122.1, 117.0, 115.4, 115.2, 113.7, 113.4, 55.9, 55.7.

2-bromo-5,3-bis(isopropoxy)-biphenyl (7c). The above procedure was followed. The liquid was purified by column chromatography on silica gel (hexane : CH_2Cl_2=10:1 to 2:1, v/v) to afford colorless oil (82%) which solidified after a few weeks. ^{1}H NMR (400 MHz, $CDCl_3$): δ7.52-7.50 (d, *J* = 8Hz, 1H, Ar-H), 7.33-7.29 (t, *J* = 8Hz, 1H, Ar-H),

6.96-6.94 (d, *J* = 8Hz, 1H, Ar-H), 6.92-6.88 (m, 2H, Ar-H), 6.80 (s, 1H, Ar-H), 6.76-6.74 (d, *J* = 8Hz, 1H, Ar-H), 4.61-4.57 (m, 1H), 4.56-4.50 (m, 1H), 1.37-1.36 (d, 6H), 1.34-1.33 (d, 6H). ^{13}C NMR (400 MHz, CDCl3): δ157.47, 157.14, 143.40, 142.53, 133.80, 123.28, 129.11, 121.54, 118.61, 118.16, 117.51, 116.74, 116.60, 115.48, 112.70, 70.34, 69.98, 22.22.

Compound 5. Under nitrogen atmosphere, n-BuLi (4.8 mL of 2.5 M solution, 12 mmol) was added dropwise to a solution of 2-bromobiphenyl (**3a**) (2.00 g, 8.58 mmol) in dry THF (35 mL) at -78 °C. The resulting solution was stirred for 1 h, followed by the addition of trimethyl borate (1.78 g, 17.2 mmol). The resulting mixture was stirred at room temperature overnight. To the above solution was added toluene (40 mL), ethanol (40 mL) and water (18 mL), followed by N_2 bubbling for 45 min. 1,2-bis(dodecyloxy)-4,5-diiodobenzene (2.40 g, 3.43 mmol), sodium carbonate (2.19 g, 20.6 mmol) and $Pd(PPh_3)_4$ (0.119 g, 0.103 mmol) were then added. The resulting reaction mixture was stirred at 90 °C for 48 h under nitrogen atmosphere and was then poured into water. The mixture was extracted with dichloromethane several times. The organic phase was collected and dried over anhydrous magnesium sulfate. After removing the solvent, the liquid residue was purified by column chromatography on silica gel (hexanes/CH_2Cl_2, 2/1, v/v) to afford the product as white crystals (1.26 g, 49%, mp 41-42 °C). ^{1}H NMR (400 MHz, $CDCl_3$): δ 7.05 (br, 12H), 6.86 (br, 2H), 6.70 (br, 2H), 6.63 (br, 2H), 6.15 (br, 2H), 3.90 (br, 4H), 1.79 (br, 4H), 1.27-1.43 (br, 36H), 0.88 (m, 6H); ^{13}C NMR (400 MHz, $CDCl_3$): δ 147.81, 141.60, 140.35, 139.45, 133.03, 131.66, 129.34, 127.74, 127.00, 126.59, 126.03, 116.80, 69.15, 32.09, 29.88, 29.83, 29.80, 29.62, 29.54, 29.37, 26.17, 23.03, 22.86, 14.30, 14.27.

Compound 8b. yellow oil (44%). ^{1}H NMR (400 MHz, $CDCl_3$): δ 6.94 (*br*, 2H), 6.67 (br, 6H), 6.44 (br, 2H), 6.30 (*br*, 2H), 6.22 (br, 2H), 6.11 (br, 2H), 3.93 (br, 4H), 3.79 (s, 6H), 3.60 (s, 6H), 1.80 (br, 4H), 1.43-1.27 (br, 36H), 0.89 (m, 6H); ^{13}C NMR (400 MHz, $CDCl_3$): δ 159.12, 158.09, 147.89, 142.75, 141.08, 133.15, 132.95, 132.81, 132.40, 128.48, 121.67, 116.95, 114.76, 113.44, 112.90, 112.42, 69.38, 55.37, 55.01, 32.09, 29.88, 29.83, 29.81, 29.62, 29.83, 29.41, 26.18, 22.85, 14.29.

Compound 8c. yellow oil (68%). ^{1}H NMR (400 MHz, CDCl3): δ 6.91 (br, 2H), 6.60 (br, 6H), 6.41 (br, 2H), 6.26 (br, 4H), 6.12 (br, 2H), 4.47 (br, 2H), 4.18 (br, 2H), 3.85 (br, 4H), 1.76 (br, 4H), 1.18-1.42 (br, 60H), 0.88(m, 6H); ^{13}C NMR (400 MHz, $CDCl_3$): δ 157.36, 156.39, 147.87, 142.88, 141.31, 133.20, 132.79, 132.14, 128.62, 121.63, 117.01, 116.86, 115.90, 114.59, 69.93, 69.66, 69.30, 32.09, 29.88, 29.83, 29.81, 29.60, 29.53, 29.42, 22.85, 22.47, 22.33, 22.25, 21.96, 14.29.

Compound 1a. A solution of anhydrous $FeCl_3$ (0.56 g, 3.45 mmol) in CH_3NO_2 (5.0 mL) was added dropwise to a solution of **5a** (0.26 g, 0.346 mmol) in dry CH_2Cl_2 (20 mL) with nitrogen bubbling through a two–neck round bottom flask at 0 °C. When the addition was completed, the ice bath was removed and resulting solution was stirred at room temperature for another hour. The reaction was quenched with CH_3OH (30 mL) and water (10 mL). The resulting mixture was stirred for 1 h. The organic layer was collected and the aqueous layer was extracted by dichloromethane three times (30 mL each). The combined dichloromethane extracts were dried over anhydrous $MgSO_4$. After filtration, the filtrate was stripped of solvent. The residual yellowish solid was purified by column chromatography (hexanes/CH_2Cl_2, 40/1 to 10/1, v/v), to give **1a** as light yellow solids (52 mg, 20%, mp 101~102 °C). ^{1}H NMR (400 MHz, $CDCl_3$): δ 9.87 (d, J = 8 Hz, 2H), 9.00

(d, *J* = 8 Hz, 2H), 8.92 (d, *J* = 8 Hz, 2H), 8.82 (d, *J* = 8 Hz, 2H), 8.05 (t, *J* = 8 Hz, 2H), 7.77 (m, 4H), 4.19 (t, *J* = 8 Hz, 4H), 2.03 (m, 4H), 1.26 (m, 36H), 0.87 (m, 6H); ^{13}C NMR (400 MHz, $CDCl_3$): δ 150.76, 130.81, 130.02, 129.78, 129.57, 129.11, 127.69, 127.23, 126.41, 124.71, 123.44, 122.74, 122.11, 122.02, 121.51, 74.56, 45.17, 32.10, 30.78, 29.89, 29.86, 29.84, 29.83, 29.55, 26.46, 22.87, 14.30. MS (MALDI-TOF): $[M+H]^+$ calcd. 744.49, found 744.31; Anal. Calcd. for $C_{54}H_{64}O_2$ (744.49): C, 87.05; H, 8.66; Found: C, 86.79; H, 8.42.

Compound 1b. bright yellow solids (30%, mp: 119~120 °C). ^{1}H NMR (400 MHz, $CDCl_3$): δ 9.82 (*dd*, *J* = 12 Hz, 2H), 8.35 (d, *J* = 4 Hz, 2H), 8.30 (d, *J* = 4 Hz, 2H), 8.10 (d, *J* = 2 Hz, 2H), 7.33 (dd, *J* = 12 Hz, 2H), 4.18 (s, 6H), 4.16 (t, *J* = 8 Hz, 4H), 4.09 (s, 6H), 2.03 (t, *J* = 8 Hz, 4H), 1.25 (m, 36H), 0.88 (m, 6H); ^{13}C NMR (400 MHz, $CDCl_3$): δ 158.67, 157.88, 149.62, 132.03, 131.59, 131.29, 130.91, 124.17, 120.35, 120.33, 115.45, 107.90, 107.68, 106.27, 105.16, 74.35, 55.93, 55.62, 32.10, 30.80, 29.91, 29.89, 29.85, 29.55, 26.50, 22.87, 14.29; MS (MALDI-TOF): $[M+H]^+$ calcd. 864.53, found 864.13; Anal. Calcd. for $C_{58}H_{72}O_6$: C, 80.52; H, 8.39; Found: C, 80.56; H, 8.29.

Compound 1c. bright yellow liquid which slowly solidified after a few weeks (15%, mp 58~59 °C). ^{1}H NMR (400 MHz, $CDCl_3$): δ 9.81 (dd, *J* = 12 Hz, 2H), 8.41 (d, *J* = 4 Hz, 2H), 8.34 (d, *J* = 4 Hz, 2H), 8.13 (d, *J* = 2 Hz, 2H), 7.32 (dd, *J* = 12 Hz, 2H), 5.04 (t, *J* = 8 Hz, 2H), 4.90 (t, *J* = 8 Hz, 2H), 4.17 (t, *J* = 8, 4H), 2.03 (t, *J* = 8 Hz, 4H), 1.55 (m, 12H), 1.51 (m, 12H), 1.27 (m, 36H), 0.88 (m, 6H); ^{13}C NMR (400 MHz, $CDCl_3$): δ 156.93, 156.14, 149.53, 132.17, 131.58, 131.32, 130.81, 123.97, 121.19, 120.41, 120.29, 116.51, 110.27, 109.72, 108.86, 74.28, 70.78, 70.19, 32.10, 30.81, 29.91, 29.90, 29.86, 29.56, 26.50, 22.87, 22.48, 22.43, 14.30; MS (MALDI-TOF): $[M+H]^+$

calcd. 976.66, found 976.16; Anal. Calcd. for $C_{66}H_{88}O_6$: C, 81.1; H, 9.07; Found: C, 80.89; H, 8.81.

Compound 1d. *B*-Bromo-9-BBN (1 M solution of dichloromethane, 0.66 mL, 0.66 mmol) was added dropwise to a dichloromethane solution of compound **1c** (0.15 g, 0.15 mmol in 5 mL of CH_2Cl_2) under refluxing. The resulting mixture was refluxed at 45 °C overnight. The reaction mixture was washed with 4 N NaOH solution (three times) and then with water. The organic layer was collected and dried over $MgSO_4$. The crude product obtained by solvent evaporation was further purified by recrystallization from methanol/THF to get the targeted compound as brown solids (0.10 g, 85%). ^{1}H NMR (400 MHz, acetone-d6): δ 9.82 (dd, *J* = 12 Hz, 2H), 9.04 (s, 2H), 8.88 (s, 2H), 8.45 (d, *J* = 4 Hz, 2H), 8.37 (d, *J* = 4 Hz, 2H), 8.18 (d, *J* = 4 Hz, 2H), 7.32 (dd, *J* = 12 Hz, 2H), 4.25 (t, *J* = 8 Hz, 4H), 1.66(t, *J* = 8 Hz, 4H), 1.20 (m, 42H); ^{13}C NMR (400 MHz, $(CD_3)_2CO$): δ 157.84, 157.13, 150.24, 133.19, 132.63, 132.33, 131.82, 123.89, 121.84, 120.97, 120.09, 117.69, 110.38, 109.96, 108.92, 74.84, 32.84, 31.50, 27.28, 23.53, 14.55; MS (MALDI-TOF): $[M+H]^+$ calcd. 808.47, found 808.07; Anal. Calcd. for $C_{54}H_{64}O_6$: C, 80.16; H, 7.97; Found: C, 79.89; H, 8.02.

CHAPTER 2

PHOTOCONDUCTIVITY AND PHOTOVOLTAIC APPLICATIONS OF TRIBENZOPENTAPHENE DERIVATIVES

2.1 Introduction

2.1.1 Introduction of Liquid Crystal Properties

Organic photoconductive materials are attractive due to their potential applications in thin-film transistors, light-emitting diodes, photodetectors, sensors and photovoltaic cells.[18-26, 48] Organic materials have advantages such as low cost and ease in fabricating large thin films using solution processing. The efficiency of these devices depends on the mobility of the charge carriers in the conducting layer. Charge carrier mobility is affected by many factors such as the purity of the molecule, its solubility, its crystallinity, the energy band gap, its optical properties, etc. High charge-carrier mobility in organic materials was observed in organic single crystals of pentacene and rubrene (Figure 2.1), and mobility as high as 35 and 8 $cm^2\ V^{-1}\ S^{-1}$, respectively, has been reported.[49-50] Growing single crystals in thin films is however a challenging task. Vacuum thermal sublimation is a common method for depositing organic thin films. This technique requires expensive setup and is difficult to produce large area thin films. Solution processing, on the other hand, is a low-cost and simple technique that can easily produce large area devices even on a flexible substrate. Solution processed liquid crystalline semiconductor thin films exhibit reasonably high charge carrier mobility (1 $cm^2\ V^{-1}\ S^{-1}$).[51-52] The self-organizational nature of the liquid crystalline phase forms monodomain film easily and is able to self-heal defects of domain structures, offering the possibility of molecular alignment in a large area.[44, 53]

The liquid crystalline phase or mesophase is a state of matter which has intermediate order between the isotropic phase and the crystalline phase. The common structures of molecules which exhibit the thermotropic LC phase consist of a rigid core (rod or disk shaped) and various flexible side chains. The calamitic LCs (rod shaped) have been extensively studied and applied in optoelectronic devices especially in LC displays (LCDs).[54] Discotic LCs with a strong delocalized π system can spontaneously self-organize into columnar or smectic mesophases, and these structures can be used for electronic conduction in one or two dimensions.

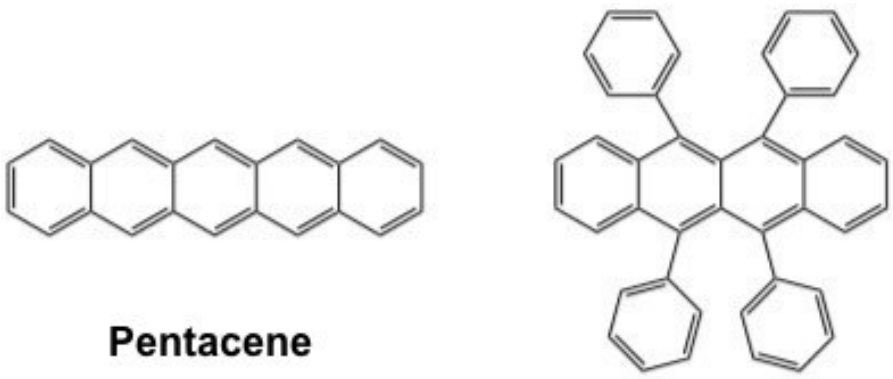

Figure 2.1. The highest charge-carrier mobility of organic semiconductor systems at room temperature 1) pentacene 35 $cm^2 V^{-1} S^{-1}$, 2) rubrene 8 $cm^2 V^{-1} S^{-1}$.

2.1.2 Various Mesophases of Discotic Liquid Crystal

Discotic liquid crystals (DLCs) are composed of rigid disc-shaped aromatic cores surrounded by various flexible alkyl chains. Discotic liquid crystals have attracted great attention from structural, environmental, and more recently, molecular electronics perspectives. Their often planar or near-planar geometry and extended π-delocalization renders them appealing π-π stacking building blocks which can be utilized to dictate controlled self-assembly processes. Most discotic molecules can self-organize one on top of the other into columns in the thermal annealing process. After further organization, columnar mesophases are arranged by two-dimensional lattices of different columns. Columnar phases exhibit different degrees of molecular order. To classify these various columnar mesophases, symmetry and varying degrees of molecular order in the column are considered. The two most common types of columnar phases are the hexagonal columnar phase" (Col_h) (with straight columns) and the "rectangular columnar phase" (Col_r) (with tilted columns). There are a few other ordered phases, such as columnar oblique (Col_{ob}), columnar plastic (Col_p), and columnar helical (H) mesophaes, which are not as common as hexagonal and rectangular mesophases. Figure 2.2 shows the common mesophases of discotic liquid crystals.[55] These mesophases can be identified by various analytical techniques such as polarized optical microscopy (for textural observation), powder X-ray and diffraction,solid-state NMR (for molecular ordering), and differential scanning calorimetry (for phase transition).

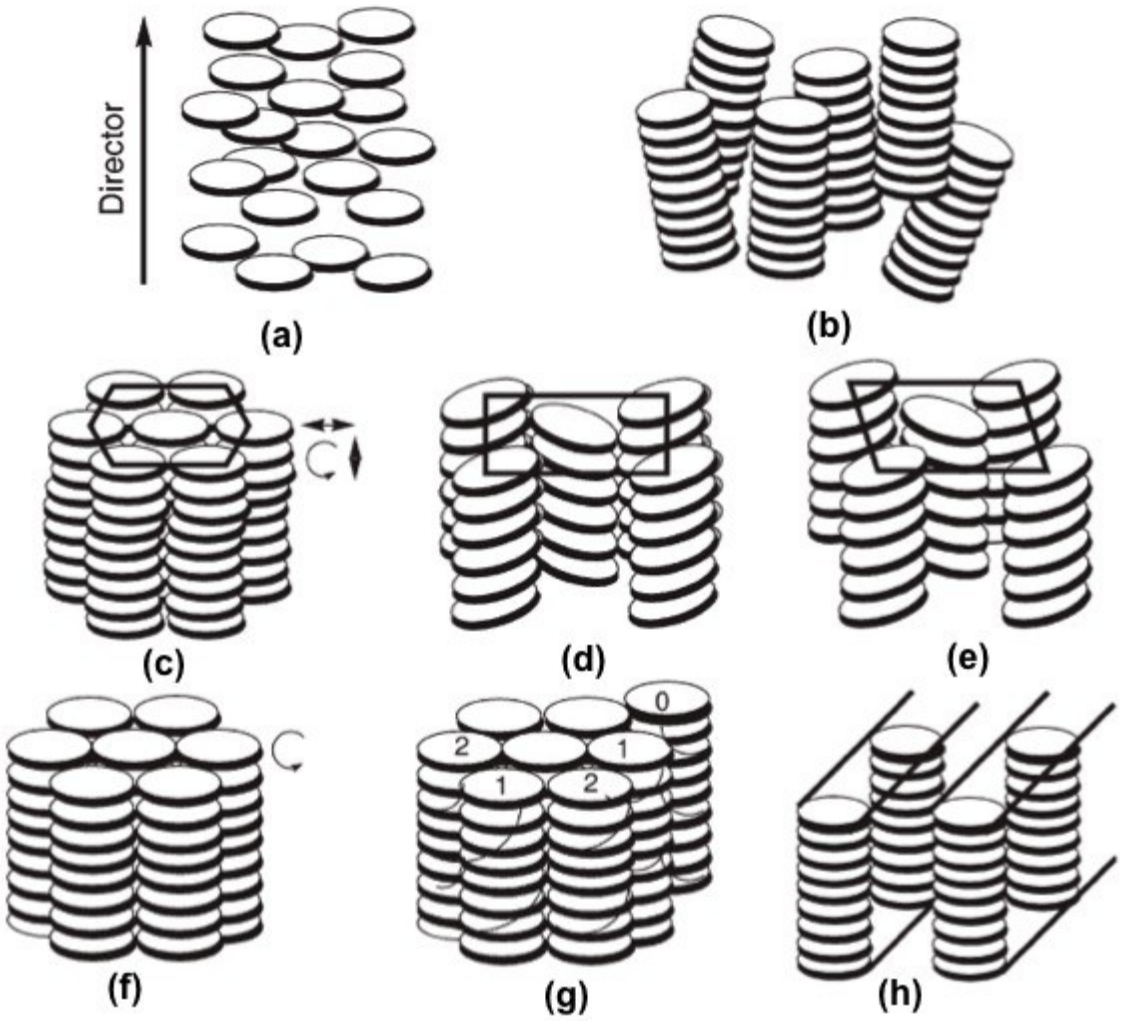

Figure 2.2. Common discotic liquid crystal mesophases. a) discotic nematic, b) columnar nematic, c) hexagonal columnar, d) rectangular columnar, e) columnar oblique, f) columnar plastic, g) columnar helical, and h) columnar lamellar phase.[55]

2.1.3 Charge Transport of Discotic Liquid Crystals in Columnar Mesophases.

In organic conjugated systems, π electrons are delocalized to form semiconducting energy band gaps (1.5 - 3 eV). Physical properties of inorganic and organic semiconductors are quite different because of the extent of variation in orbital overlap along the conducting channel. Inorganic semiconductors have three-dimensional crystalline order, and their frontier orbital interactions form a valence band (VB) and a conduction band (CB). On the other hand, most organic semiconductor materials have weak intermolecular orbital overlap and cannot form a CB and a VB like inorganic materials. Charge carriers in organic materials transport by hopping between neighboring sites. This is why most organic semiconductor materials have lower charge carrier mobility when compared to inorganic semiconductor materials.

Discotic liquid crystals are appealing organic semiconductors because charge transport through the π-stacked columns can be very efficient. Flexible alkyl side chains linked to the rigid core not only increase the solubility in common organic solvents, but also behave as insulators which can decrease the probability for intercolumnar tunneling of the charge carriers leading to one dimension charge transport (Figure 2.3).[56] These discotic molecules can transport the positive hole or negative electron based on the ionization potential or electron affinity. According to these different types of charge transport the materials can be classified as p-type or n-type semiconductors respectively. The charge - carrier mobility of discotic molecules depends on the extent of π-delocalization of the aromatic core and the degree of order in the columnar phase, and can range from 10^{-3} to 1.0 cm^2 V^{-1} S^{-1}. The high charge carrier mobility could be explained by a band-like charge transport that passes through the formation of the

conduction band in several molecules.[57] However, the exact mechanism of the charge transport is still not clear and is under further study.

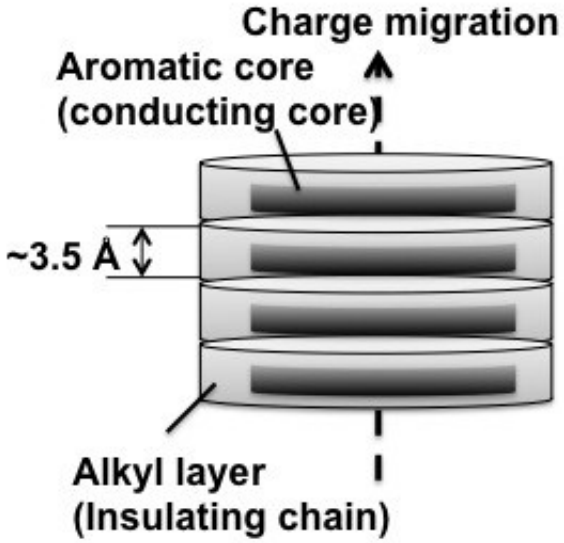

Figure 2.3. Discotic molecules organized into one-dimensional conducting columns.

2.1.4 Methods of Processing Discotic Molecules for Organic Semiconductor Active Layers

Discotic molecules are one-dimensional semiconductors after thermal annealing, so charges and excitons prefer traveling along instead of between the columns. This specific feature implies that appropriate alignment in one direction plays an important role to allow the charge carrier to flow in the column. Discotic liquid crystals can align in two different ways based on the application. For example, OFET applications require planar alignment ("edge on" orientation) of the discotic mesogens, where the discotic cores of molecules are parallel to the substrate surface, while OLED or photovoltaic cells require homeotropic alignment ("face on " orientation), where discotic cores of molecules are perpendicular to the substrate surface (Figure 2.4)[53]. Because the discotic liquid crystal phases have high viscosity, the conventional alignment techniques of calamitic liquid crystal are not very useful.[58] Developing good alignment techniques for discotic LCs is still an active research area.

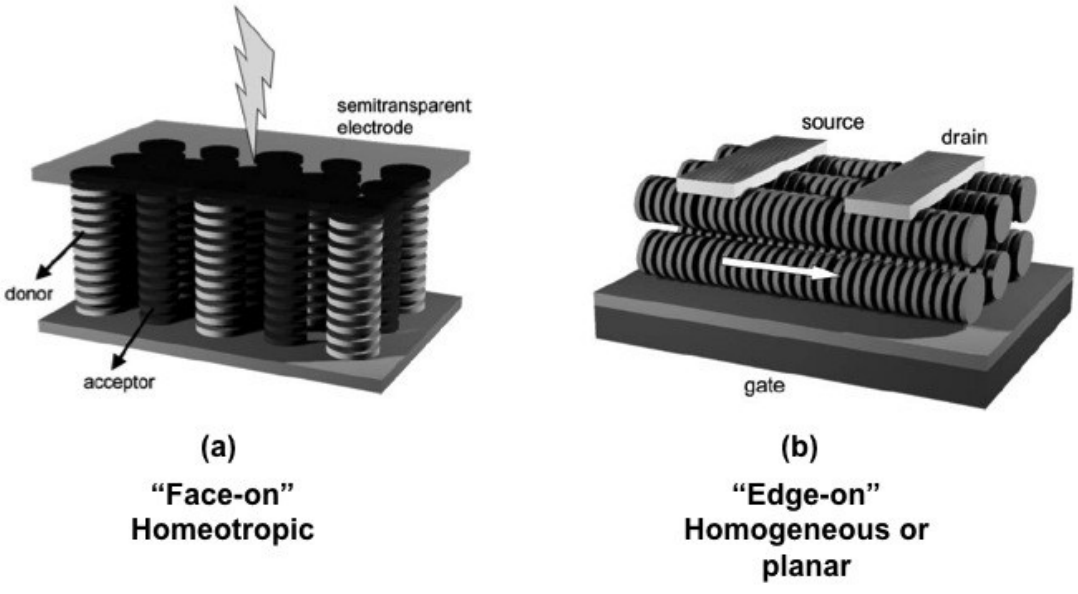

Figure 2.4. Discotic liquid crystals homoetropic a) and planar alignments.[53]

2.1.4.1 Homeotropic Alignment

Compared with planar alignment, homeotropic alignment is easier to implement, and is generally obtained by thermal annealing between two substrates. Some discotic molecules have been shown to homoetropically align in their columnar mesophase spontaneously, such as triphenylene, phthalocyanine, porphyrin, and hexabenzocoronene.[59-63] When these compounds slowly cool down from their isotropic phase, a relatively thick film a few micron thick can be formed. Most molecules require a super slow cooling rate to achieve uniform homeotropic alignment. If the discotic liquid crystals have high viscosity in the columnar mesophases, multiple domains may exhibit in the film and prevent forming good homeotropic alignment in a large area. Two design strategies have been applied to decrease the viscosity. One is to introduce heteroatoms in the flexible side chains and the other is to attach the mesogenic core with sterically hindered groups.

Fabrication of photovoltaic cells and OLEDs requires two electrodes. Generally, the organic conducting layer is deposited on one electrode, followed by the deposition of the second electrode. In this case, the discotic materials should achieve homeotropic alignment in open film where the compounds must come in contact with the air directly before depositing the second electrode. Homeotropic alignment is usually observed between two surfaces, but may be difficult to achieve in one surface. Some studies have shown that homeotropic alignment in a single substrate may be achieved using kinetically controlled thermal annealing for thickness even over 300 nm.[64] The nature of the columnar mesophases and surface treatment also affect the open film properties of homeotropic alignment.[65-68]

2.1.4.2 Planar Alignment

The successful homogeneous alignment of discotic columns were developed in the past decade. A uniaxially aligned thin layer of discotic columns must be well ordered to have high charge carrier mobility. Planar alignment of DLCs has been achieved using various techniques such as PTFE alignment layers[69], zone casting[53], zone crystallization[42], Langmuir-Blodgett (LB) films[73-75], self assembly[83], pulsed infrared irradiation[54], and magnetic field-induced alignment[196.] PTFE alignment layers and zone casting are two techniques suitable for solution processing. In 2002, Zimmermann and coworkers demonstrated planar alignment by spin coating triphenylene with hexagonal columnar mesophases onto a PTFE alignment layer.[69] Later, several HBC derivatives have also been successfully aligned with edge-on orientation in PTFE-coated surface.[20, 70-73] In the planar alignment of the zone casting process, a solution containing the DLC molecule is injected through a nozzle onto a slowly moving glass substrate. Driven by the temperature and concentration gradient created by the moving substrate, the molecules align into uniaxial columns which is parallel to the moving direction (Figure 2.5).[53] The quality of the film morphology depends on the processing conditions that include evaporation temperature, polarity of the solvent, substrate velocity, solvent flow, concentration, and the distance between the nozzle and the glass substrate. Another commonly used method for fabricating ultrathin planar-aligned DLCs is the Langmuir-Blodgett technique. A Langmuir-Boldgett film can control the transfer of organized monolayers of amphiphilic molecules from air/water interface to a solid substrate, and is able to align the molecules “edge-on” by vertical dipping/ raising of the substrate at a constant surface pressure. Some discotic liquid crystals, such as triphenylene and

hexabenzocoronene, were reported to form well-ordered Langmuir-Boldgett films after functionalizing the molecules with hydrophilic side chains.[73-75]

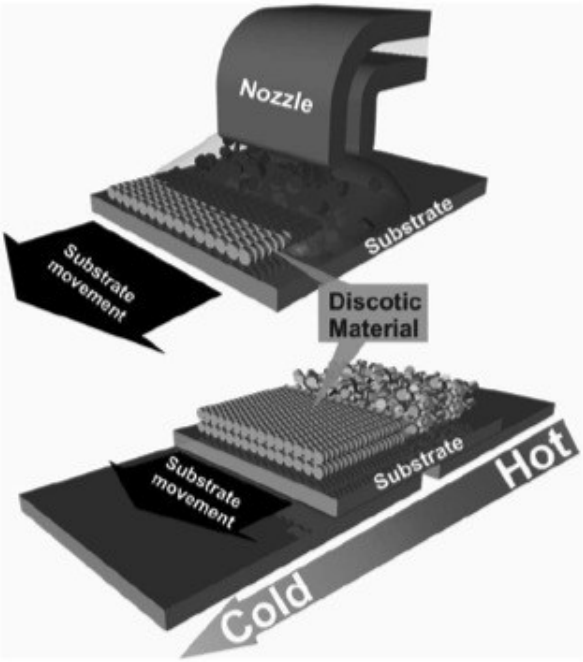

Figure 2.5. Zone Casting technique for discotic materials.[53]

2.1.5 Applications of Discotic Liquid Crystals as Organic Semiconducting

Discotic liquid crystals have promising applications in solar cells, OLEDs, and OFETs. These applications have been developed with good fundamental understanding of charge transport in bulk and in thin films of DLC materials.

2.1.5.1 Photovoltaic Cells of Discotic Liquid Crystals

Photovoltaic cells convert light energy directly into electricity. Photovoltaic devices employing organic semiconductors are usually of p/n-type. A double layer p/n-type photovoltaic cell contains a layer of n-type semiconductor and a layer of p-type semiconductor sandwiched between two electrodes with different work functions. Fig. 2.6 shows the schematic representation of a double layer p/n junction solar cell and its operating principles.[56] In such a device, a built-in electric field is generated by equalization of Fermi energies of two electrodes with flow of electrons from the low-work function electrode to the high-work function electrode. Sunlight is adsorbed by the semiconducting layers, and the built-in electric field can pull the photo-induced charge carriers (electrons and holes) to their corresponding electrodes, generating a current and a voltage. Organic semiconducting materials form tightly bound charge carriers (binding energy around 0.1-0.4 eV) in the form of excitons after adsorbing photons. In most cases, the photo-generated excitons require additional driving forces to dissociate them into separate charges. Exciton dissociation to free charge carriers can occur at the semiconductor/electrode interface and/or donor/acceptor interfaces. In a heterojunction device, two organic semiconductor materials with different electron affinities (LUMO) or ionization potentials (HOMO) were combined. The chemical potential energy created at the donor/acceptor interface is sufficient to overcome the intrinsic exciton-binding

energy. Exciton dissociation at such donor/acceptor interfaces is much more efficient than at the electrode interface. When the exciton reaches the donor-acceptor interfaces, electrons transfer from the LUMO level of the excited donor to the low-lying LUMO level of the acceptor, while holes remain on the HOMO level of the donor, thereby forming a polaron pair. When the dissociated holes and electrons move to their respective electrode driven by the built-in electric field, the current is produced. It is desirable for organic materials to have a long exciton diffusion length and high carrier mobility. Solar spectral coverage is another important parameter for efficient photovoltaic cells. The broader the absorption spectral range of the organic materials is, the higher the efficiency of the device can be. Another important characteristics to be considered is the relative energy levels of donor and acceptor molecules. The potential output or open circuit voltage of the device is related to the energy gap between HOMO of the donor and LUMO of acceptor. Overall, the efficiency of a photovoltaic cell depends on the efficiencies of light absorption, exciton dissociation, charge transport and charge collection at the electrodes.[76]

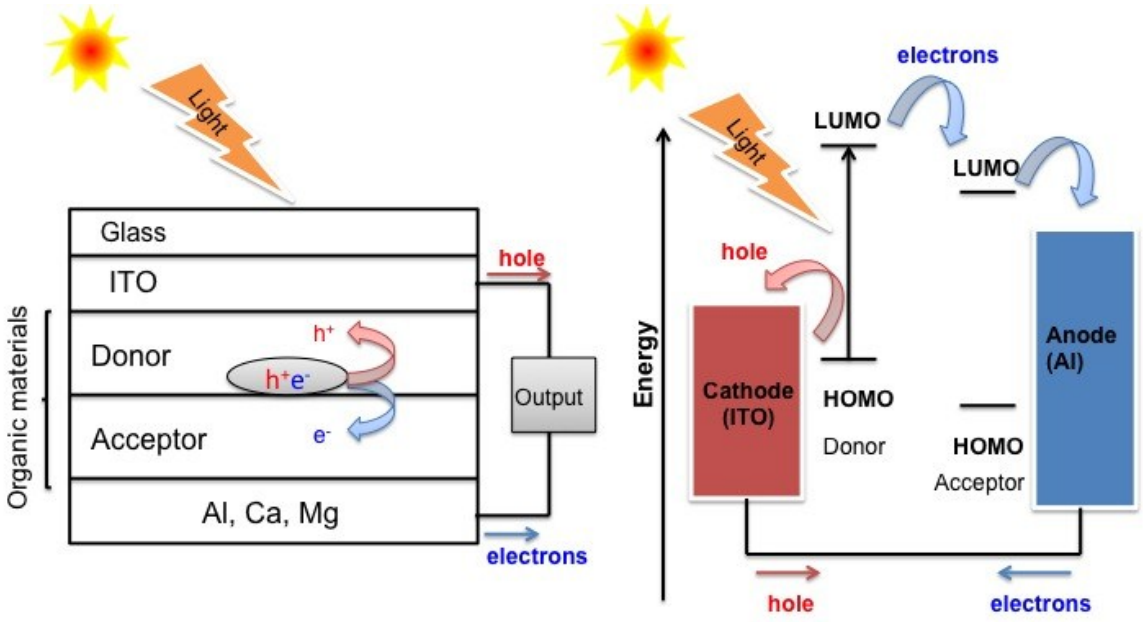

Figure 2.6. Organic heterojunction solar cell (left) and energy level diagram (right).

In 1986, the first organic photovoltaic cell using the concept of a heterojunction (Figure 2.7) was introduced by Tang.[77] He used two different dyes to fabricate a bilayer device, and power conversion efficiency reached 1% which is one order of magnitude higher than those of a single material OPV cell at that time. The morphology of the donor and acceptor interface was recognized as a critical factor to the performance of heterojunction photovoltaic cells. In 1995, Heeger and coworkers introduce the new concept of bulk heterojunction (BHJ) photovoltaic cells (Figure 2.7) to increase the donor and acceptor interfaces.[78] The bulk heterojunction consists of well-blended donor and aceeptor materials forming interpenetrating networks of donors and acceptors. The advantage is that the charge carriers have unrestricted conduction pathways to their respective electrode.

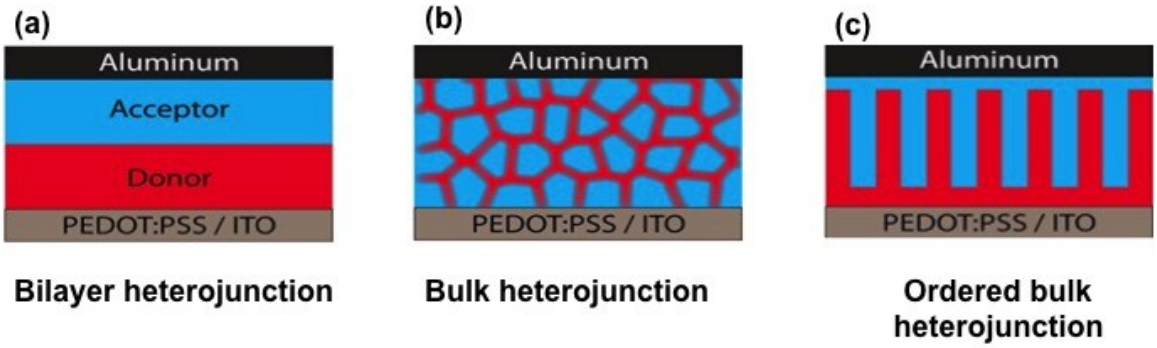

Figure 2.7. Schematic diagram of different heterojunction methods of photovoltaic cells a) Bilayer heterojunction, b) Bulk heterojunction, c) Ordered bulk heterojunction.

Columnar discotic liquid crystals as semiconducting materials in photovoltaic cells have distinct advantages because they exhibit large exciton diffusion length and high charge carrier mobility in their highly ordered columnar mesophase. The first discotic liquid crystal-based photovoltaic cell was fabricated by 1990 by Gregg and coworkers who sandwiched a thin film of porphyrin between two ITO-coated glass electrodes.[79] In 2001, Schmidt-Mende and coworkers used hexabenzocoronene as the electron donor and perylene tetracarboxylic diimide (PTCDI) as the electron acceptor in a bulk heterojunction device . The power conversion efficiency reached 2 % under monochromatic illumination (490 nm).[80] The nanophase separation of PTCDI and hexabenzocoronene in the blend film provided separate percolation pathways for the electron and hole transport, leading to the significantly improved device performance.

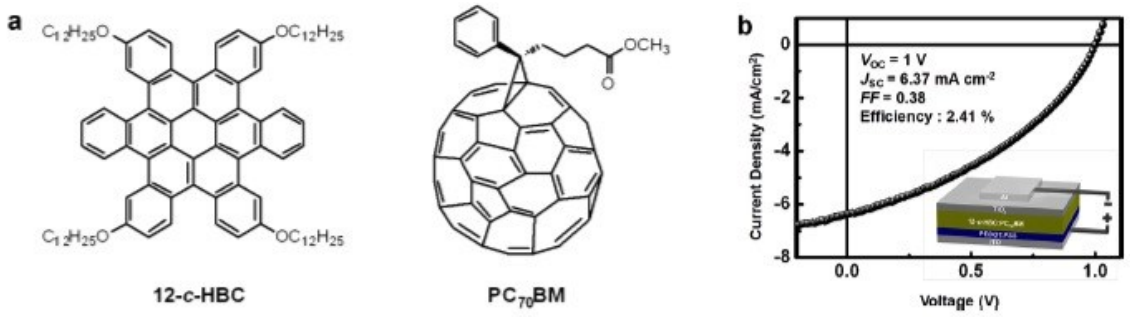

Figure 2.8. a) Chemical structure of donor and acceptor, b) *J-V* characteristic of 12-c-HBC/$PC_{70}BM$ device under light illumination.[81]

Kang and coworkers designed donor (dodecyloxy-substituted contorted hexabenzocoronene) and acceptor ($PC_{70}BM$) materials with complementary shapes to improve their assembly (Figure 2.8). Using the strategy of complementary shapes, they created a well-defined interface between donor and acceptor and the power conversion efficiency reached 2.41 % under light illumination.[81]

In order to optimize the degree of phase separation and to control the domain size in blended donor and acceptor systems, covalently linked donor and acceptor molecules have been explored.[82] Although D-A linked polymeric systems are well known for OPV device applications, it is only recently that researchers have begun to focus on such hybridized columnar discotic systems.[83-85] In 2006 Takuzo Aida and his group reported a promising design using a large hexabenzocoronene (HBC) derivative covalently linked with a trinitrofluorenone (TNF) acceptor (Figure 2.9).[82] This compound self-assembles into nanotube with separated HBC and TNF layers. The coaxial donor-acceptor system provided an excellent design strategy to achieve large interface for spatially segregated redox couples.

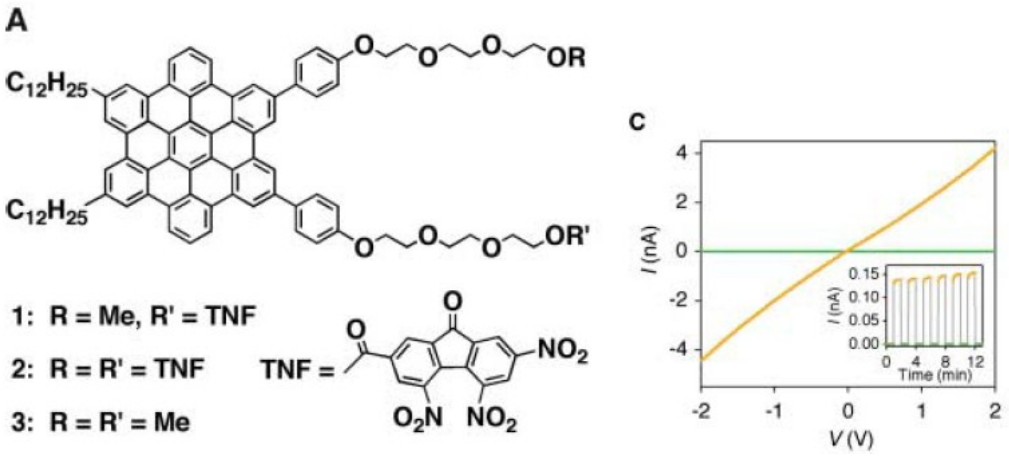

Figure 2.9. Molecular structur of HBC with TNF (left). I-V curve of HBC-TNF at 25 ^{o}C with and without photoirradiation.[82]

The transient photoconductivity ($\Delta\sigma$) reached a high value (Δ_{max}) of 13 μS m^{-1} in 0.11 μs. One disadvantage for covalently linked D-A system is its synthetic difficulty. In recent years, self-assembly has proven to be a convenient method for constructing well-defined nanostructures, and a few examples have been reported on the design and fabrication of nanostructured heterojunction systems through molecular self-assembly.[86-88] In 2011, Zang developed a simple and general method to improve photoconductivity.[88] They used self-assembled nanofibril electron acceptors which were then coated with electron donors on the surface of acceptors to fabricate photoconductive materials (Figure 2.10). This method allows facile control of the domain size. The donor and acceptor molecules are held together by non-covalently bonds though alkyl chain interdigitation.

2.2 Objectives

The four newly designed tribenzopentaphene derivatives have been explored as photoinduced electron donors coated on self-assembled perylenediimide (PDI) nanofibrils. The effect of various alkoxy side chains on their molecular aggregation behavior and the subsequent effect on the photoinduced charge separation process at the nanofibril heterojunction has been systematically studied. Solar cells based on tribenzopentaphene/PCBM or PDI heterojunctions have been fabricated and evaluated.

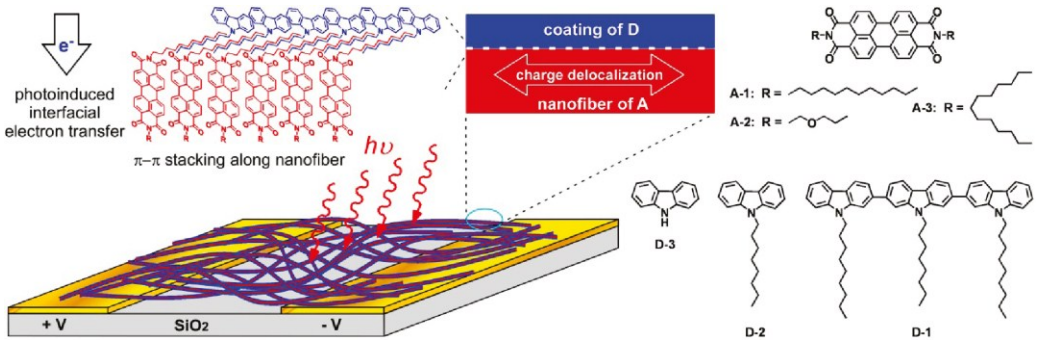

Figure 2.10. Illustration of nanofibril heterojunctions composed of electron donor (D)-coated nanofibers that function as electron acceptors (A).[88]

2.3 Photoconductivity of Tribenzopentaphene-Perylenediimide Nanofibril Heterojunctions

2.3.1 TBP and Perylene Tetracarboxylic Diimide (PTCDI) System

The four tribenopentaphene (TBP) derivatives were used for electron donors in the photoconductivity studies (Scheme 2.1). The two linear long alkyl chains in TBP molecules help anchor the donor molecules onto the nanofiber of PTCDI by hydrophotobic alkyl chain interdigitation.[88-90] Meanwhile, the various the intermolecular

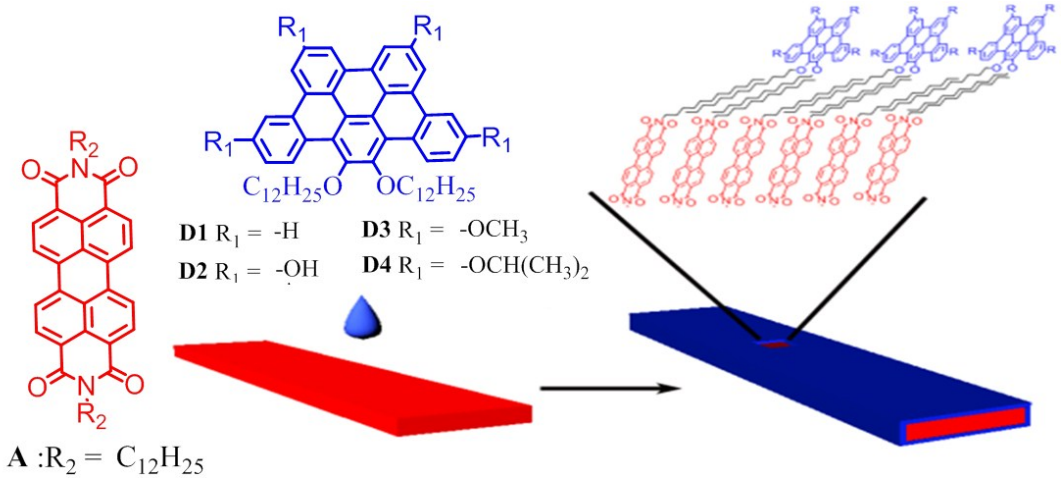

Scheme 2.1. Schematic illustration of core-shell structured nanofibril heterojunction composed of D1-D4 coating and PTCDI nanofiber.peripheral side chains can modulate

interactions, leading to different aggregated morphologies and electronic properties.[91] In order to elucidate the molecular structural effect, solvent vapor annealing can be used to facilitate the self-assembly process. Because solvent vapor annealing can improve crystallinity and charge carrier mobility in organic semiconductor materials and devices, the technique has been widely studied in the past few years.[92-95] Among the four TBP

molecules, **D4**, which has the largest bulkier side groups is expected to have the most severe steric hindrance to interrupt the π–π stacking. The other three TBP molecules possess relatively small side groups. As shown in Figure 2.11, the strength of intermolecular aggregation in the four TBP molecules exhibits a huge effect on photocurrent response of the core PTCDI nanfibers. When PTCDI nanofibers were coated with **D4**, which has negligible π–π stacking even after solvent annealing, the highest photocurrent response was obtained. However with the coating of **D1**, **D2** and **D3** of TBP molecules, the PTCDI nanofiber showed significantly lower photocurrent response. The difference of photocurrent response between **D4** and the other three TBPs became more significant after solvent vapor annealing.

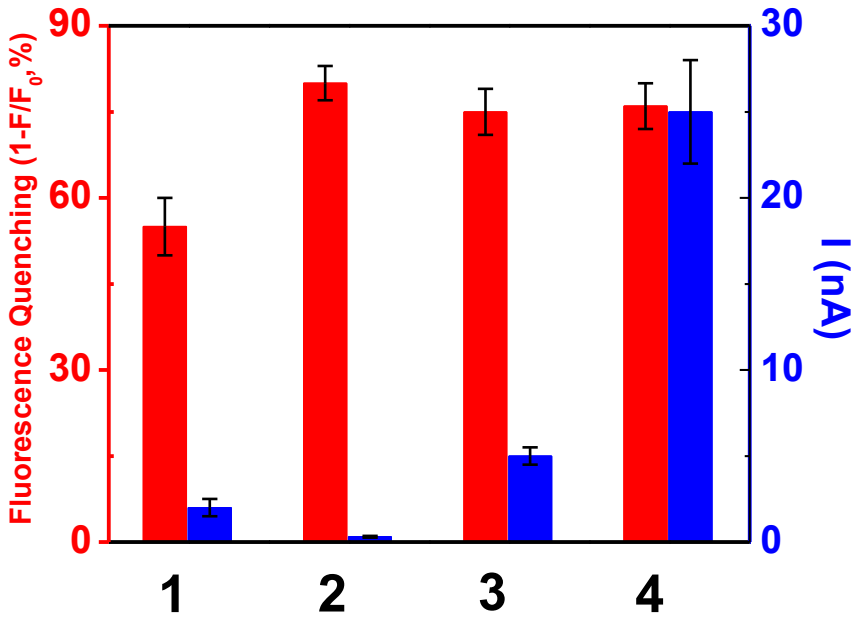

Figure 2.11. Comparison of fluorescence quenching (red) and photocurrent generation (blue) between the PTCDI nanofibers coated with one of the four donor molecules, **D1-D4**.

The nanofibers of PTCDI were fabricated by the previously published self-assembly procedure.[88] In order to ensure strong hydrophobic alkyl chain interdigitation with the four TBP molecules, this PTCDI molecule also includes a dodecyl chain on both imide positions. The TBPs were coated on the surface of PTCDI nanofibers by the drop casting method previously employed for creating similar nanofibril heterojunctions.[88] The nanofibers have well-defined morphologies to provide a large interface for the adsorption of TBP molecules. The in-situ AFM images of PTCDI nanofibers before and after coating with **D4** molecules were presented in Figure 2.12. The PTCDI nanofibers were fully coated with **D4** molecules after drop casting, and very little residue was left on the silicon oxide substrate. Similar results were obtained for **D2**-coated PTCDI nanofibers (Figure 2.13). The strong hydrophobic interdigitation between the dodecyl chains of TBP and that of PTCDI molecules on the nanofiber surface are crucial in bringing TBP and PTCDI together. The morphology of individual nanofibers maintains the same after drop casting, indicating the robustness of nanofibril structures on the substrate. Such a feature enables comparative studies of PTCDI nanofibers modified with different TBP molecules, allowing the pinpointing of different photocurrent response to the surfaced-coated D molecules.

Figure 2.14a shows the fluorescence spectra of the PTCDI fibers before and after **D4** coating. 80% of the PTCDI fluorescence is quenched after **D4** molecule coating, indicating efficient photoinduced electron transfer from **D4** to the excited PTCDI molecule.

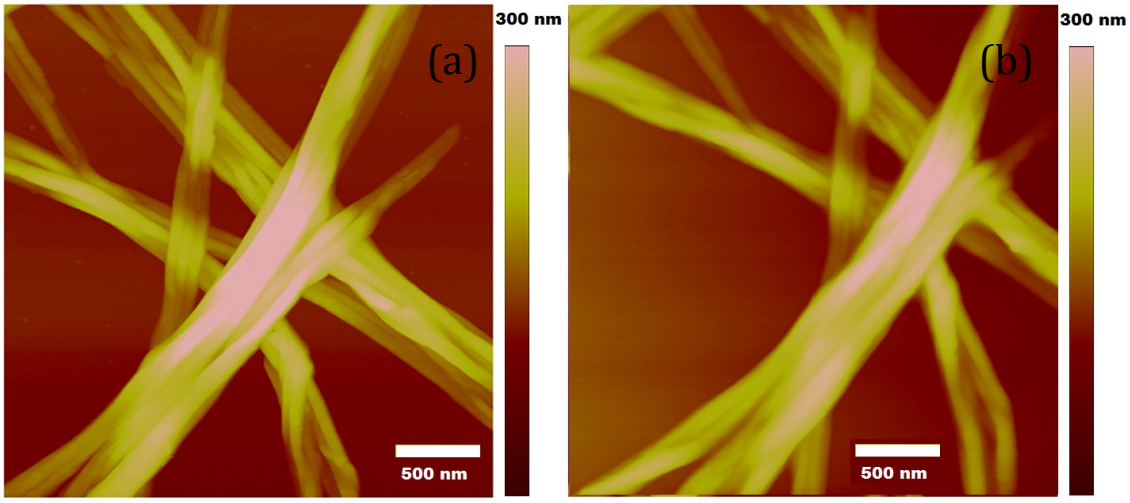

Figure 2.12. AFM images of PTCDI nanofibers (molecular amount of 7 nmol) deposited on a 5 mm × 5 mm silicon wafer covered with 300-nm thick SiO_2 before (a) and after (b) surface coating of **D4** (4 nmol).

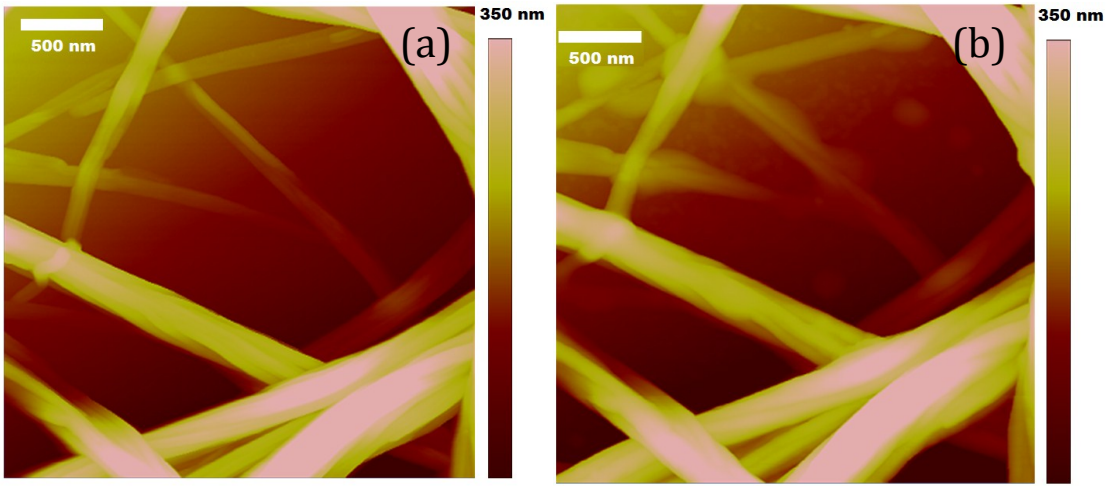

Figure 2.13. AFM images of PTCDI nanofibers drop-cast on the surface of silicon wafer covered with 300-nm thick SiO_2 before (a) and after (b) coating with **D2**.

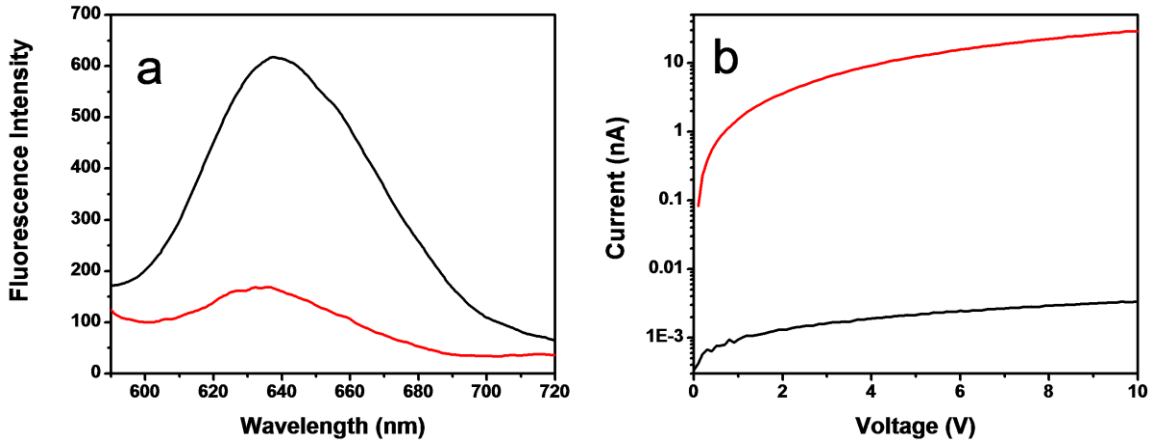

Figure 2.14. (a) Fluorescence spectra of PTCDI nanofibers shown in Figure 2.12 before (black) and after (red) drop-casting of D4. (b) I-V curves measured over the D4 coated PTCDI nanofibers in the dark (black) and under white light irradiation of 0.17 mW/cm^2 (red).

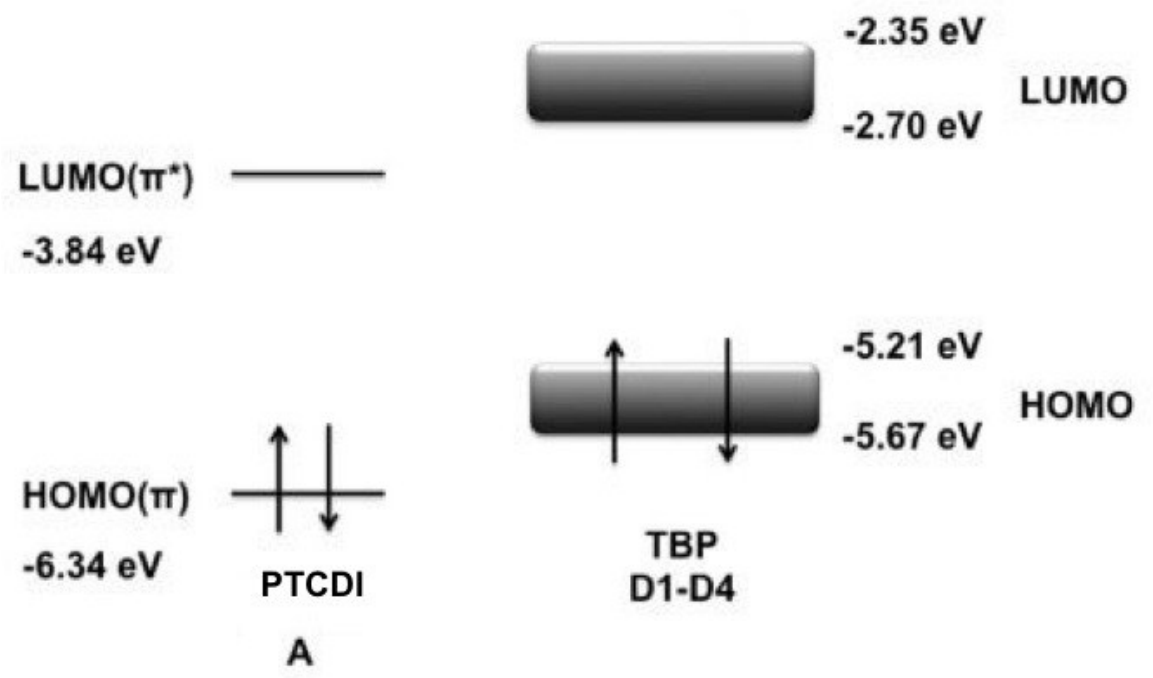

Figure 2.15. Electronic energy levels of PTCDI and TBP (PAH).

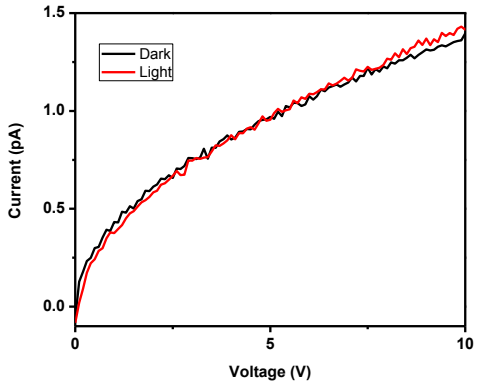

Figure 2.16. I-V curves measured for **D4** film in dark (black) and under light illumination (red). Experimental conditions are the same as in Figure 2.14.

The driving force of photoinduced electron transfer is 1.13 eV, which is thermodynamically favored, and it is calculated between the HOMO levels of **D4** and PTCDI molecules (Figure 2.15).

Figure 2.14b shows the photoconductivity response of the **D4**/PTCDI nanofibrial heterojunction. An on/off ratio of ca. 10^4 was obtained under a 10 V bias. Pure **D4** film or pure PTCDI fibrils showed photocurrent response of at least three orders of magnitude lower (around 1 pA under 10 V bias, Figure 2.16).

To study the effect of the molecular structure of TBP on the photoconductivity in nanofibrial heterojunctions, the same experiments as **D4**/ PTCDI system were also performed via coating **D1~D3** on PTCDI nanofibers. Figure 2.11 summarizes the results of fluorescence quenching and photocurrent measurements of the four TBP / PTCDI nanofibers. While all four TBP molecules show comparable fluorescence quenching, the photocurrent shows significant difference. The **D4**/PTCDI nanfiber gave the highest photocurrent compared with **D1**-**D3**/PTCDI. The efficient fluorescence quenching is consistent due to the energetically favorable forward electron transfer from all TBP

molecules to the photoexcited PTCDI where the driving force was calculated to be in the range of 0.7-1.1 eV (Figure 2.15). However, efficient forward electron transfer does not necessarily produce high electrical current, which also depends on other factors such as the subsequent charge separation of the photogenerated D^+-A^- pair to free charge carriers and the charge carrier mobility. Charge recombination (or back electron transfer) within D^+-A^- pair is often one of the major reasons for low photocurrent. It is particularly intriguing to compare **D3** and **D4**. Both have alkoxy side groups and very close HOMO levels. When coated on PTCDI fibers, they exhibit identical extent of fluorescence quenching. The photocurrent response of the two heterojunctions, however, differ by almost five times. The difference in photocurrent was even more dramatic for the nanofibers coated with **D1** and **D2**, which showed photocurrent values more than 10 and 50 times, respectively lower than that of **D4**-coated fibers (Figure 2.11). Considering the similar fluorescence quenching efficiency among the four nanofibers, we suspected that the lower photocurrent observed with the nanofibers coated with **D1**-**D3** (compared to that of **D4**) was primarily due to the less efficient charge separation (or faster charge recombination) of the photogenerated D^+-A^- pair, which has something to do with the phase segregation of surface-coated D molecules. The bulky side group of **D4** prevents intermolecular π–π stacking, resulting in uniform molecular distribution of **D4** onto the PTCDI nanofibers (Scheme 2.2). In contrast, **D1**-**D3**, with relatively small side groups, are prone to π–π stacking, which leads to the formation of segregated phases of aggregated D molecules. AFM images of the drop-cast films of **D1**-**D3** confirmed their self-assembly. Particularly for **D1** and **D3**, the preferred columnar stacking enabled formation of nanofibril structures (Figure 2.17 and 2.18).

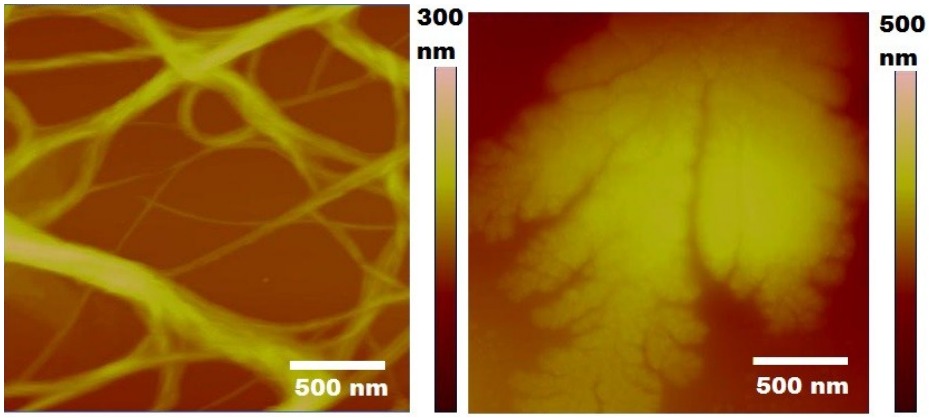

Figure 2.17. AFM images of **D1** (a) and **D2** (b) drop-cast on the surface of silicon wafer covered with 300-nm thick SiO_2.

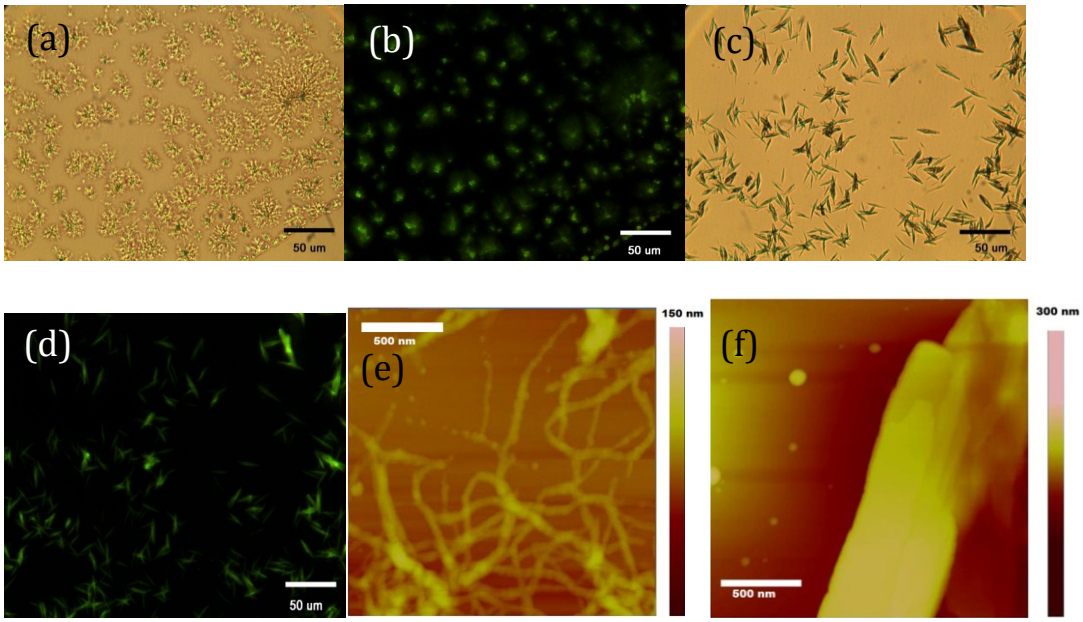

Figure 2.18. Bright field microscopy (a,c) and fluorescence microscopy images (b,d) of **D3** drop-cast on OTS modified glass surface before (a,b) and after (c,d) ethanol vapor annealing. AFM images of the same sample before (e) and after (f) ethanol vapor annealing.

Results in Figure 2.11 indicate that aggregates of **D1-D3** can quench the fluorescence of PTCDI nanofiber with comparable efficiency as the homogeneously coated **D4**. The exciton migration length within crystalline PTCDI nanofibers can be long, in some cases reaching hundreds of nanometers.[89,96] When the quenchers, such as molecules or aggregates, are distributed on the fibrile surface with sufficient density, the fluorescence of nanofibers can be effectively quenched, as a migrating exciton can always encounter a quencher within its lifetime. In our studies, the ratio of D/A is up to 4/7. It is reasonable to assume that the aggregates of **D1-D3** can fully cover the PTCDI nanofiber with enough density, and the separation between their aggregates is much smaller than exciton migration distance of PTCDI.

Although the aggregation of **D1-D3** can quench the fluorescence of PTCDI, the photocurrent response of D1-D3 coated PTCI fibrils is much lower than that of the **D4**/PTCDI system. The reason could be the locally enhanced recombination (rather than separation) of D^+-A^- charge pair photogenerated around the aggregate of TBP molecules (Scheme 2.2b). The intermolecular electron delocalization among π-π stacked PTCDI molecules primarily causes the interfacial charge separation of D^+-A^- at the PTCDI nanofiber[83,88,97] and this charge delocalization can be further extended under electrical bias applied to the nanofiber. At the fibril section with an aggregated D domain, there may be multiple pairs of D^+-A^- photogenerated by quenching multiple excitons (as discussed above), making the electron delocalization along the PTCDI stacks more difficult due to the increased charge density.[98-99] Moreover, multiple charge pairs form a

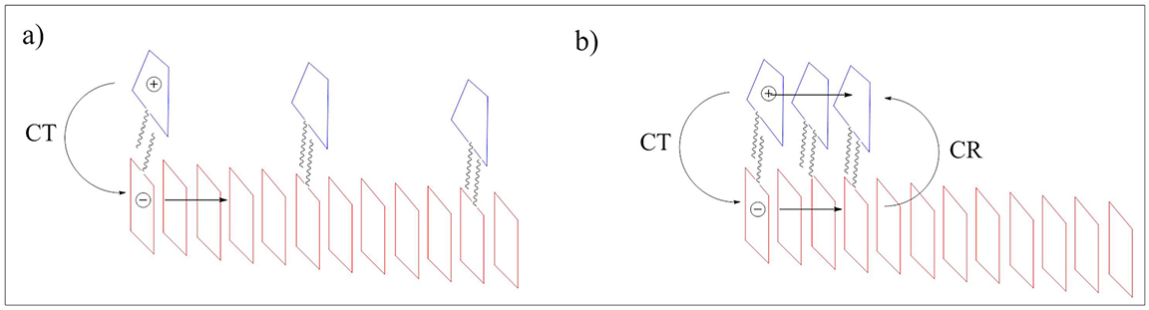

Scheme 2.2. A schematic comparison of the charge recombination process in a PDI fiber coated with nonaggregating PAH donors (**D4**) (a) and aggregated PAH donors (**D1**-**D3**)(b).

strong local electrical field, which can prevent the charge separation. Thus, the charge recombination of D^+-A is enhanced by the above two effects. On the other hand, **D4** with homogenous coating can have more uniform distribution of D^+-A^- pairs on the PTCDI nanofibers (Scheme 2.2a) which can be effectively separated through the intermolecular electron delocalization along the nanofiber, leading to high photocurrent response shown in Figure 2.11.

It is worth noting that **D2/PTCDI** showed the lowest photocurrent response, although the fluorescence quenching efficiency of **D2** is the highest. The lowering of photoconductivity is likely due to the hydroxyl side groups of **D2** (-OH), which affords redox interaction with electrons, functioning as a charge carrier trap as previously observed in n-type organic field effect transistors.[100-102]

Due to fast evaporation of solvents during the drop casting process, it is often hard to produce the thermodynamically stable (energy minimized) state. Large number of defects and grain boundaries can be formed during the rapid assembly of molecules, and

the growth of small nuclei may be quenched when the solvent is dried. Post-assembly treatment, like solvent vapor annealing (i.e., aging of organic materials in saturated solvent vapor), has proven to be an effective method to reorganize and optimize the intermolecular arrangement, and facilitate the phase growth to reach the thermodynamic stable state.[103-105]

Indeed, solvent vapor annealing has been commonly used in solar cell materials processing to improve the crystalline organization of D and A phases, with the aim to facilitate the charge transportation.[106] We expected that the above mentioned difference of photocurrent between the nanofibers coated with **D4** and **D1-D3** would be more profound if the nanofibers were subject to solvent vapor annealing, considering that the difference of phase morphology and its dependence on the molecular structure between **D4** and **D1-D3** can be maximized at the thermodynamic stable state.

Because of similar HOMO level and alkoxy side chains, **D3** was chosen as a model compound of **D1**-**D3** to study the effects of solvent vapor annealing on the surface aggregation and the subsequent photoconductivity. The results were compared to **D4** in the same conditions. The annealing was performed in ethanol vapor, because ethanol is a good solvent for **D1**-**D4** but a poor one for PTCDI. PTCDI nanofibers are expected to maintain the same crystalline structure after solvent annealing. Interestingly, **D3** and **D4** coatings showed dramatically different transitions of the aggregation state under the same annealing conditions. The optical microscopy images of **D3 coated PTCDI** showed the growth from small aggregations to large needle-like structures (Figure 2.18). AFM images show that the small aggregates are actually composed of fine nanofibrial structures which were formed during the drop-cast process. Formation of nanofibiril

structures indicate that the **D3** molecule has strong π–π stacking, which is consistent with its planar geometry of TBP's π-conjugation. When continuously annealed for a longer time, the small nanofibers grew into needle-like chunks, though still retaining in an elongated shape (Figure 2.18). This observation indicates that **D3** is prone to crystallize into large elongated structures driven by the strong π-π stacking interaction. The **D4** coating on the other hand showed no obvious aggregation even after solvent vapor annealing (Figure 2.19).

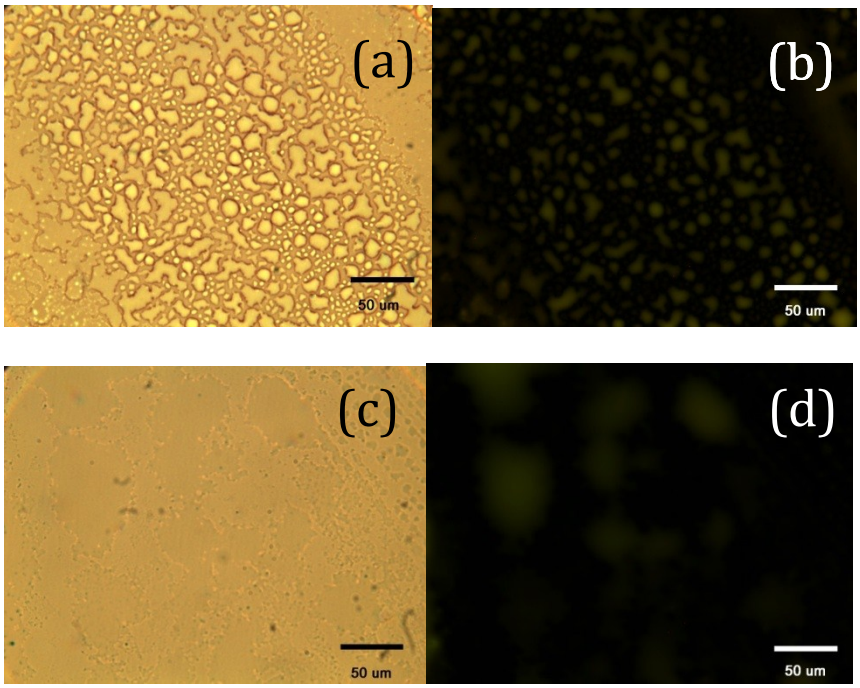

Figure 2.19. Bright field microscopy (a,c) and fluorescence microscopy images (b,d) of **D4** drop-cast on OTS modified glass surface before (a,b) and after (c,d) ethanol vapor annealing.

The different aggregation behavior of **D3** and **D4** under solvent vapor annealing led to distinct effects on the photocurrent response as measured over PTCDI nanofibers coated with these two molecules (Figure 2.20a). For D4, the photocurrent increased up to 60% after solvent annealing; however, for **D3** the photocurrent decreased to 14% of its preannealing value. The significant decrease in photoconductivity of **D3**/PTCDI nanofiber is likely caused by the increased **D3** molecule aggregations induced by the solvent vapor annealing. As discussed above, the enlarged aggregated domains of D molecules are detrimental to the charge separation of D+-A- pairs because of the enhanced local electrical field. In contrast, for **D4**/PTCDI nanofiber the bulky isopropoxyl substitution at **D4** prevents molecular aggregation, instead favors the homogeneous distribution of molecules on surface. Such molecular distribution can be further facilitated under solvent vapor annealing, producing a coating layer with minimized aggregation, as indicated by the 60% increase in photocurrent shown in Figure 2.20. The solid-state fluorescence spectral measurements on a thin **D4** film further support this annealing-enhanced molecular distribution of **D4**. The glass slide was pre-treated with trichloro(octadecyl)silane (OTS) to create a similar hydrophobic surface environment as PTCDI nanofiber. Before solvent vapor annealing, the fluorescence spectrum of **D4** film exhibit a major peak at 465 nm, with a shoulder peak at 440nm (Figure 2.20 b).

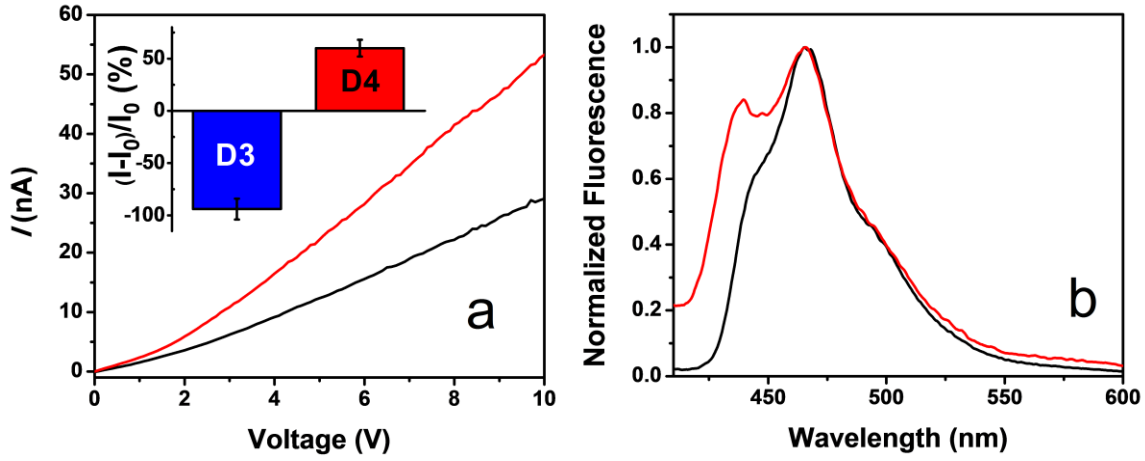

Figure 2.20. (a) I-V curves measured over **D4** coated PTCDI nanofibers under the same light irradiation as employed in Figure 2.14 before (black) and after (red) solvent vapor annealing. Inset: relative photocurrent change (in percentage) for **D3** and **D4** coated nanofibers after solvent vapor annealing. Photocurrent values used in this plot were obtained at a bias voltage of 10 V. (b) Fluorescence spectra of **D4** drop-cast on a glass surface modified with trichloro(octadecyl)silane (OTS) before (black) and after (red) solvent vapor annealing. The two spectra are normalized at 465 nm.

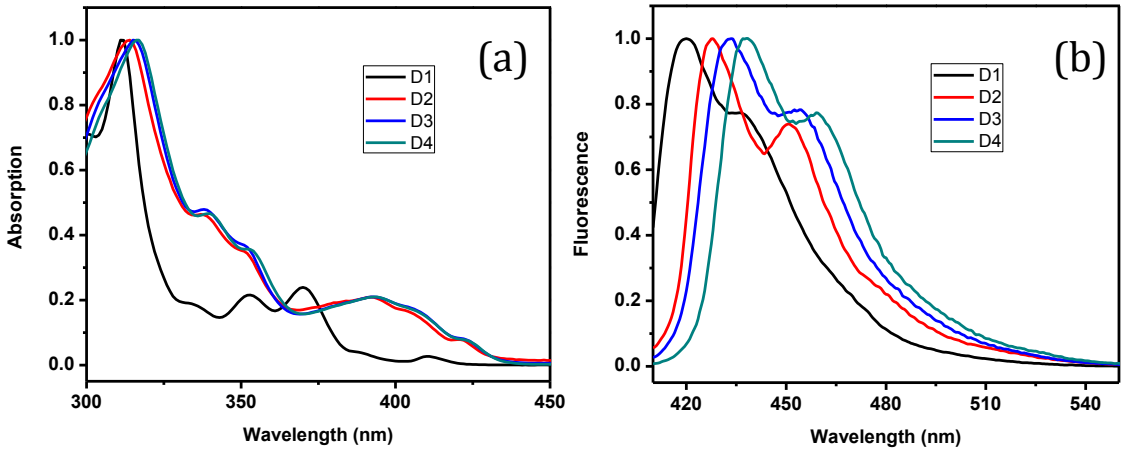

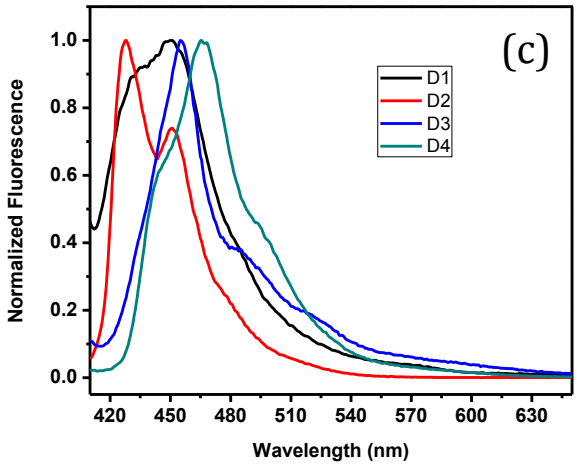

Figure 2.21. Normalized absorption (a) and fluorescence spectra (b) of **D1-D4** in ethanol solution, (c) Normalized fluorescence spectra of **D1-D4** drop-cast on glass surface.

Compared to the fluorescence spectrum of **D4** (Figure 2.21), the fluorescence emission becomes more dominant in solid state at longer wavelength (Figure 2.20 b), which is consistent with enhanced intermolecular interaction, as commonly observed for molecular assemblies. The emission at 440 nm (characteristic of the fluorescence of individual molecules) remains in the solid film of **D4**, indicating the relatively weak intermolecular π–π interaction in comparison with the film of **D3**, where the strong π–π stacking results in almost no emission observed for the individual molecules (Figure 2.21). After solvent vapor annealing, the peak of **D4** film at 440 nm was significantly enhanced (Figure 2.20 b), implying more molecules originally "frozen" as aggregates during the fast evaporation of drop-casting now transformed into homogeneous molecular distribution. In contrast, for **D3** film there was no obvious change observed in the fluorescence spectrum upon solvent vapor annealing under the same condition (Figure 2.22). This is consistent with the strong intermolecular π–π stacking, which leads to the formation of stable aggregates in the specific nanofibril morphology (Figure 2.18).

Although solvent vapor annealing facilitates growth of the nanofibers of **D3** into larger elongated crystals, the electronic property of the solid phase still remains dominant with the π–π stacking as indicated by the unchanged fluorescence spectra.

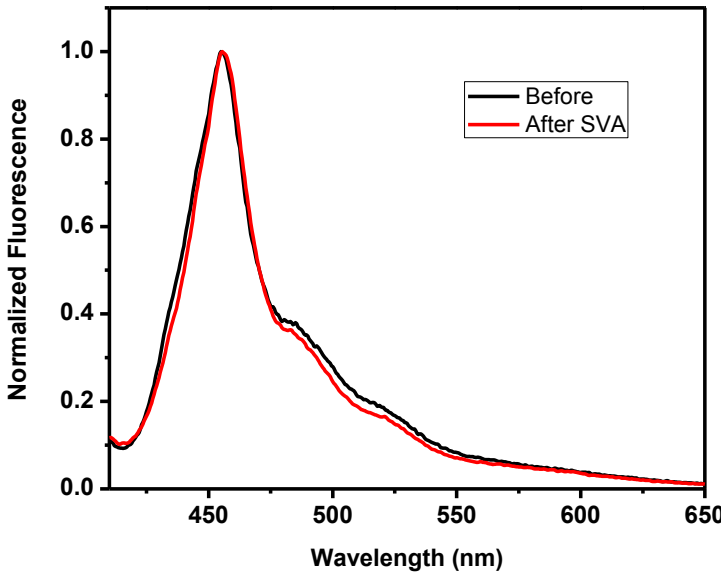

Figure 2.22. Fluorescence spectra recorded on **D3** film deposited on OTS modified glass surface before (black) and after (red) solvent vapor annealing

2.3.2 Interfacial Influence on the Photoconductivity between TBPs and PDIs

To demonstrate that alky chain interdigitation plays an essential role in bringing the TBP donor and PTCDI acceptor together, PTCDI derivatives with different side chains at the imido positions have been used to fabricate PTCDI/TBP fibril heterojunctions. (Scheme 2.3).

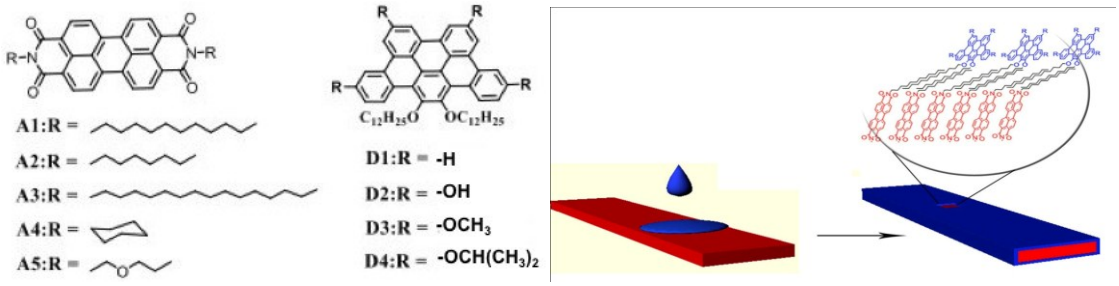

Scheme 2.3. Five different substituted PDI derivatives as electron acceptors and tribenzoperylene derivatives as electron donor (left). The concept of coated method (right).

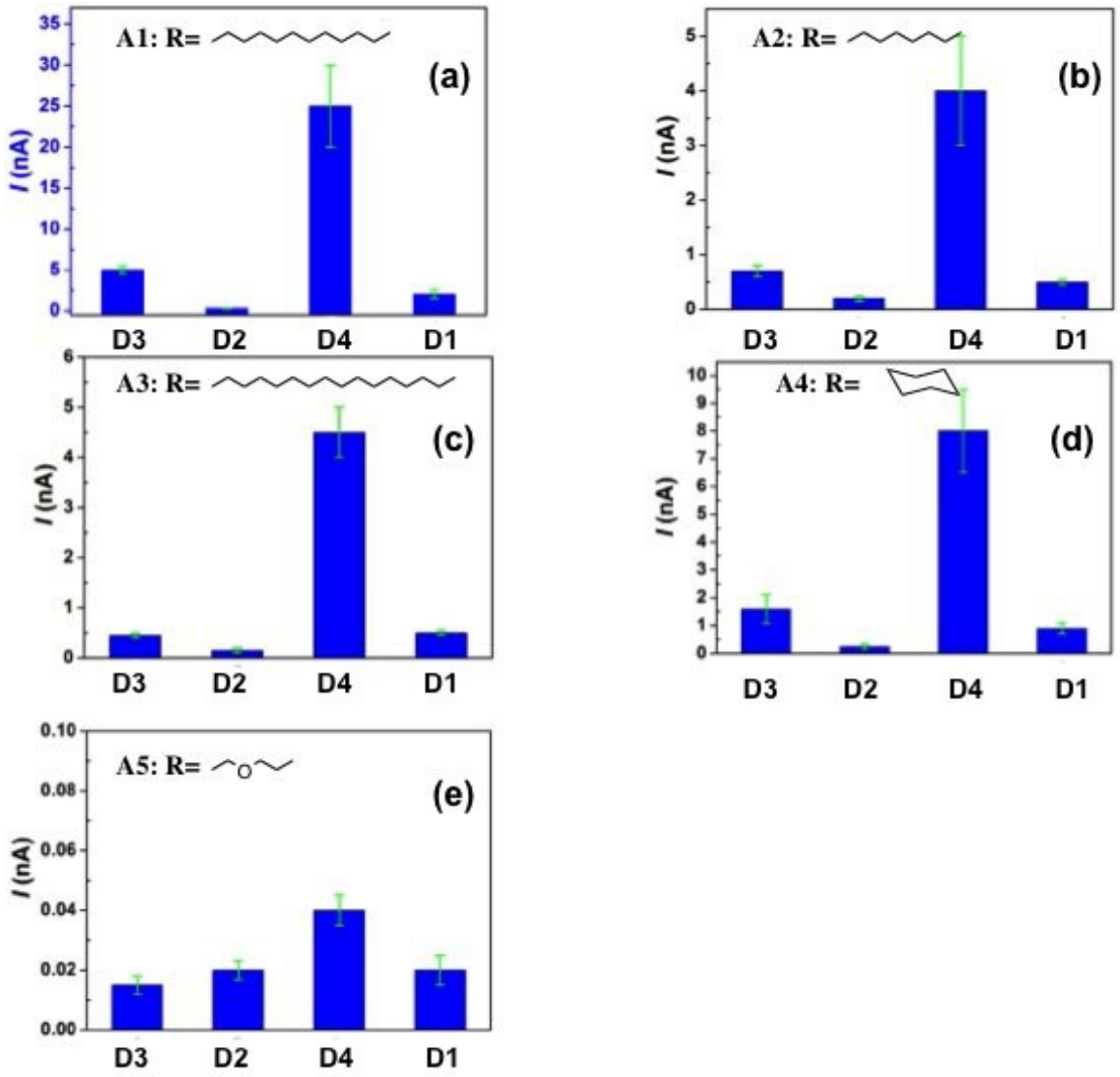

Figure 2.23. Comparison photocurrent generation between the various functionalized PDI nanofibers coated with the four donor molecules, **D1-D4**.

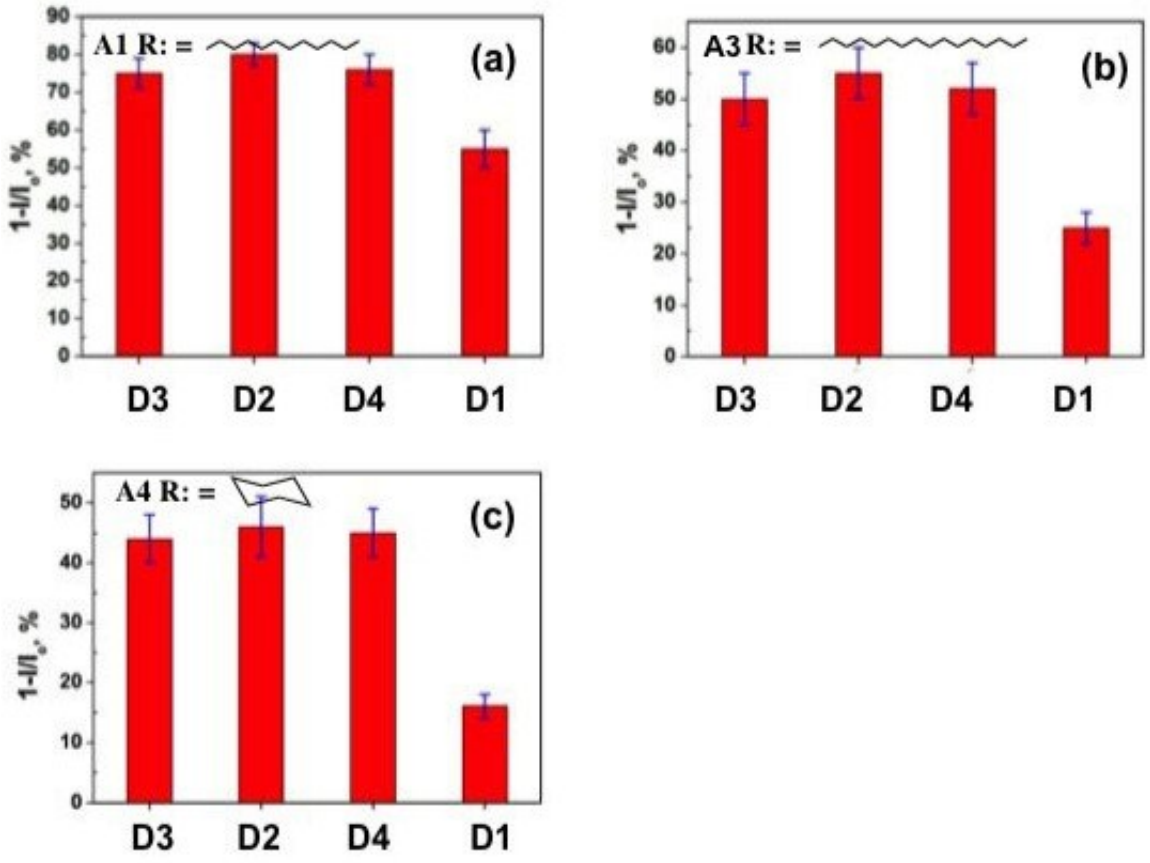

Figure 2.24. Comparison fluorescence quenching between the various functionalized PDI nanofibers coated with the four donor molecules, **D1-D4**.

As shown in Figure 2.24, all four TBP molecules when coated on the surface of A1 nanofibers showed efficient quenching of the fluorescence of the nanofibers. The extent of fluorescence quenching on **A2** and **A4** nanofibers is noticeably lower. **A2** has a shorter alkyl chain while **A4** has bulky side chains (cyclohexyl). The mismatch between the side chains in the acceptor molecule and those in the donor molecules clearly affected the charge transfer between the D and A species. The photocurrent responses, shown in Figure 2.23, are more striking for the different acceptor molecule-based heterojunctions. **A2** and **A3**, both have linear alkyl chains but one is four carbon shorter while the other is four carbon longer than the dodecyl chain in the TBP molecule, showed photocurrent responses one order of magnitude lower than those based on the A1 molecule. Heterjunctions based on A4/TBP showed similarly low photocurrent. **A5**, which possesses ether side chains, showed the lowest photocurrent. The incompatible side chains prevent the close and tight locking of the D/A molecules, resulting in the significantly lower photocurrents.

2.4 Photovoltaic Properties of TBP/ PCBM and TBP/PDI

To evaluate the photovoltaic properties of the new alkoxyl substituted TBPs, bulk heterojunction solar cells using **D3** as the electron donor and **A1** or [6,6]-phenyl-C_{61} butyric acid methyl ester (PCBM) as the electron acceptor were fabricated with a device structure of ITO/PEDOT:PSS/**D3**:PDI (or PCBM)/Ca/Al. Figures 2.25(a) and 2.25(b) show the absorption spectra of the mixtures of **D3**:**A1** and **D3**:PCBM (1:1, wt. ratio) in chloroform and film, respectively. The spectra of the mixtures in solution are a simple linear superimposition of the individual components. As for the blend film of **D3**:**A1**, a significantly broadened absorption with a long tail extending to 800 nm was observed as compared to its absorption spectrum in solution. This indicates a strong aggregation in the **D3**:**A1** film. Both homostacking of **D3** and/or **A1**, and heterostacking between **D3** and **A1** (donor-acceptor stacking) may occur and contribute to the spectral broadening and bathochromic shift. On the other hand, the film spectrum of **D3**:$PC_{61}BM$ showed broadened peaks only at wavelengths below 450 nm which corresponds to the **D3** homo-π-π stacking.

Figure 2.26 shows the current density–voltage (*J*–*V*) characteristics of the solar cells. The blend film of **D3**:**A1** exhibited an efficiency of 0.12% with a V_{OC} of 0.78 V, a J_{SC} of 0.75 mA/cm^2, and a FF of 0.21. This efficiency is comparable to those of previously reported photovoltaic devices of hexabenzocoronene:PDI blends.[107] However, the blend film of **D3**:$PC_{61}BM$ showed a poor efficiency of only $6.8*10^{-4}$ % with a V_{OC} of 0.87 V, a J_{SC} of 0.0029 mA/cm^2, and a FF of 0.27. This is likely due to the dramatically different molecular shapes of **D3** and $PC_{61}BM$ which prevents an intimate blending of the two components/domains. Further optimization of the solar cells is under investigation.

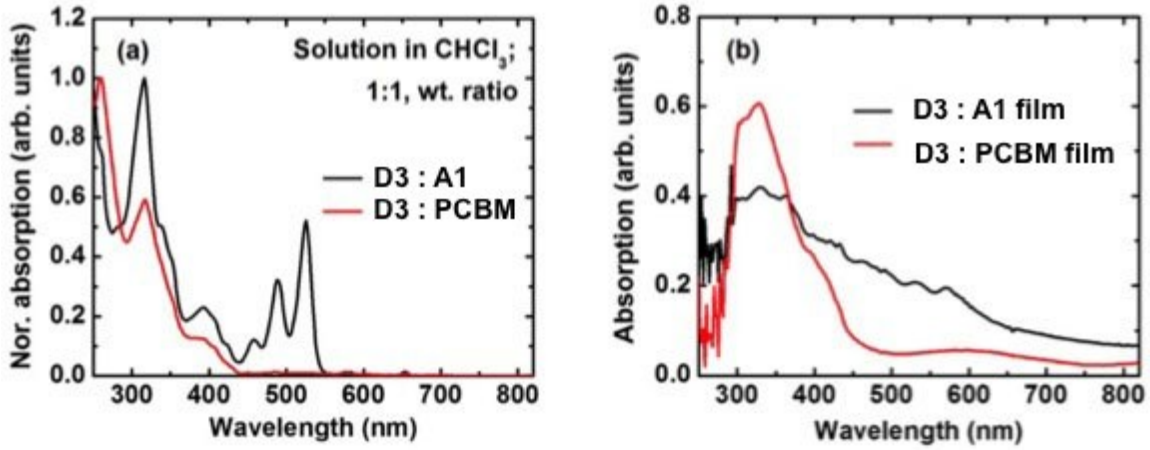

Figure 2.25. UV/Vis absorption spectra of **D3**:**A1** and **D3**:PCBM (1:1, wt. ratio) in chloroform (a) and as annealed films (b).

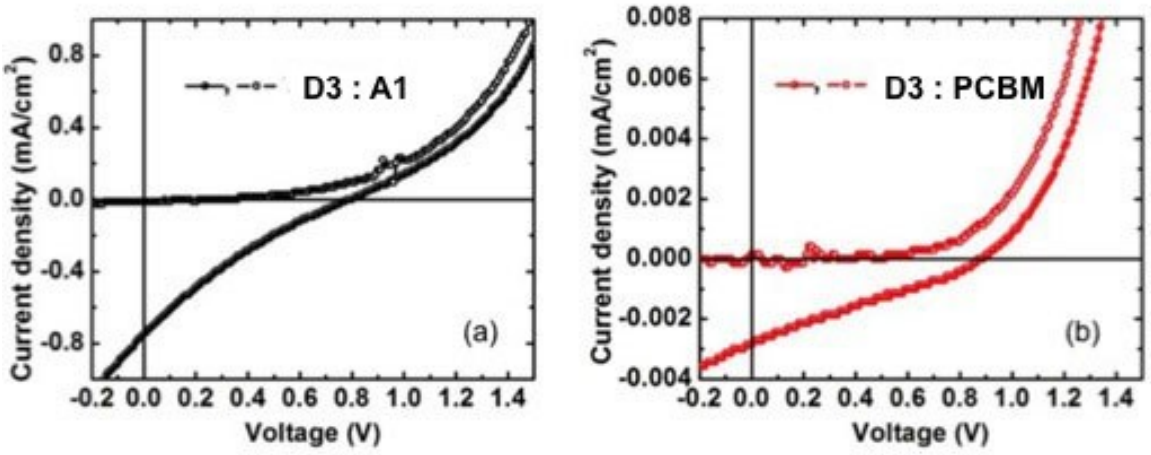

Figure 2.26. *J–V* curves of the solar cells fabricated from **D3:A1** (a) and **D3:**PCBM (b) in dark and under illumination.

2.5 Conclusions

We have investigated a series of TBP molecules with the same π-conjugation core but different side groups as electron donors (**D1-D4**). Various PDI nanofibers (electron acceptors) coated with such donor molecules showed dramatically different photocurrent responses. It has been observed that the PTCDI nanofibers with dodecyl side chains had the best photocurrent response when it was coated with all TBP molecules. The strong hydrophobic interdigitation between the long dodecyl side chains of **D1-D4** and **A1** molecules enable efficient charge transfer between the two under photoexcitation. Any side chain mismatching, whether by length, bulkiness or electronic property leads to lower photocurrent responses. It was also found that the nanofibers coated with homogeneously and molecularly distributed donor molecules (such as **D4)** exhibit the highest photocurrent, whereas those coated with segregated donor aggregates (such as **D1-D3)** show much lower photocurrent under the same illumination conditions. The aggregation of donor molecules on the surface of the PTCDI fibers may lead to the buildup of local electrical field which hinders the charge separation of the photogenerated electron-hole pairs. The different morphologies of molecular aggregates were mostly the result of side group modification of the donor molecules. Such structural effect was more clearly manifested by investigating the structure and morphology change of the drop-cast films upon solvent vapor annealing. The findings presented provide new insight into the molecular structural effect on photoconductivity of organic semiconductor materials, particularly those based on donor-acceptor composites or interfaces, and open alternative ways to improve the photoconductivity by structural design and modification. Finally, preliminary studies for photovoltaic cells using **D3** as electron donor and **A1** or PCBM as

electron acceptor have been fabricated. The **D3**:PDI blend exhibited better PV performance and a power conversion efficiency of 0.12% has been obtained.

2.6 Experimental Section

General.

All the reactions were carried out under Nitrogen protection in flame-dried glassware. The solvents were used after fresh distillation over drying agents indicated and were transferred under nitrogen: THF (Na/benzophenone), CH_2Cl_2 (CaH_2). $PC_{61}BM$ was purchase from Nano-C, Inc. PDI was synthesized following published procedures.[47]

Instrumentation.

UV-vis absorption spectra were measured on a PerkinElmer Lambda 25 spectrophotometer. The fluorescence spectra were taken on a PerkinElmer LS 55 spectrophotometer. Bright field and fluorescence optical microscopy images were obtained with Leica DMI4000B inverted microscope equipped with Acton SP-2356 Imaging Spectrograph system and Princeton Instrument Acton PIXIS:400B Digital CCD Camera System for high resolution full spectral recording. AFM measurement was performed in tapping mode on a Veeco MultiMode V scanning probe microscope, for which samples were directly drop-cast on a silicon wafer covered with 300-nm thick SiO_2 layer. The electrical conductivity was measured using a two-probe method on a Signatone S-1160 Probe Station combined with an Agilient 4156C Precision Semiconductor Analyzer. A tungsten lamp was used as the light source with a light intensity of 0.17 mW/mm^2 on the testbed. The gold-electrode pair used was 14 μm in width and 5 μm in gap.

Solvent Vapor Annealing Process.

Solvent vapor annealing was performed by putting the nanofiber sample (deposited on a substrate) into a sealed 50 mL jar, which contained 5 mL of ethanol at bottom to maintain the saturated vapor of ethanol. The annealing was kept for 3 h.

Preparation of Surface Modified Glass slides.

The glass slides were first thoroughly cleaned in acetone and isopropanol for 3 min each in an ultrasonic bath, and then cleaned with a piranha solution (70 vol% H_2SO_4: 30 vol% 30% H_2O_2) for 20 min, followed by rinsing with deionized water and drying in air flow. To form monolayer of octadecyl-trichlorosilane (OTS) on the surface, the glass slides were immersed in an anhydrous toluene solution of OTS (3 mM) for 3 h, followed by ultrasonic cleaning in fresh toluene solvent for 2 min to remove the excessive OTS residues. The glass slides were then baked on a 150 ºC hot plate for 1 h to enhance the surface crosslinking.

Photovoltaic devices fabrication and characterization.

The model solar cell was shown in the Figure 2.27. Indium tin oxide (ITO) coated glass slides with sheet resistance of 8–12 Ω/square was used as substrates. ITO glass was cut into 1.5 cm by 1.5 cm pieces, and the ITO was patterned by etching with aqua regia vapor. The patterned ITO glass substrates were cleaned in an ultrasonic bath sequentially by detergent, water, deionized water, toluene, acetone, and isopropyl alcohol, each for 15 min, and then dried by compressed air stream. Cleaned ITO substrates were treated with UV ozone for 45 min before use. Highly conductive poly(3,4-ethylenedioxythiophene):poly(styrenesulfonate) (PEDOT:PSS, Clevios P VP AI4083) thin layer was spin-coated (4,000 RPM, 30 s) onto the ITO substrates from an aqueous

solution. The substrates were dried at 120 ºC for 45 min on hotplate in air. Blend solutions of **1b**:PDI (1:1 wt. ratio; 10 mg/mL) and **1b**:PCBM (1:1 wt. ratio; 10 mg/mL) were prepared in glove box by dissolving respective materials in $CHCl_3$. The solutions were heated at 50 ºC with stirring for 48 h and passed through a 0.45 μm filter before spin coating. The active layer was deposited by spin-coating the solution of respective active materials on top of the PEDOT:PSS layer. The devices were transferred to glove box and dried in nitrogen atmosphere under reduced pressure. The films were annealed at 80 ºC for 20 h in nitrogen atmosphere. Subsequently, an electrode including 45 nm thick Ca and 100 nm thick Al was deposited on the top by thermal evaporation under high vacuum ($<2\times10^{-6}$ MB). The active area of 0.14 cm^2 of the devices was defined by the area of deposited Ca/Al electrode through a shadow mask.

Current–voltage characteristics were measured using a Keithley 2400 Source Meter. Devices were illuminated with an Oriel Xenon Arc Lamp Solar Simulator at an intensity of 100 $mW{\cdot}cm^{-2}$ (1-sun air mass 1.5 global illumination). Short circuit current density (J_{SC}), open circuit voltage (V_{OC}), and maximum output power density ($J_{max}V_{max}$) were obtained from the *J–V* curves under illumination. The power conversion efficiency was calculated by $\eta = J_{SC}V_{OC}FF/P_{in}$, where P_{in} is the incident power density; and FF is fill factor which is given by $J_{max}V_{max}/J_{SC}V_{OC}$.

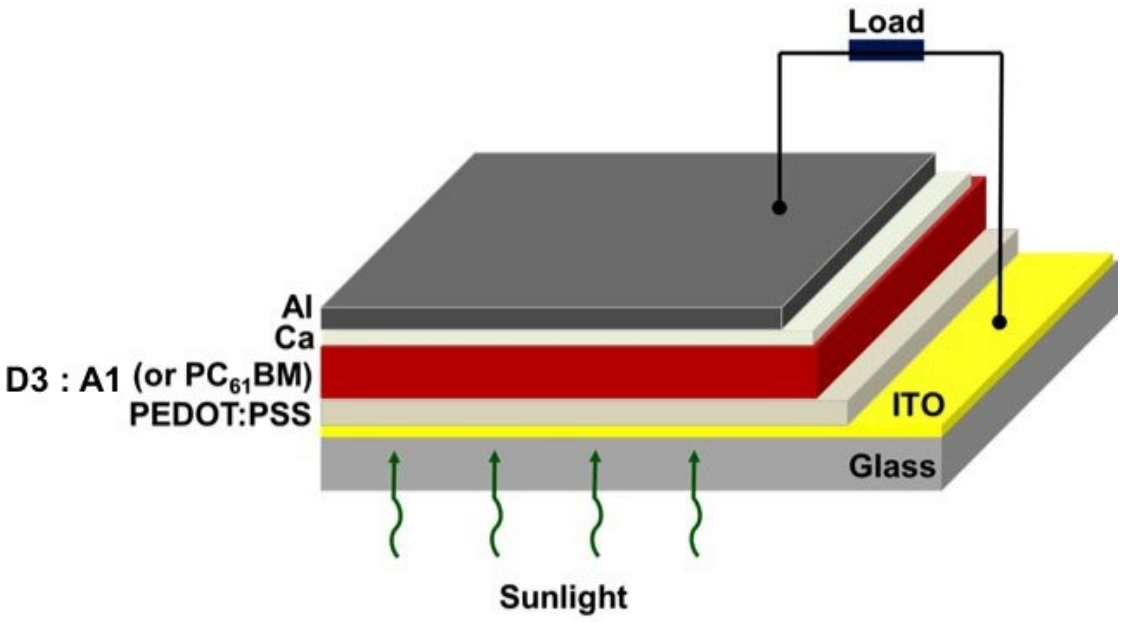

Figure 2.27. The solar cell device configuration of **D3** blended with **A1** or PCBM.

CHAPTER 3

SYNTHESIS, SELF-ASSEMBLY, AND APPLICATIONS OF A DIPHENYL-SUBSTITUTED TRIBENZOPENTAPHENE

3.1 Introduction

Hexa-peri-hexabenzocoronene (HBC) is an important polycyclic aromatic hydrocarbon (PAH), which is built of all-benzenoid. HBC exhibits a highly symmetrical structure and acts as the core fragment of discotic liquid crystals.[43,53,55,108] Unlike other large PAHs, many HBC derivatives have been synthesized and successfully demonstrated in a number of potential applications such as field effect transistors, photovoltaic cells, etc.[19,20,109] Fundamental studies on HBC derivatives are also abundant which include the order and dynamics of molecules in the columnar phase, the relationship between charge carrier mobility and molecular morphology, macroscopic alignment in solution or melt, self-assembly of molecules on film, etc. Furthermore, because the HBC core is composed of carbon atoms only, they can act as precursors for functional carbon nanomaterials.[110-115] Over the past couple of decades systematic experimental and theoretical studies correlating the charge carrier mobility of HBCs with mesophase structures, especially in the columnar phase have been carried out, which has led to the basic understanding and molecular design principles for improving their electrical and optical performance in electro-optic devices.[116-118]

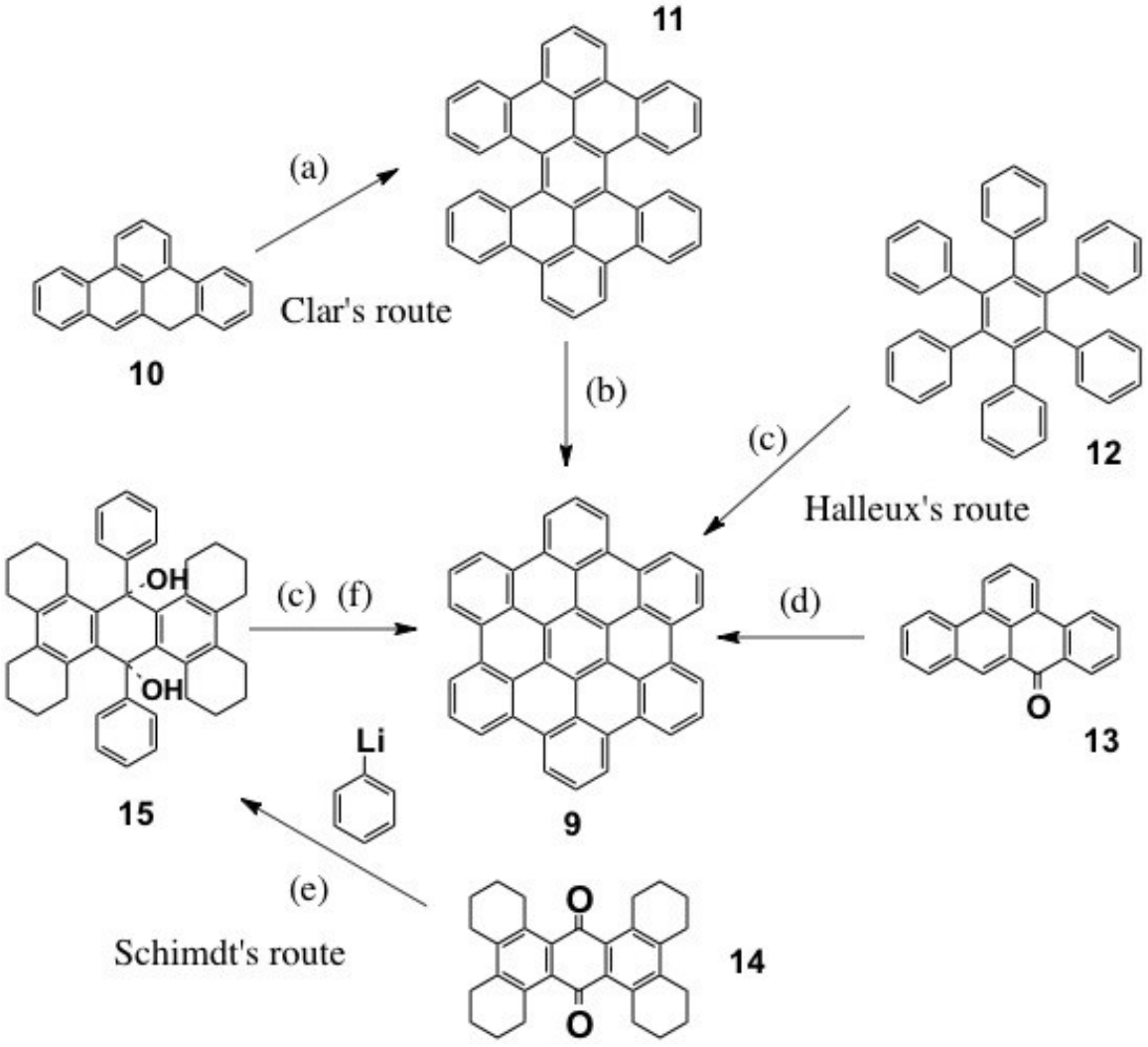

Scheme 3.1. Different synthesis routes of HBC hydrocarbon: (a) Br_2, C_6H_6 at 153 ^oC; (b) at 481 ^oC; (c) $AlCl_3$/NaCl at 120 ^oC; (d) $Zn/ZnCl_2$ at 330 ^oC; (e) Et_2O/C_6H_6; (f) Cu, 400 ^oC.

HBC core contains 42 carbon atoms and 13 benzene rings and can be used as a nano graphene. HBC has a D_{6h}-symmetry, and its conjugated π system is three times larger than triphenylene and two times larger than tribenzopentaphene discussed in the previous two chapters. HBC is considered as a "supper benzene" and exhibits appealing electrical properties.

The HBC hydrocarbon was first discovered in the late 1950s.[119-121] In 1958, Clar, the pioneer of polycyclic aromatic hydrocarbons, was the first person to successfully synthesize the parent hydrocarbon **9** (Scheme 3.1).[119-120] In the same year, Halleux and coworkers developed different routes to synthesize HBC.[123] Scheme 3.1 shows three different synthetic routes to HBC. The direct cyclodehydrogenation of hexaphenylbenzene (Compound **12**) with $AlCl_3$/NaCl at 120 ^oC, or compound **13** with $Zn/ZnCl_2$ at 330 ^oC lead to identical HBC molecule. Later, Schmidt and coworker reported alternative synthesis methods to make the parent HBC (Scheme 3.1).[124] All these synthetic methods give very low yields and requires complicated purification process. In the late 1990s, Mullen reported that HBC derivatives could be made in good yields by intramolecular oxidative cyclodehydrogenation of hexaphenylbenzene using a Cu(II) salt such as $CuCl_2$ or $Cu(OTf)_2$ as the oxidant combined with a Lewis acid $AlCl_3$.[43,53,55,108] $FeCl_3$ was soon found to be a better cyclodehydrogenation agent as it can act as both a fairly strong Lewis acid and a mild oxidizing agent. Scheme 3.2 shows a well adopted synthetic protocol to HBC derivatives, especially alkyl-substituted HBCs.[124] The two key steps are the alkyne trimerization of **20** to give hexa(4-alkylphenyl)benzene **21** and its subsequent oxidative cyclodehydrogenation (intra-molecular Scholl reaction). This approach has been applied to prepare a number of alkyl-substituted HBCs and some of

them have been shown to exhibit strong self-association and very high charge carrier mobilities.[127-128]

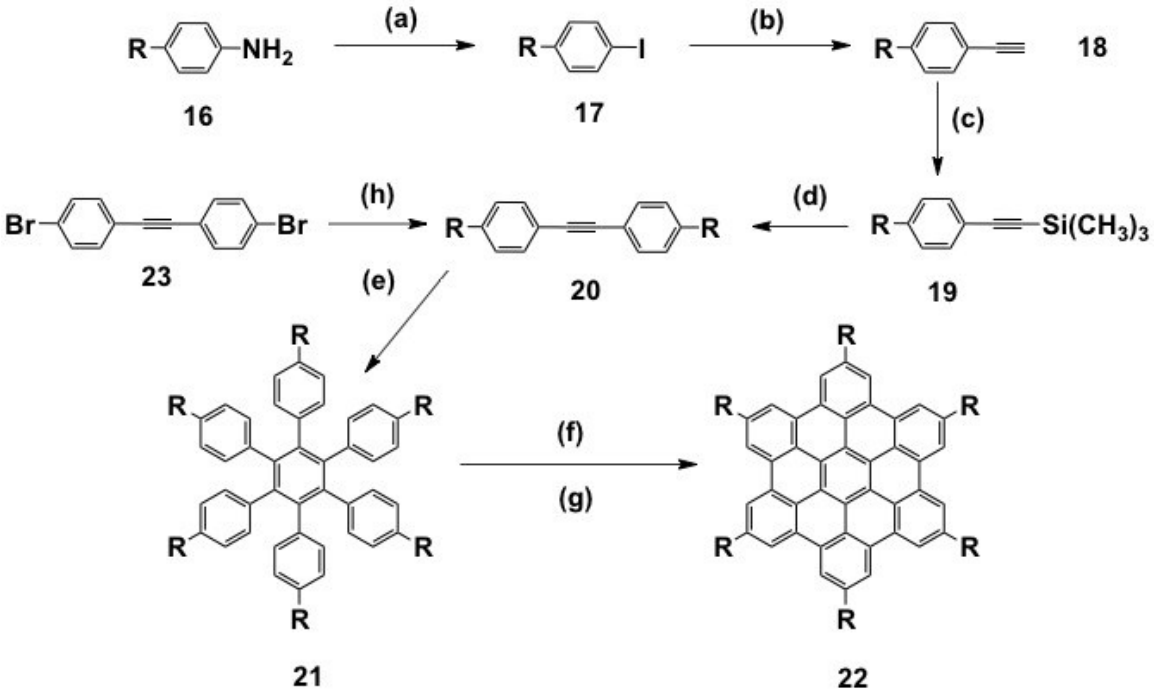

Scheme 3.2. New synthesis protocol for HBC derivatives: (a) $C_5H_{11}NO_2$, KI; (b) TMSA, $[PPh_3]PdCl_2$, PPh_3, CuI, piperidine; (c) KF, DMF; (d) **9**, $[PPh_3]PdCl_2$, CuI, piperidine; (e)$Co_2(CO)_8$; (f) $AlCl_3$, $Cu(CF_3SO_3)_2$, CS_2; (g) $FeCl_3/CH_3NO_2$, CH_2Cl_2; (h) $[PdCl_2(ddpf)]$, THF, RMgBr.

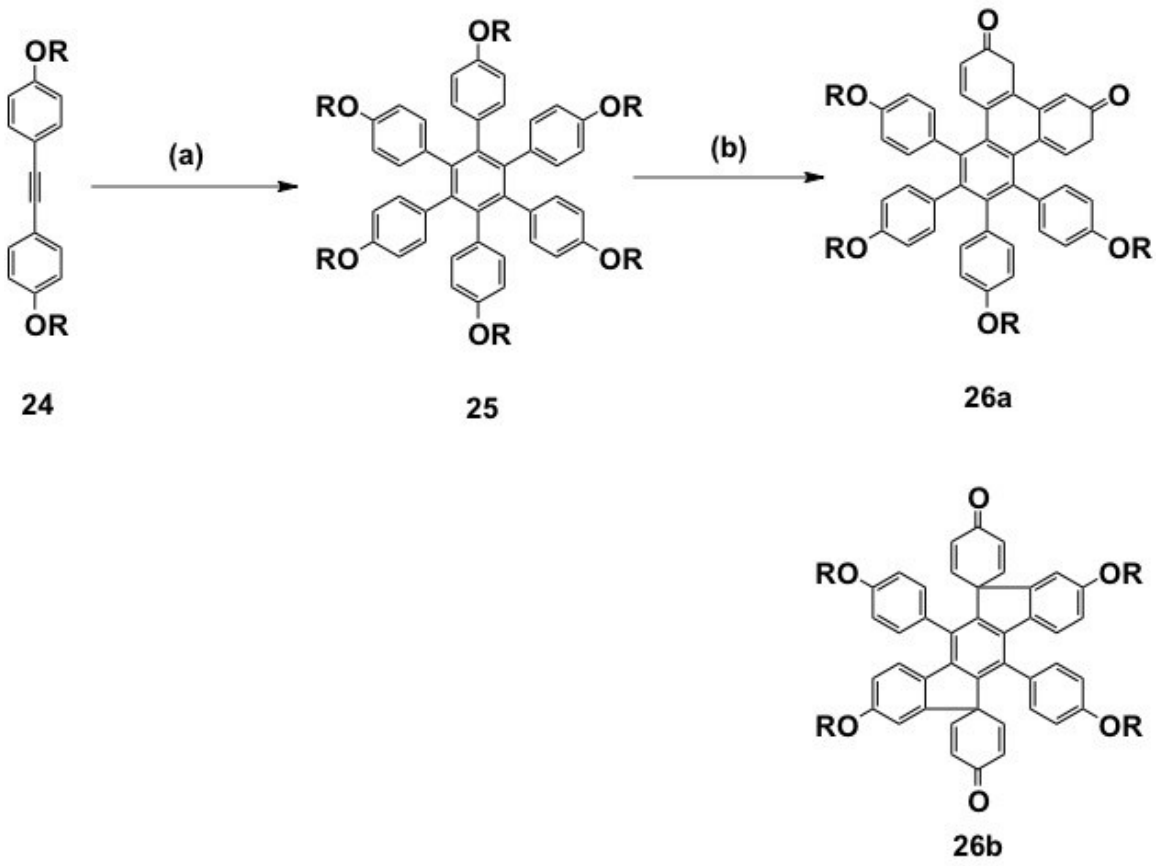

Scheme 3.3. Synthesis protocol of hexaalkoxy-HBCs: (a) [$Co_2(CO)_8$], dioxane; (b) $FeCl_3$, $MeNO_2$, CH_2Cl_2.

While the Scholl reaction works well on alkyl-substituted hexaphenylbenzene (compound **21**), it fails to give the alkoxy-substituted HBC analogy. The reaction is instead complicated by a number of side products that the alkoxy-substituted hexaphenylbenzene **25** compound may lead to quinone products **26**[125-126] and various chlorinated derivateves[126] during the oxidative cyclodehydrogenation (Scheme 3.3). An alternative route to the alkoxy-substituted HBC analog (hexaalkoxy-substituted HBC **32)** has recently been reported (Scheme 3.4).[129]

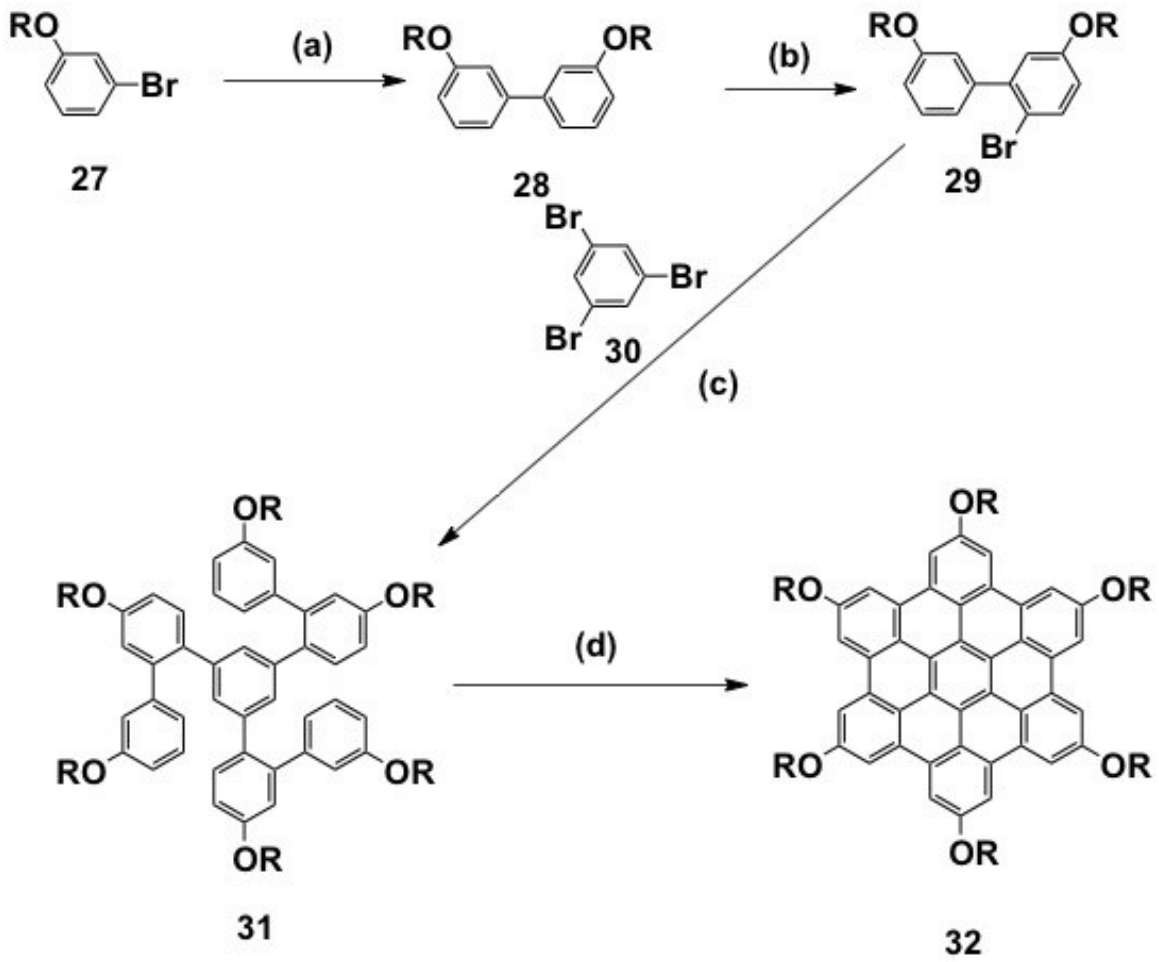

Scheme 3.4. New Synthesis route of hexaalkoxy-HBC derivatives: (a) THF, -78ºC, BuLi, $B(OMe)_3$; (b) Toluene/EtOH/ $H_2O/Na_2CO_3/Pd(PPh_3)_4$; (c) NBS, MeCN; (d) $FeCl_3$, CH_3NO_2, CH_2Cl_2.

The synthetic routes discussed so far lead to highly symmetrical HBCs with only one type of functional group. Scheme 3.5 shows a general approach to HBCs with unsymmetrical substitution patterns.[130-131] The precursor of unsymmetrically functionalized hexaphenylbenzenes **37** can be prepared by a [4+2] Diels-Alder cycloaddition with a suitably substituted diphenyl acetylene **36** and 2,3,4,5-tetraacrylcyclopenta-2,4-dien-1-one **35**. The key compound of cyclopentadienone in this route can be synthesized via double Knovenagel condensation between a 4,4'-substituted benzyl **33** and 1,3-diarylacetone **34**. The last step again relies on the Scholl-type oxidative cyclodehydrogenation reaction.

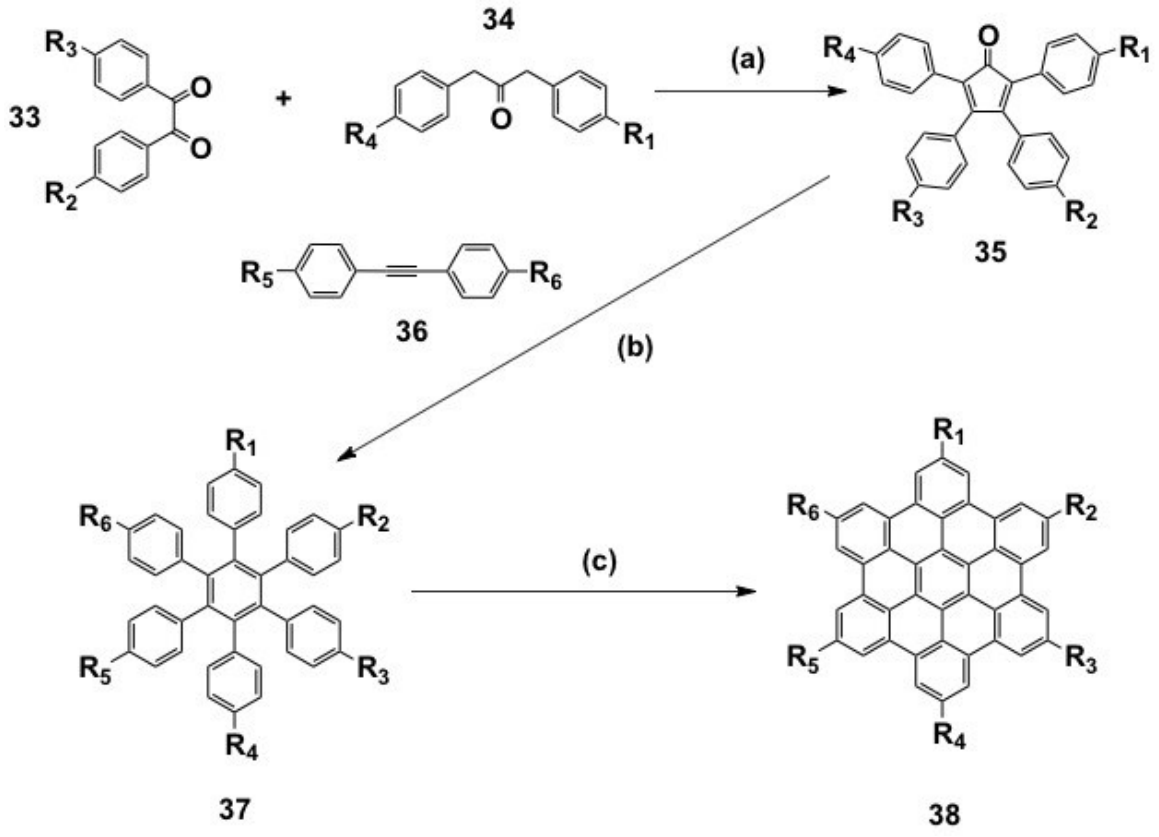

Scheme 3.5. The protocol of unsymmetrically substituted HBC derivatives: (a) Bu_4NOH, MeOH, t-BuOH or KOH. EtOH, reflux; (b) Ph_2O, 260 ^oC; (c) $FeCl_3$, $CH_2Cl_2/MeNO_2$.

This approach has been used to prepare a number of interesting unsymmetrically-substituted HBCs including HBCs containing covalently linked electron deficient anthraquinones (Figure 3.1).[132-133] These donor-acceptor systems show nanophase separation and form so called “molecular double cables”.

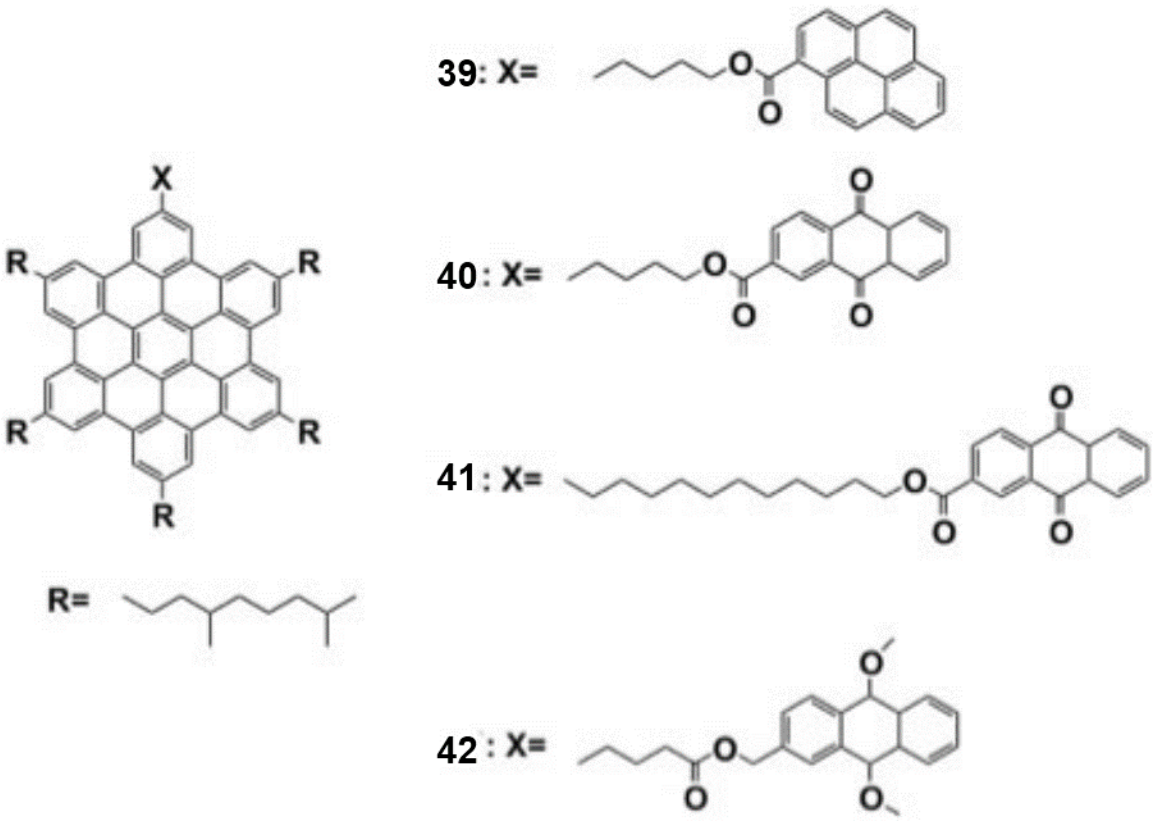

Figure 3.1. The structure of covalently linked donor and acceptor HBC derivatives.

3.2 Objectives

Encouraged by the appealing properties of tribenzopentaphene (TBP) derivatives discussed in the previous two chapters, we set our next goal on substituted HBCs. Our target is shown as compound **48** in Scheme 3.6. This compound is designed for the following two considerations. First, alkoxy substitution is known to direct cyclodehydrogenation at its para and ortho positions. Having alkoxy group at the meta position in compound **46** is expected to facilitate and direct the formation of the desired product. Second, our long term goal is to prepare conjugated foldamers using HBC as the backbone building blocks. If compound **48** is successfully prepared, halogenation of **48** is expected to introduce halogens (iodo or bromo) to the two positions ortho to the alkoxy groups. The resulting bi-functional monomers can be used to prepare our targeted foldamers.

3.3 Synthesis of Hexa-peri-hexabenzocoronene (HBC)

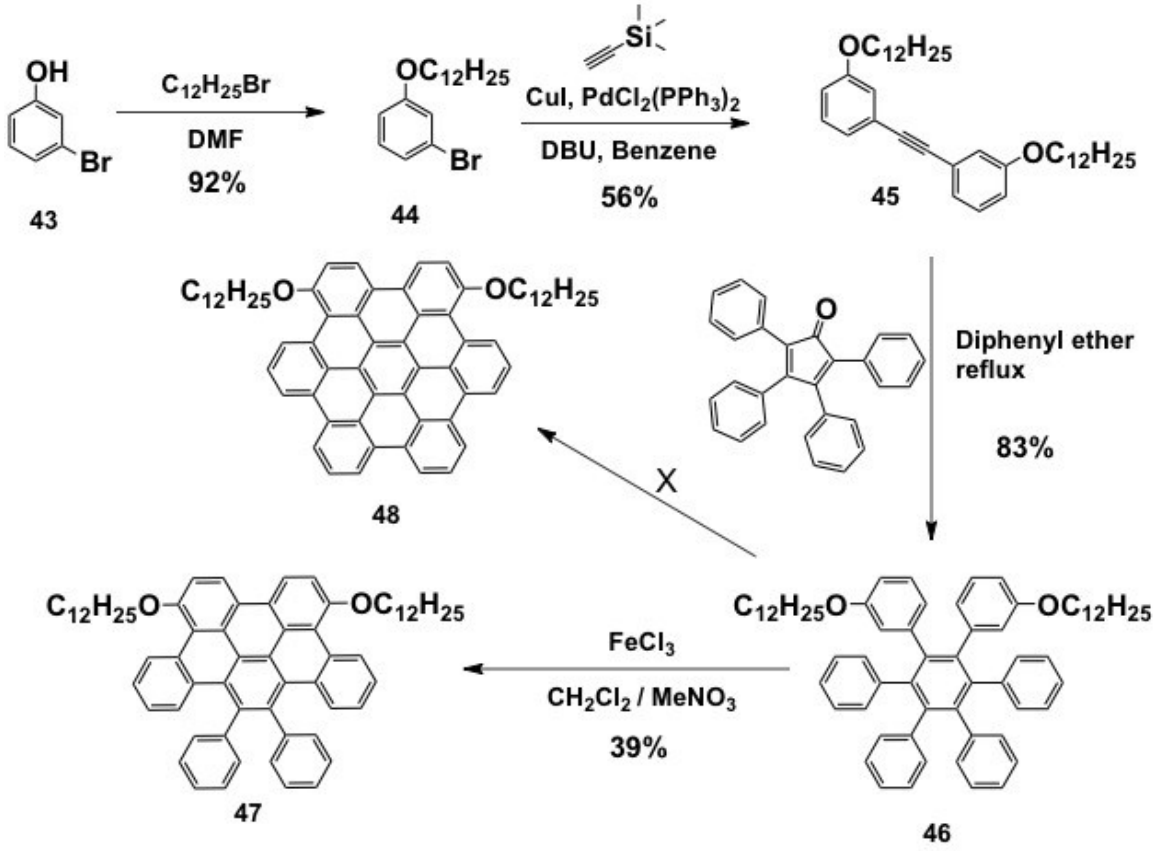

Scheme 3.6. Synthesis route of hexabenzocoronene.

Scheme 3.6 shows the planned synthetic route to compound **48**. The synthesis started with commercially available 3-bromophenol (**43**). After alkylation, 1-bromo-3-(dodecyloxy)benzene was obtained, which was then subjected to one pot symmetrical Sonagoshia coupling reaction, giving 1,2-bis(3-(dodecyloxy)phenyl)ethyne (**45**) in excellent yields.[134] Compound **45** was then reacted with commercially available 2,3,4,5-tetraacrylcyclopenta-2,4-dien-1-one by [4+2] Diels-Alder cycloaddition leading to the successful synthesis of the precursor compound **46**.[135] Attempts on the

cyclodedydrogenation of compound **46** using various Scholl reaction conditions, unfortunately, failed to produce the desired product HBC **48** (Table 3.1). Instead, phenyl substituted TBP derivative (compound **47**) was obtained. The structure of **47** has been confirmed by NMR (Figure 3.2) and MALDI-TOF (Figure 3.5) measurements.

Table 3.1. Various reaction condition of HBC synthesis

						Yields %	
Entry	Oxidants	Equiv.	Solvents	Time	Temperature	**47**	**48**
1	$FeCl_3$	9	$CH_2Cl_2/MeNO_2$	2hr	RT	25	0
2	$FeCl_3$	32	$CH_2Cl_2/MeNO_2$	12hr	RT	39	0
3	$FeCl_3$	50	$CH_2Cl_2/MeNO_2$	24hr	Reflux	17	0
4	$MoCl_5$	50	CH_2Cl_2	12hr	RT	32	0
5	$MoCl_5$	50	CH_2Cl_2	24hr	Reflux	13	0
6	DDQ	3	$CH_2Cl_2/MeSO_3H$	24hr	0 ^oC	0	0

3.4 Structural Characterization

Compound **47** is soluble in common organic solvents such as chloroform, benzene, and THF. Its structure and purity have been confirmed by ^{1}H & ^{13}C NMR, MALDI-TOF MS measurements and elemental analysis. Figure 3.2 shows ^{1}H NMR spectra of compound **46** and **47**, where sharp and well resolved signals are observed. The ^{13}C NMR of compound **47** was also shown in Figure 3.3 After cyclization, the $-OCH_2-$ protons shift downfield with the chemical shift increasing from 3.5 ppm to around 4.5 ppm. The significantly increased deshielding on these alkoxy methylene protons indicates that the aromatic system on which the alkoxy groups bind to becomes stronger after cyclization. In other words, the alkoxy-binding phenyl rings must become part of a stronger aromatic system, which excludes compound **49** showing in Figure 3.6 as the possible product. The aromatic region of the product shows 7 signals: four doublets, one triplet and two multiplets (Figure 3.4). The proton integration in aromatic region is 18 which is matched proton numbers of compound **47**. Furthermore, compound **47** has been subjected to MALDI-TOF MS analysis. As shown in Figure 3.5, the spectrum shows three major peaks at mass/charge ratios of 558.1, 727.3, and 897.5, which can be assigned to the molecular ion M^+, $(M-R)^+$ and $(M-2R)^+$, respectively. Concluded the above data, the compound **48** which is fully cyclized HBC can be excluded.

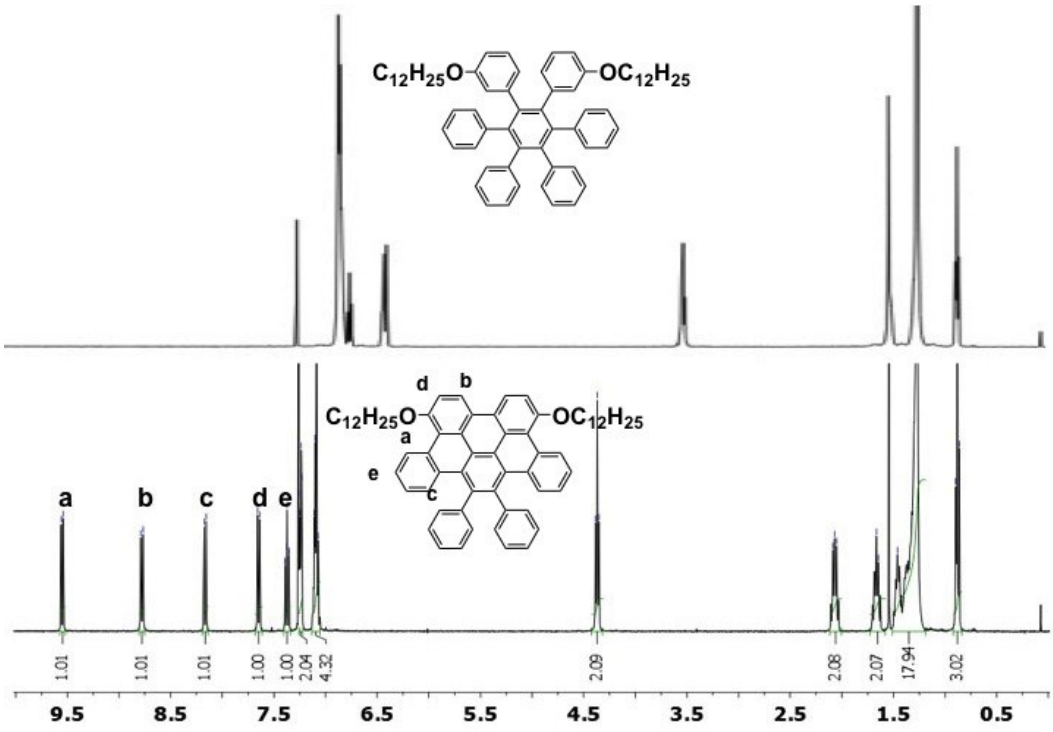

Figure 3.2. [1]H NMR of precursor (**46**) and half-cyclized HBC (**47**).

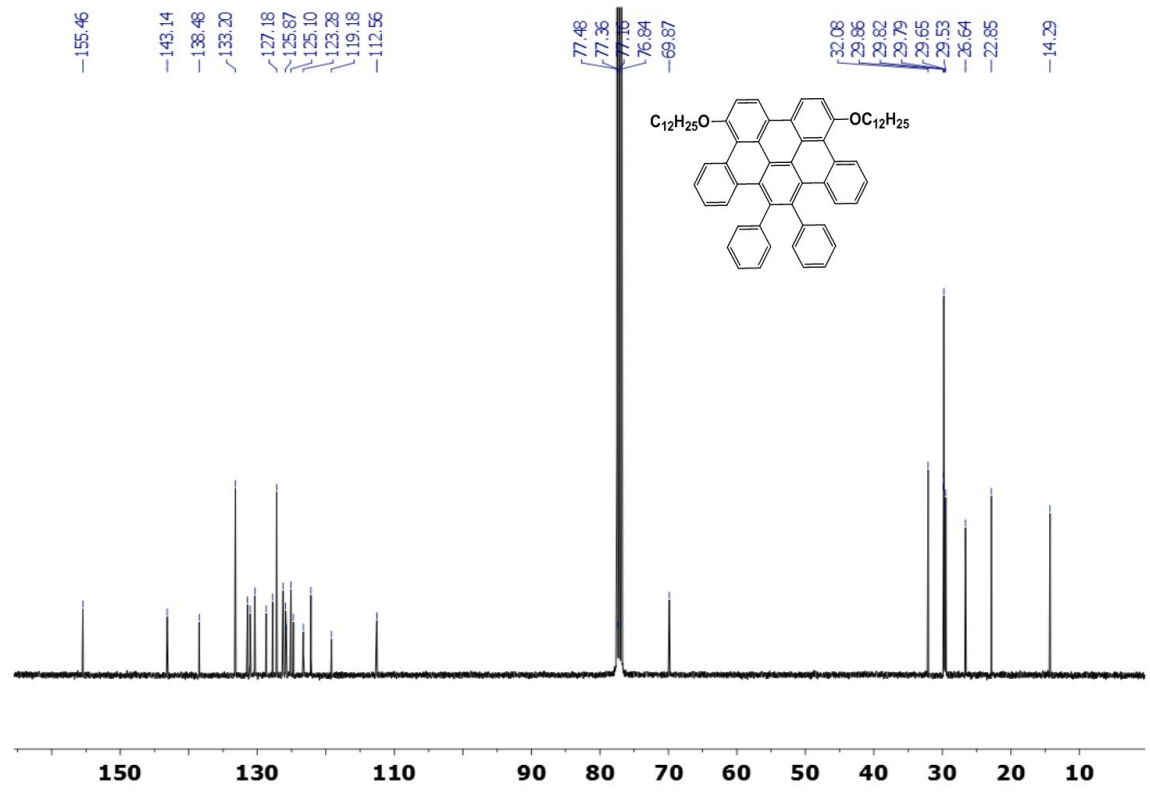

Figure 3.3. [13]C NMR of compound **47.**

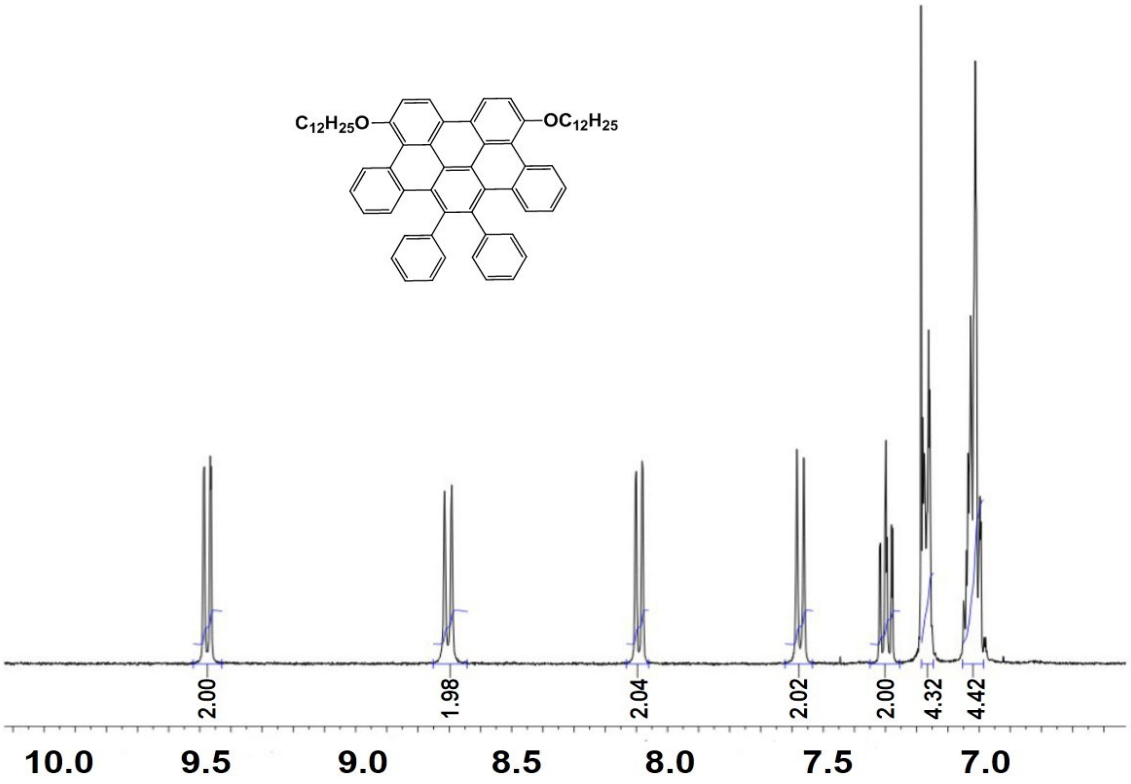

Figure 3.4. ^{1}H NMR of half cyclized HBC (**47**) in aromatic region.

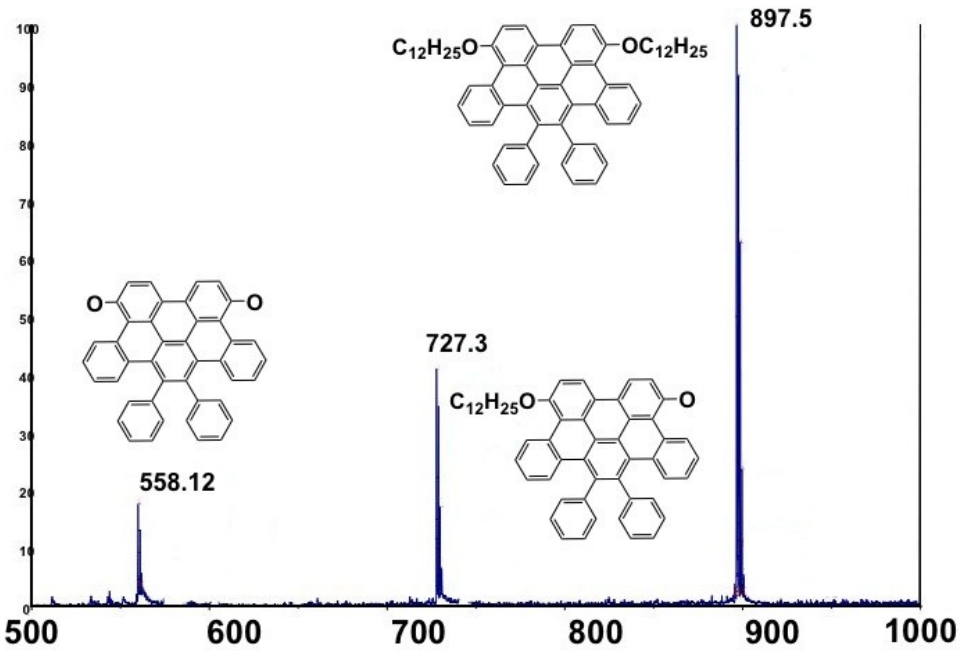

Figure 3.5. MALDI-TOF of half cyclized HBC (**47**).

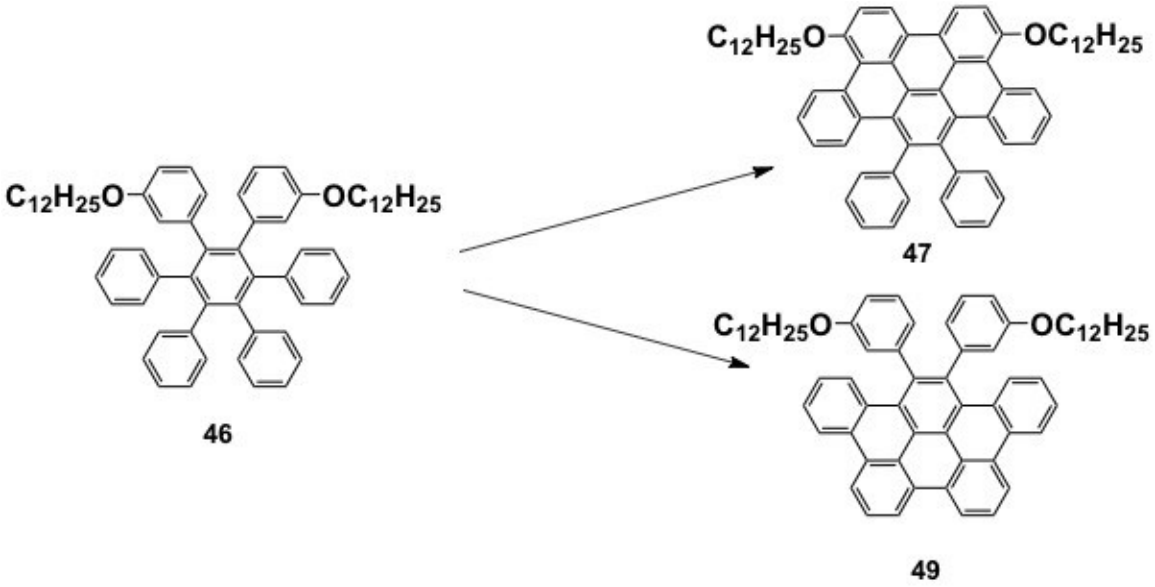

Figure 3.6. Two possible isomers of half cyclized HBC molecules.

3.5 Optical Properties of a Diphenyl-Substituted Tribenzopentaphenes

While we are disappointed that the targeted HBC was not realized, compound **47** itself is an interesting PAH. The two phenyl substituents at the bay positions are likely significantly twisted and thus can block the TBP core π–π stacking at least from the bay side. The two dodecyloxy chains are *para* to each other and it will be interesting to see whether they can intedigitate cooperatively with dodecyl-substituted PTCDI acceptors discussed in Chapter two.

Absorption spectra: The steady state optical properties of **47** were studied in both dilute solutions and as solid films. Figure 3.7 shows the UV-Vis absorption spectra of a dilute chloroform solution and a thin solid film of **47**. Compared with the absorption spectra of **1a**, **47** showed much stronger absorption in the visible range. In particular, the α band is significantly enhanced and bathochromically shifted. The stronger S_0-S_1 absorption (π–π* transition) is likely due to the effect of the two phenyl rings in the bay position whose partial conjugation with the TBP core lowers the symmetrical of the TBP π system. Unlike compound **1a** whose film spectra show clear red-shift (more than 25 nm) on all absorption bands, the film spectrum of **47** shows only very slight redshift (less than 10 nm) over its solution spectrum, presumably due to the steric effect of the two phenyl rings which blocks at least partially the π-stacking of TBP rings.

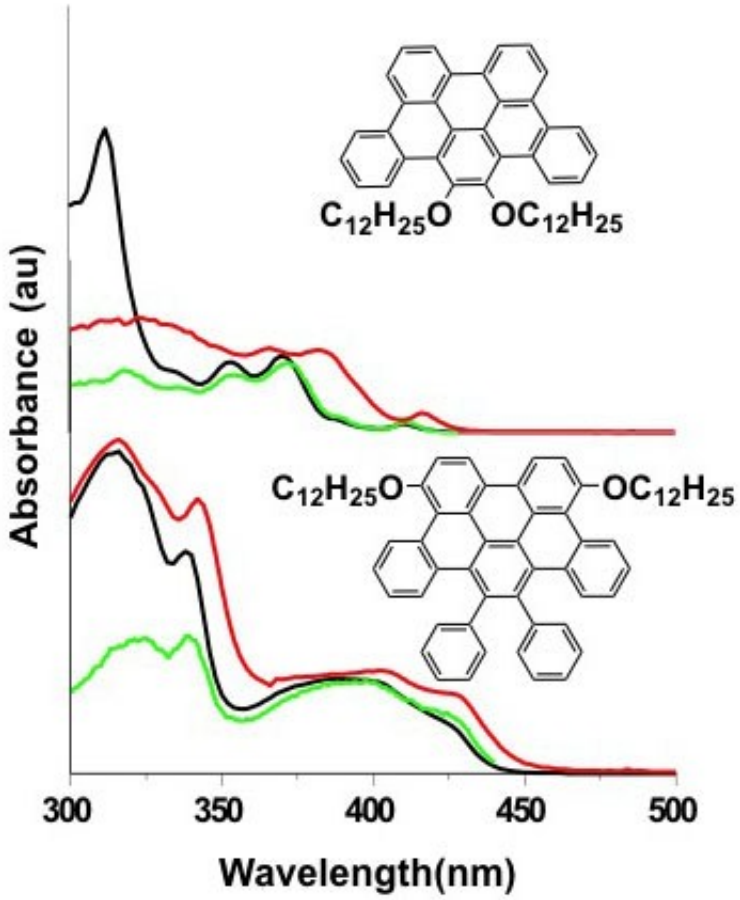

Figure 3.7. UV-Vis absorption (black) and excitation (green) spectra of the **1a** and **47** compounds in chloroform solutions. The red curves are the absorption spectra of the **1a** and **47** films.

Table 3.2. Fluorescence quantum yields of **1a** and **47** of tribenzopentaphene derivatives measured in dilute chloroform solution.

Compound	**1a**	**47**
λ_{ex} (nm)	370	427
Φ_{fl}	0.156	0.334

Fluorescence spectra: The solution fluorescence quantum yield of **47** and **1a** are listed in Table 3.2 and the florescence emission spectra are shown in Figure 3.8. In a dilute solution, **47** shows a maximum emission wavelength λ_{max} of 450 nm, while the emission λ_{max} of **1a** is 418 nm. The fluorescence quantum yields of **1a**, and **47** in chloroform are 0.16 and 0.33, respectively (Table 3.2). The higher fluorescence quantum yield of **47** is again due to the lower symmetry of its π system. While the film of **1a** gives a red-shifted, broad, and featureless emission band, the emission of film **47** showed a red-shifted emission, but with clear vibronic features (Figure 3.8). The observation of this significantly red-shifted (around 50 nm) emission with clear vibronic features indicates that the two phenyl rings and the TBP core of **47** adopts much smaller dihedral angles in the solid film than those in solution. It is also plausible that the TBP core in **47** may still π–π stack by alternating the phenyl substituents on opposite side of adjacent **47** molecules. The excitation spectrum of **47** in solution closely matches its absorption spectrum, especially in the spectral range of 350-450 nm (Figure 3.7).

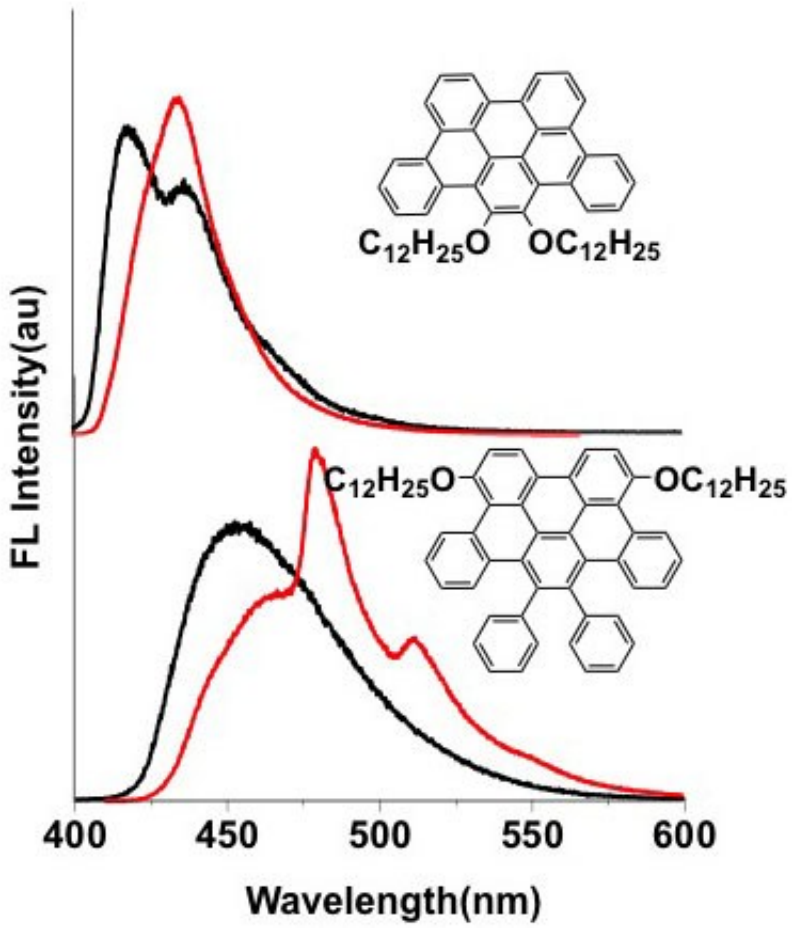

Figure 3.8. Fluorescence emission spectra of compounds **1a**, and **47** in chloroform solutions (black) and as solid films (red).

3.6 Electrochemical Properties of a Diphenyl-substituted Tribenzopentaphene Derivative

Cyclovoltammogram of **47** in methylene chloride solution is shown in Figure 3.9. Compound **47** shows a reversible oxidation wave with a half-cell potential of 0.49V, respectively. Under identical conditions, a reversible oxidation wave ($E_{1/2}$ = 0.15 V) is observed for the ferrocene/ferrocenium couple. Using the ferrocene energy level of 4.8 eV below vacuum, the HOMO energy levels of **47** was calculated to be - 5.14 V. No reduction wave was observed for compound **47** within the scan range of 0 to -2 V.

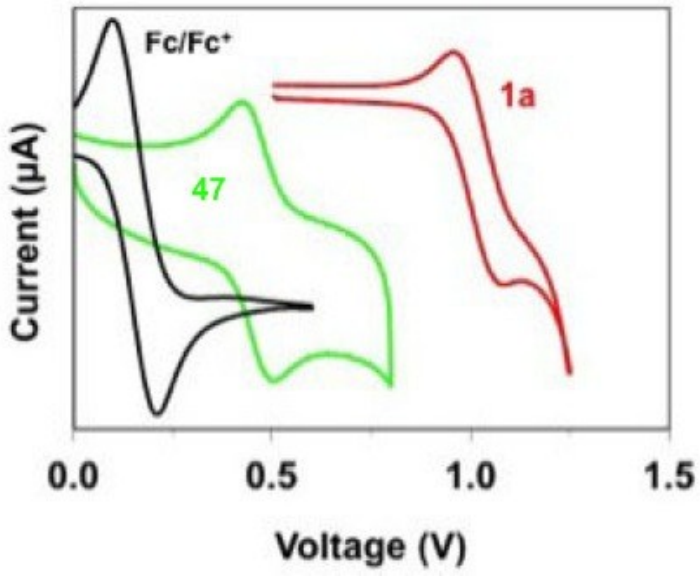

Figure 3.9. Cyclic voltammetry of **1a**, and **47** in CH_2Cl_2.

3.7 Molecular Self-Assembly of a Diphenyl-substituted Tribenzopentaphene Derivative

When methanol vapor is diffused into a chloroform solution of **47** for two days, ribbon-like structures of mm length with varied widths are obtained (Figure 3.10). Under similar conditions, **1a** instead forms fibers. The board-like assembly of **47** reflects its molecular shape where one side the TBP ring is blocked by the two phenyl substituent. The TBP core can π–π stack by alternating the two blocking substituents in one dimension to form π-stacked columns. On the lateral dimension, the opposite stretching dodecyl substituents can inter-digitate and bring adjacent columns together to form a two dimensional sheet (or ribbon). Compound **47** is thus an unique smectic mesogen.

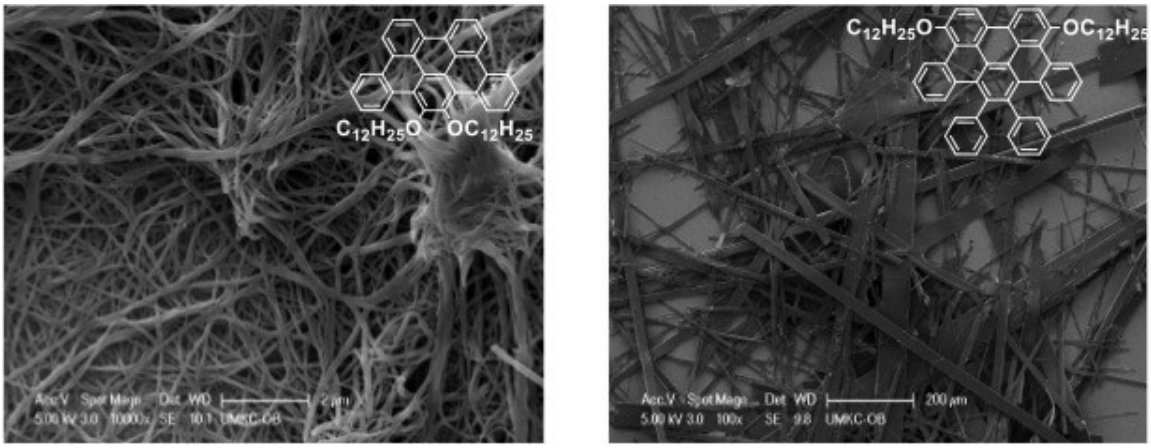

Figure 3.10. SEM images of self-assembled structures of **1a** (left) and **47** (right).

3.8 Thermotropic Liquid Crystalline Behaviors of a Diphenyl-Substituted Tribenzopentaphene

Thermal phase behavior of **47** was studied using differential scanning calorimetry (DSC). The DSC data for compound **1a** and **47** were organized in Table 3.3. Figure 3.11 shows the DSC thermograms of compound **47**. The compound was heated to 200 °C, which is a temperature higher than their melting temperature, followed by controlled cooling from 200 °C to -80 °C and were subsequently subjected to the second heating run. The scanning rate was set up at 10 °C/min. During the heating run, compound **47** showed three endothermic transitions at 72, 91, and 195 °C respectively. When coupled with polarized optical microscopy, three transitions can be assigned to C→ Col_1, Col_1→Col_2, Col_2→Iso. In the second heating run, compound **47** again showed three phase transitions at the same temperature. During the subsequent cooling process, four exothermic transitions are observed.

Table 3.3. Phase transition temperatures and enthalpies of **1a** and **47** from DSC[a].

Thermal transition T(°C) [Enthalpy changes ΔH(J/g)]	
First heating	Second heating
1a Cr 78 (36) Col_1 101.6 (30) I	Cr 64.7 (10) Col_1 101.4 (29.7) I
47 Cr 71.6(5.8) Col_1 87.6(5.5) Col_2 193.3 (29.8) I	Cr 71.7 (5.93) Col_1 87.6 (5.4) Col_2 193.3 (27.3) I

[a]Abbreviations: Col_1 Col_2 columnar phase, Cr for crystalline phase, I for isotropic phase.

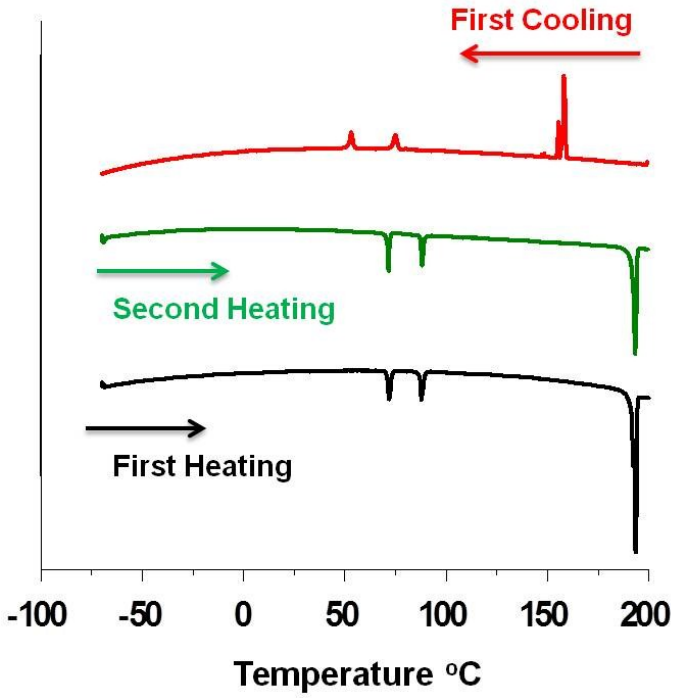

Figure 3.11. DSC thermograms of compound **47**.

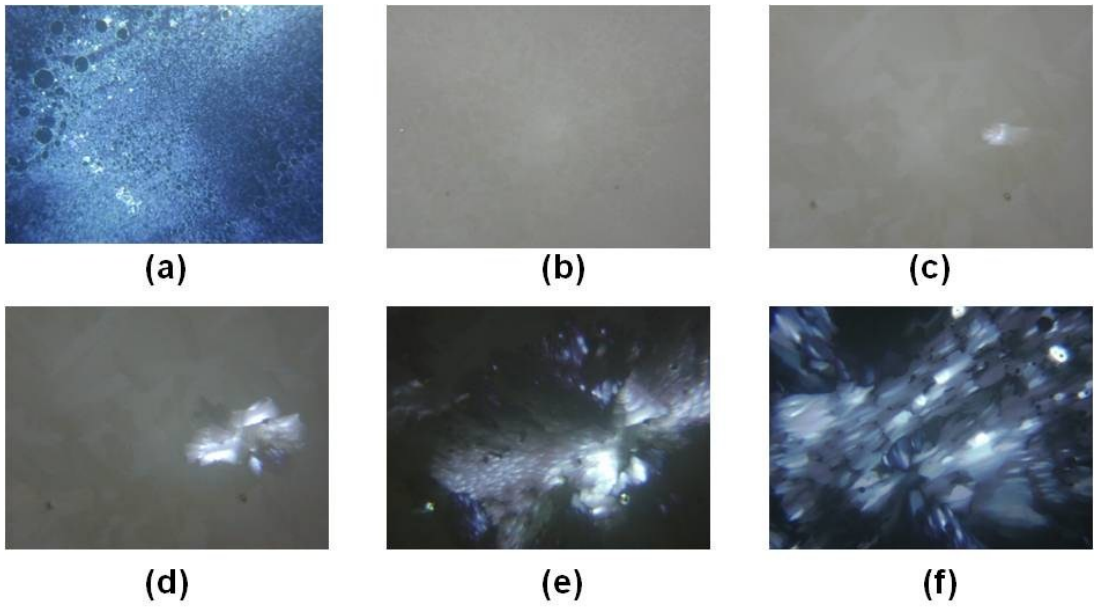

Figure 3.12. Polarized optical microscopy images of compound **47** in heating process at 25 °C (a) 196 °C (b), and cooling process at 167 °C (c), at 159 °C (d), at 95 °C (e), at 71 °C (f).

Figure 3.12 shows a series polarized optical microscopy (POM) images of compound **47**, taken at varied temperatures during cooling from their respective isotropic phase. Compound **47** was sandwiched between two glass slides and then heated to its isotropic phase, and heating/ cooling rate was set to 1 ^{o}C / mins. From POM investigation, compound **47** revealed mosaic texture which is typical for columnar mesophases.[154-157] No textural change was observed even when the sample was cooled down to room temperature.

3.9 Photoconductivity of a Diphenyl-Substituted Tribenzopentaphene

47 was used as the electron donor in a donor-acceptor heterojunction fiber, similar to the studies discussed in Chapter two. Figure 3.13 showed the photocurrent of PTCDI nanofibers coated with **47** at an applied voltage of 10 V under white light irradiation (power intensity 0.17 mW/mm^2). Under the same conditions, the PTCDI nanofiber without diphenyl TBP coating exhibits negligible photocurrent (<1 pA). When the PTCDI nanofiber was coated with **47**, its photocurrent response increased by nearly two orders of magnitude. Compared with the TBP derivatives discussed in Chapter two, the order of photocurrent response after TBP coating is **D4**> **47**>**D3**>**D1>D2** (Figure 3.14). This order is consistent with the increasing propensity for TBP π–π stacking.

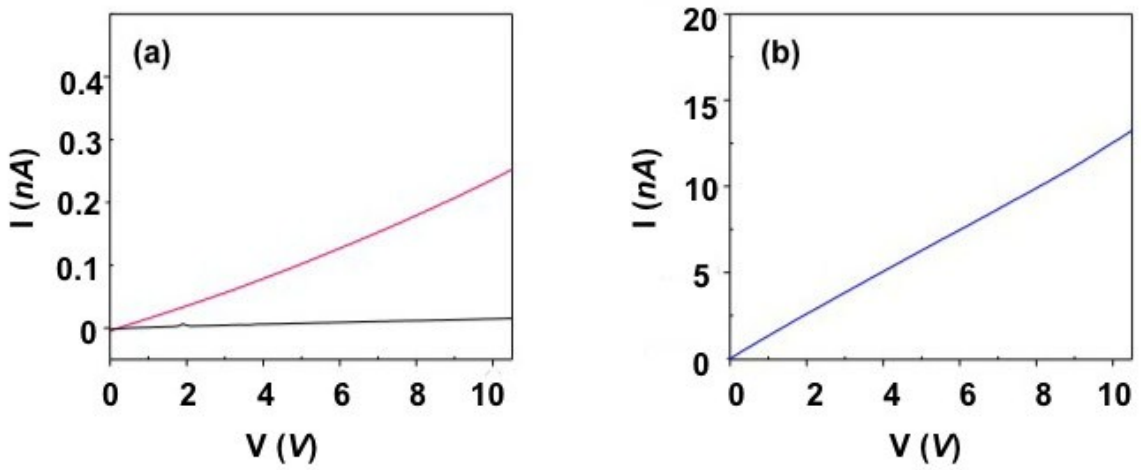

Figure 3.13. Photocurrent response of a PTCDI nanofibers before (a) and after (b) coating with compound **47**.

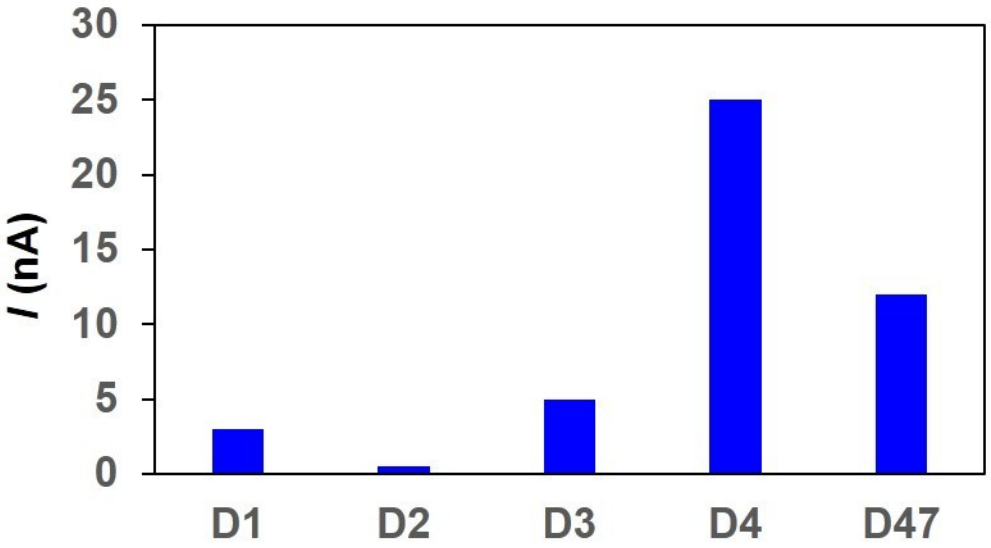

Figure 3.14. Comparison of photocurrent generation between the PTCDI nanofibers coated with the donor molecules **D1-D4** and **47**.

3.10 Conclusions

In summary, diphenyl-substituted TBP has been synthesized. This compound exhibits stronger fluorescence in dilute solutions than other TBP derivatives discussed in the previous two chapters due to the interference of the two phenyl substitutens on the TBP core π system. Due to the blocking of one side of the TBP ring, **47** adopts board-like self-assembly. The thermal behavior was also investigated by DSC and POM. Compound **47** forms a columnar mesophase. When coated on PTCDI nanofilbers, **47** can behave as photoinduced electron donors, significantly enhancing the photocurrent response.

3.11 Experimental Section

General.

All the reactions were carried out under nitrogen protection in flame-dried glassware. The solvents were used after fresh distillation over indicated drying agents and were transferred under nitrogen: THF (Na/benzophenone), CH_2Cl_2 (CaH_2). All the other reagents were purchased from Sigma-Aldrich and were used without further purification. 1-bromo-3-(dodecyloxy)benzene (**44**)[136] and 1,2-bis(3-(dodecyloxy)phenyl)ethyne (**45**)[134] were synthesized according to literature procedures.

Instrumentation.

The ^1H and ^{13}C NMR spectra were recorded on a Varian INOVA 400 MHz FT NMR Spectrometer in the solvent indicated; chemical shifts (δ) are given in ppm relative

to TMS, coupling constant (*J*) in Hz. The solvent signals were used as references[47] ($CDCl_3$: δ_C = 77.16 ppm; residual $CHCl_3$ in $CDCl_3$: δ_H = 7.26 ppm; Acetone-d6: δ_C = 206.26, 29.84 ppm; residual acetone in acetone-d6: δ_H = 2.05 ppm). UV-Vis absorption spectra were measured using a Hewlett-Packard 8452A Diode Array Spectrophotometer. Emission and excitation spectra were measured using a Shimadzu RF-5301PC Spectrofluorophotometer. Fluorescence quantum yield for solution was determined using quinine sulfate in 1N H_2SO_4 (φ = 0.58) as the standard. Cyclic voltammetry (CV) studies were carried out in freshly distilled dichloromethane for **1a** and **47** under argon protection at room temperature using a BAS Epsilon EC Electrical Station employing a 1 mm^2 Pt disk as the working electrode, a silver wire as the reference electrode, and a Pt wire as the counter electrode. $[Bu_4N]PF_6$ was used as the supporting electrolyte. The scan rate for all the measurements was set at 50 mV/s. Ferrocene was used as an internal standard. MALDI-TOF measurements were carried out on a Voyager DE Pro (Perspective Biosystem/ABI) Mass Spectrometer, operating in linear and reflector mode. Dithranol (1,8-dihydroxyanthrone) and a mixture of silver trifluoroacetate/dithranol (1:25, w/w) were used as the matrix. DSC measurements were performed on a PerkinElmer DSC8000 with a heating and cooling rate of 10 ^oC/ min.

1,2-bis(3-(dodecyloxy)phenyl)ethyne (**45**). A 100-mL round bottom flask with magnetic stir bar is fitted with a rubber septum. The flask is vacuumed and purged with dry nitrogen three times, and charged with $PdCl_2(PPh_3)_2$ (0.123 g, 6 mol%), CuI (0.056 g, 1 mol%), and compound **44** (1 g, 2.93 mmol). Septum is parafilmed after solids are added. While stirring, dry benzene (15 mL) sparged with dry nitrogen is added by syringe.

Nitrogen-sparged DBU (2.63 mL, 17.54 mmol) is then added by syringe, followed by purge of the reaction flask with nitrogen. Ice-chilled trimethylsilylethynylene (0.21 mL, 50 mol%) is then added by syringe, followed immediately by distilled water (0.02 g, 40 mole%). The reaction flask is covered with aluminum foil and heated to 60 ^{o}C under stirring at a high rate speed overnight. At the end of the reaction, the mixture was cooled down to room temperature and ethyl ether (50 mL) and distilled water (50 mL) added. The organic layer is washed with 10% HCL (3X 75 mL), saturated aqueous NaCl (1X 75 mL), dried over $MgSO_4$, gravity-filtered and the solvent removed in vacuo. The crude product was purified by silica gel column chromatography (Hexane : DCM= 5:1), and isolated the white crystals (0.45 g, 0.823 mol, 56%). ^{1}H NMR (400 MHz, CDCl3): δ7.24 (t, *J* = 8 Hz, 2H), 7.10 (d, *J* = 8 Hz, 2H), 7.05 (s, 2H), 6.88 (d, *J* = 4 Hz, 2H), 3.98 (t, *J* = 4 Hz, 4H), 1.79 (m, 4H), 1.43 (m, 4H), 1.27 (m, 32H), 0.88 (t, *J* = 4 Hz, 6H).

Compound **46**. A mixture of 1,2-bis(3-(dodecyloxy)phenyl)ethyne (**45**) (0.35 g, 0.6 mmol) and tetraphenylcyclodienone (0.246g 0.6 mmol) in dipehnyl ether (1.5 mL) was heated at reflux for 16 h under nitrogen atmosphere. After cooling to room temperature, ethanol (20 mL) was added to the reaction mixture. The solvent was evaporated and residual oil was purified by silica gel column chromatography (Hexane : DCM= 2:1), and isolated the light yellow crystal (0.48 g, 0.531 mmol, 83%); m.p.: 114~115 ^{o}C. ^{1}H NMR (400 MHz, $CDCl_3$): δ 6.86 (m, 20H), 6.77 (t, *J* = 8 Hz, 2H), 6.42 (m, 6H), 3.54 (t, *J* = 4 Hz, 4H), 1.54 (m, 4H), 1.26 (m, 36H), 0.9 (t, *J* = 4 Hz, 6H). ^{13}C NMR (400 MHz, CDCl3): δ178.1, 157.95, 141.97, 140.85, 140.46, 131.60, 127,77,

126.81, 125.48, 124.42, 117.60, 113.51, 68.28, 32.20, 29.96, 29.93, 29.65, 29.36, 29.27, 16.18, 22.97, 14.41.

Compound **47**. A solution of iron(III) chloride (0.323 g, 2 mmol) in nitromethane (2.5 mL) was added dropwise to a stirred solution of compound **46** (0.2 g, 0.22 mmol) in dichloromethane (40 mL). A dry nitrogen stream was bubbled through the reaction mixture throughout the entire reaction. After stirring another 2 h, the mixture was quenched with methanol (20 mL) and stirred for another 1 h. The precipitate was filtered and washed with methanol (20 mL), and dried under reduced pressure. The crude product was purified under by silica gel column chromatography (Hexane : DCM= 10:1); m.p. : 184~185 ^{o}C. ^{1}H NMR (400 MHz, CDCl3): δ9.54 (d, *J* = 8 Hz, 2H), 8.78 (d, *J* = 8 Hz, 2H), 8.17 (d, *J* = 8 Hz, 2H), 7.65 (d, *J* = 8 Hz, 2H), 7.39 (t, *J* = 8 Hz, 2H), 7.25 (m, 4H), 7.11 (m, 8H), 4.38 (t, *J* = 8 Hz, 4H), 2.08 (m, 4H), 1.68 (m, 4H), 1.46 (m, 4H), 1.27 (m, 28H), 0.89 (t, *J* = 4 Hz, 6H). ^{13}C NMR (400 MHz, $CDCl_3$): δ 155.26, 142.94, 138.28, 132.99, 131.23, 130.58, 130.17, 128.50, 127.56, 126.97, 126.05, 125.67, 125.56, 124.89, 124.53, 123.08, 121.97, 118.98, 112.35, 69.67, 31.88, 29.65, 29.61, 29.59, 29.45, 29.32, 26.43, 22.65, 14.09.

CHAPTER 4

SYNTHESES AND OPTICAL PROPERTIES OF TRIPHENYLENE-CONTAINING CONJUGATED FOLDAMERS

4.1 Introduction

Conjugated oligomers and polymers which can self-organize into a helical conformation have been extensively studied[137]. Such studies have not only led to a much better understanding of the principles behind non-covalent folding[138], but also brought about a number of exciting applications from selective and specific guest binding[139], functional group organization[140], to reactive sieves[141]. The major driving forces responsible for the folding of π-conjugated systems are π–π stacking and solvophobic interactions[137]. The strength of the π–π interaction depends on the size and the electronic nature of the aromatic systems, and is very sensitive to solvent. In general, the larger the size of the planar aromatic system, the stronger the π–π interaction[142]. Interestingly, studies on conjugated foldamers have so far been limited to systems based on m-phenyleneethynylenes (mPEs)[137,138], oPEs[143], and their pyridyl analogs[144], all involving only single-ring aromatic systems in which the mere existence of π–π interactions is questionable[145]. Polycyclic aromatic systems (PCAs), as far as we know, have not been utilized in conjugated foldamers.

4.2 Brief Histories and Recent Advances on Helical Polymers and Foldamers

Helical biological macromolecules such as protein and DNA are the ubiquitous structure in nature. The history of helical polymers can trace back to the 1950s. In 1951 Pauling, Watson and Crick discovered the right handed α-helix for protein[146], and in 1953 they further found the right-handed double stranded helix for DNA.[147] The inspiring discovery of biological helical structures started molecular biology and remarkable progress has been made.[148,149] At about the same time, Natta synthesized isotactic polypropylene which adopts helical conformation.[150] So far, numerous isotactic or syndiotactic polymers have been synthesized and their helical conformations in crystalline state have been studied.[151]

In the 1960s, Pino and coworkers investigated a serious of optically active isotactic vinyl polymers which were synthesized by α-olefins with optically active substituents.[152] This was the first time that the helical conformation of synthetic vinyl polymers with an excess one-handed helical sense in solution had been revealed. The conformations of these helical polyolefins are however dynamic, with the backbone composed of short, randomly distributed helical segments with reversed helical senses.[153]

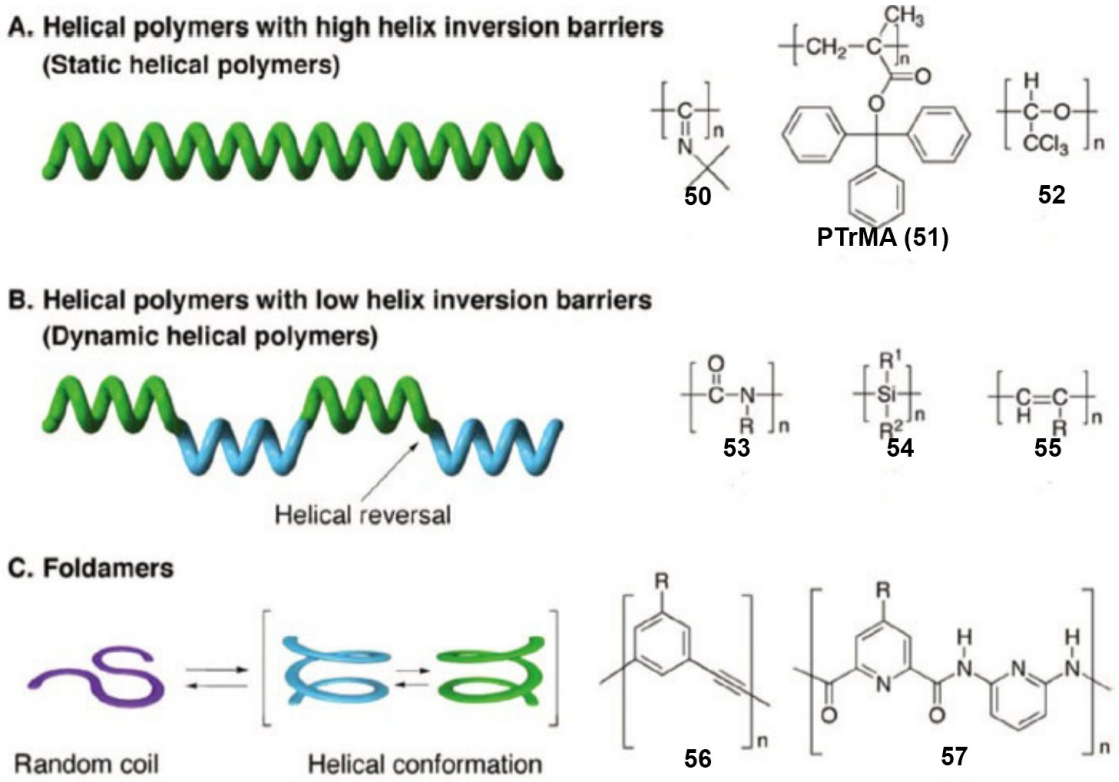

Figure 4.1. Three types of helical polymers and their representative structure.[156, 162]

In 1974, Nolte and Drenth et al. successfully isolated enantiomerically pure right- and left-handed helices of poly(tertbutyl isocyanide) **50** by chiral chromatography (Figure 4.1A).[163] Five years later, Okamoto and Yuki, et al. reported an optically active helical vinyl polymer (PTrMA, **51**)[164] using a chiral anionic initiator. The PTrMA is a fully isotactic helical polymer with a large specific rotation, confirming for the first time that stable helical conformation of polymers in solution can be realized. The one-handed helical PTrMA was used as the chiral stationary phase (CSP) in high performance liquid chromatography (HPLC), successfully recognizing and separating racemic compounds. [165] In 1980, Vogl and co-workers synthesized isotactic polychloral (**52**).[166] The helical

structure of this polymer has been confirmed by NMR and X-ray crystallographic analyses.[167,168]

In 1988, another type of helical polymer, dynamic helical polyisocyanates (**53**), were discovered by Green, et al.[169] The polyisocyanate polymers consist of interconvertible right- and left-handed conformations. It was shown that a small chiral bias through covalent or noncovalent bonding interaction can lead to a large excess in helical sense of the entire polymer chain, establishing the principles of so-called "Majority Rules" and "Sergeants and Soldiers". Adopting the same approaches, optically active helical polymers such as polysilanes (**54**),[170] polyacetylene (**55**),[171,172] and others have been reported. These dynamic helical polymers have a very low helix inversion barrier. A small amount of chiral bias can induce one-handed helical conformation (Figure 4.1 B).

Conjugated foldamers are another class of helical polymers which are shape persistent. (Figure 4.1C).[173] Moore,[137] and Hamilton,[174] Lehn,[175] Huc,[156] etc are pioneers in studying conjugated foldamers. Moore and coworkers synthesized a number of m-poly(phenylene ethylene)s (mPE, **56**).[176] The backbone curvature created by the meta-linkage (120° angle), the π–π stacking interaction and the solvophobic interaction lead to backbone folding.[177] When tri(ethylene glycol) Tg was used as the side chain in the mPE, the favorable interaction of the side chain with polar solvents (such as acetonitrile) drives the backbone folding.

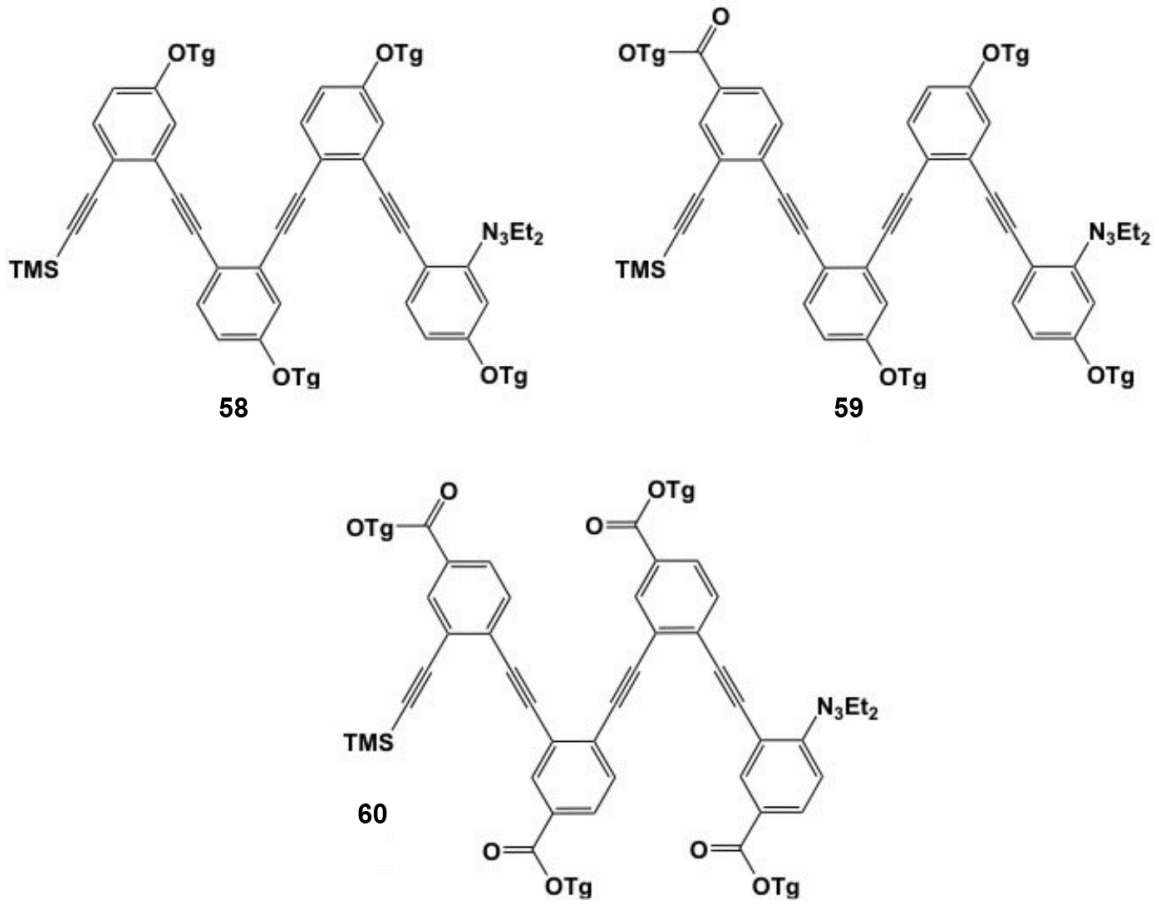

Figure 4.2. Three otho-linked phenylene ethylene (oPE) oligomers.

Tew and colleague synthesized ortho-linked penylene ethylene (oPE) oligomers (Figure 4.2).[178] The oPE oligomers were found to adopt folded conformation in acetonitrile. The larger backbone curvature created by the smaller bond angle (60^{o}) angle allow a full turn with only three repeat units.

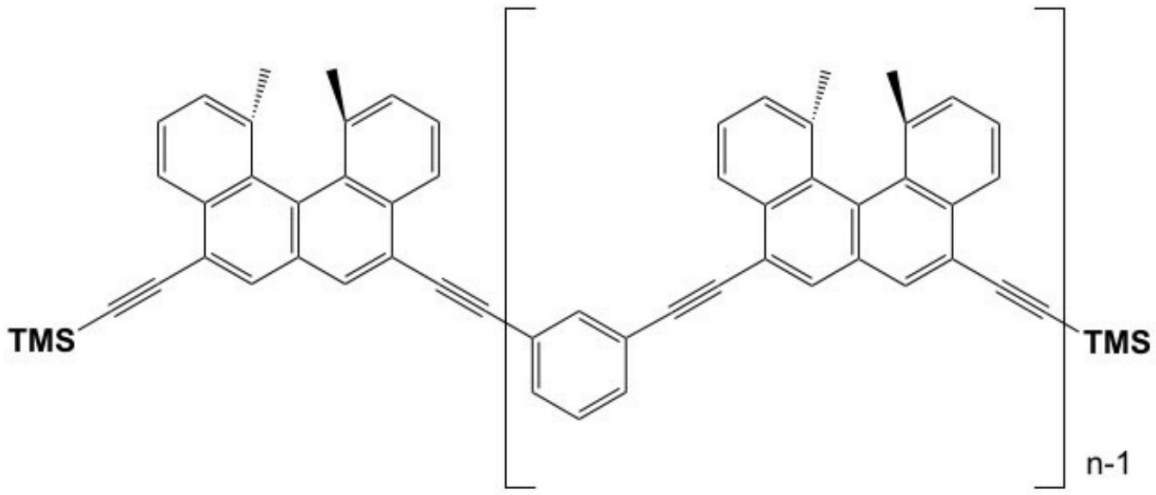

61 , n=2-9

Figure 4.3. Helical ethynylhelicene oligomers.

In 2004, another foldamer, ethynylhelicene oligomers (**61**), were reported, and their folding properties were studied by circular dichroism (CD) and NMR spectroscopy. Helical conformations were identified when the number of repeating units was more than 7. Foldamers based on flexible backbones have also been reported. Naphthalene-based polyether **62** is one example which adopts folding conformation in polar solvents.[180] Folding of **62** creates a cavity which is comparable to 18-crown-6 and can form complexes with ammonium or ethan-1,2-diaminium ion.

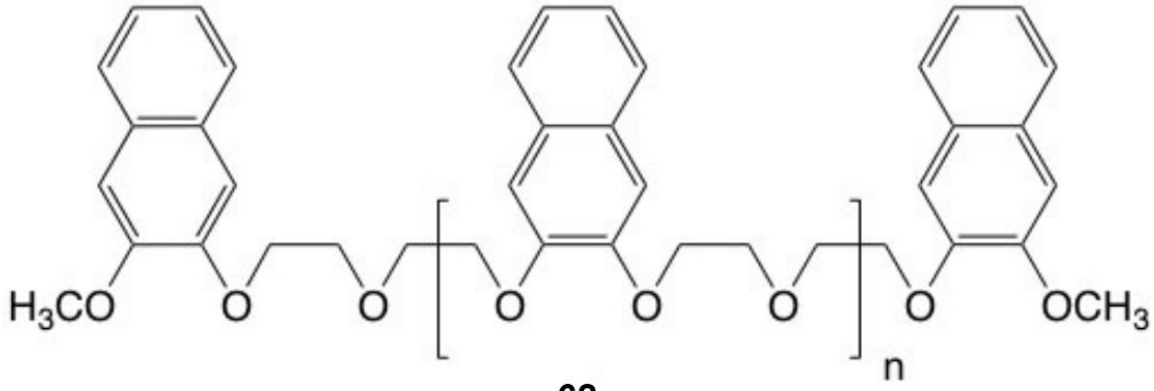

62

Figure 4.4. Oligpnaphthalene foldamers

4.3 Objectives

One of the driving forces for folding of π-conjugated systems is the π–π stacking interaction which makes folding enthalpically favorable. Since π–π stacking interactions are stronger for larger polycyclic aromatic systems (PCAs), polymers containing PCAs are expected to have higher propensity for folding. Surprisingly, conjugated foldamers based on PCS building blocks, as far as we know, have not yet been reported. It is envisioned that with PCAs in the conjugated polymer backbone the polymer will not only exhibit much stronger propensity for folding due virtually to their stronger π–π stacking interactions, but also may lead to conjugated systems with very interesting electronic and optical properties. For example, it is known that π-stacked columns formed from some PCAs exhibit strong electron delocalization among[182] and high-charge mobility through the stacked columns.[183] Foldamers based on PCA-containing conjugated polymers which form multiple PCA-stacked columns after folding may thus exhibit efficient charge-transport, a property which is crucial for some polymer-based electronic devices, such as

polymer light-emitting diodes, field-effect transistors, and solar cells.[184] In this chapter, we report the synthesis and optical properties of a triphenylene-containing mPE whose structure is shown in Figure 4.5. Triphenylene derivatives are one of the most common discotic mesogens,[185] which have a tendency to form π-stacked discotic liquid crystalline phases that facilitate both energy and hole transport.[186] The strong π-stacking tendency is expected to enhance the backbone folding. To further promote folding, the triphenylene unit is linked to the polymer backbone through its 2 and 11 positions. Such a linkage not only ensures the full conjugation of triphenylene chromophore's π system into the polymer backbone, but it also results in a 60° turn of the backbone. A fully and closely folded polymer thus possesses two triphenylene-stacked columns (Figure 4.5). Our results indicate that mPPET indeed folds in a variety of solvents. Depending on the solvents, this polymer may also adopt a random coil conformation or interchain aggregation. Among the three conformations, the folding conformation is found to exhibit the highest fluorescence quantum yield.

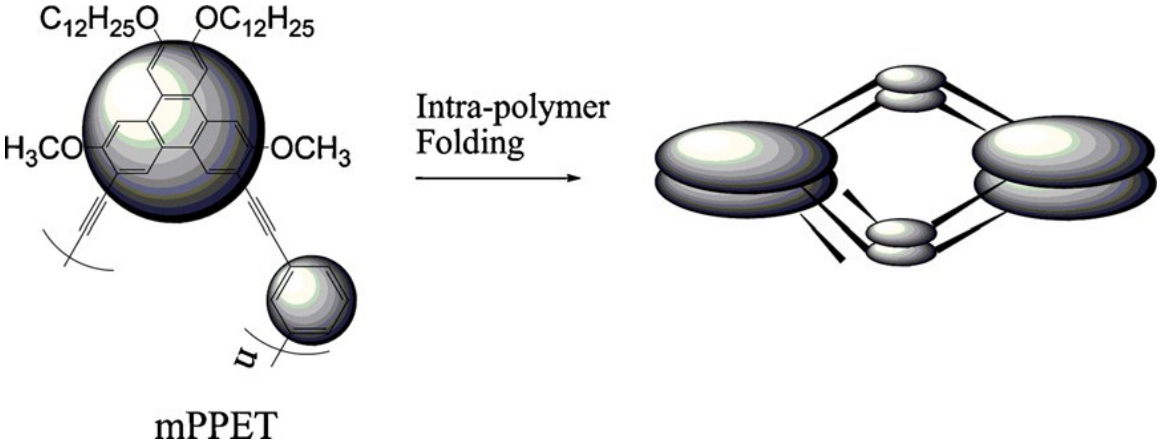

Figure 4.5. A triphenylene-containing foldamer, m-PPET and its presumed folding.

4.4 Synthesis and Characterization of Triphenylene-Based Foldamer mPPET

The mPPET polymer contains meta-linked phenyl rings and 2, 11-linked triphenylenes. Triphenylene's 7 and 10 positions are π-conjugated while the meta-linkage of the phenyl ring interrupts conjugation.[189] A monomeric unit which possesses the same extent of π-conjugation as mPPET and thus reflects the optical properties of unfolded mPPET should thus include the 7,10-bis(phenylethynyl) triphenylene segment. Since meta-branching does impact the optical properties of the π-system, compound **I** which includes an additional ethynyl group at the meta-position of each phenyl ring is therefore chosen as the model compound. This compound helps identify the unfolded and non-aggregated (random coil) conformation of mPPET. As mentioned earlier, the fully folded mPPET contains two stacked triphenylene columns. If one looks through the folded helix, one sees a diamond shaped macrocycle. This macrocycle, compound **II**, is also synthesized as a model compound. This planar macrocyle cannot fold intra-molecularly, but may stack inter-molecularly, and is therefore useful for distinguishing mPPET's intra-chain folding conformation from its' inter-chain aggregation.

mPPET and model compounds **I** and **II** were all synthesized by the Sonogashira coupling reaction according to Scheme 1. Sonogashia reaction worked well in all cases except for the ring formation step where the best yield achieved was 25%. High dilution is required for cyclization and thus the reaction was carried out by adding slowly and dropwise the two reactants (**63** and **I**) into the catalyst-containing reaction mixture. In contrast, polymerization was carried out in high concentrations. Even so, cyclic oligomers may not be completely excluded. As a matter of fact, gel-permeation chromatography (GPC) shows two separated peaks for mPPET, one with a number

average molecular weight of 32.5 KDa and a polydispersity of 1.8, and the other with a lower molecular weight of about 8.7 KDa (Figure 4.9). The lower molecular weight component is a minor fraction (less than ¼ of the major fraction) and is likely composed of cyclic oligomers.

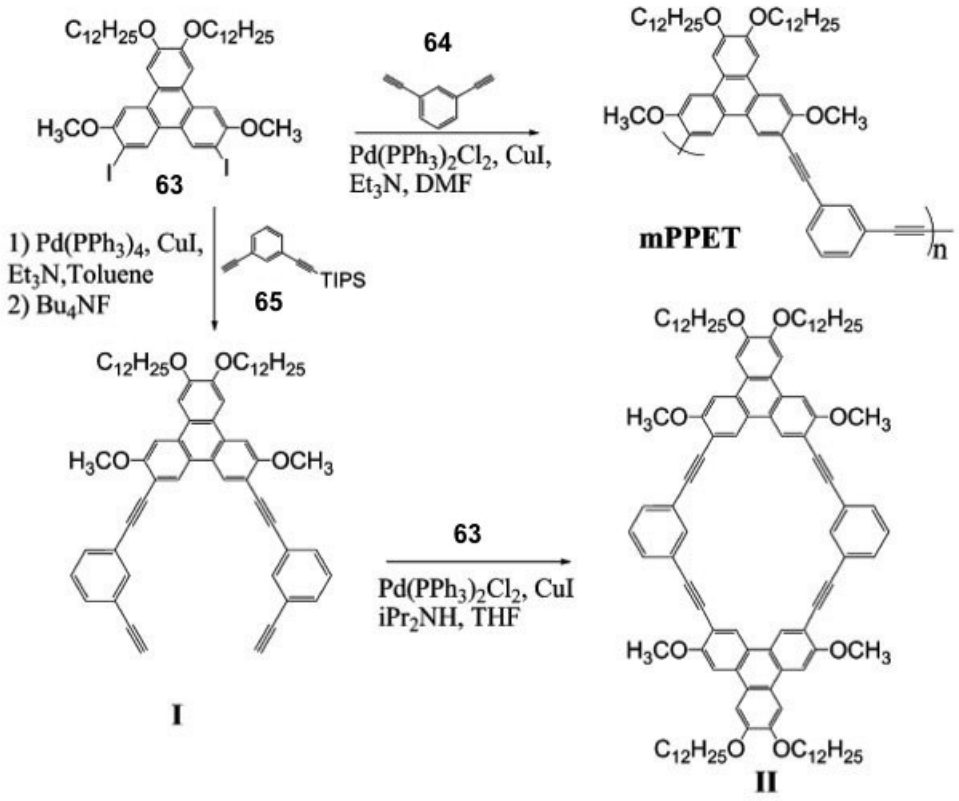

Scheme 4.1. Synthesis of mPPET and two model compounds.

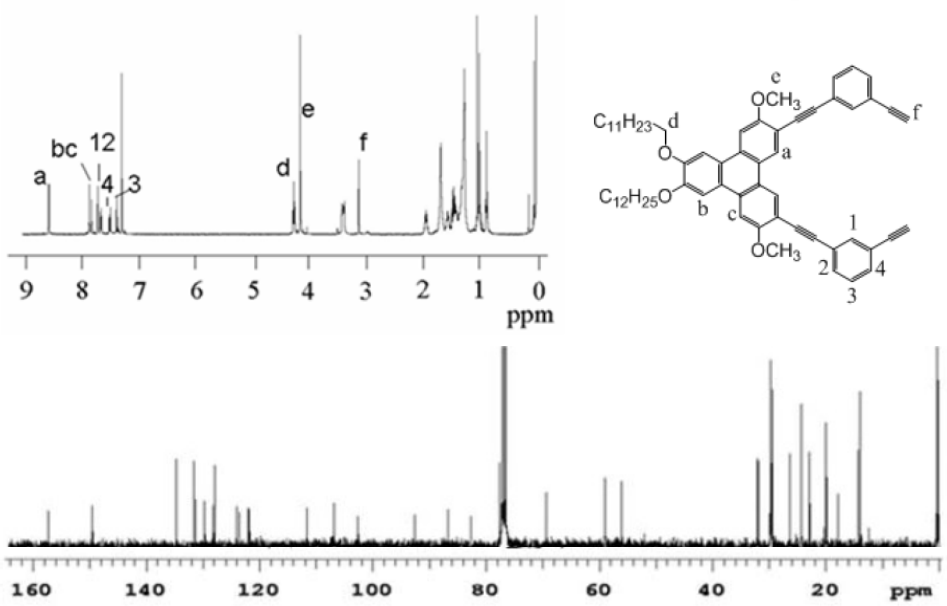

Figure 4.6. ^{1}H and ^{13}C NMR spectrum of model compound **I** in $CDCl_3$.

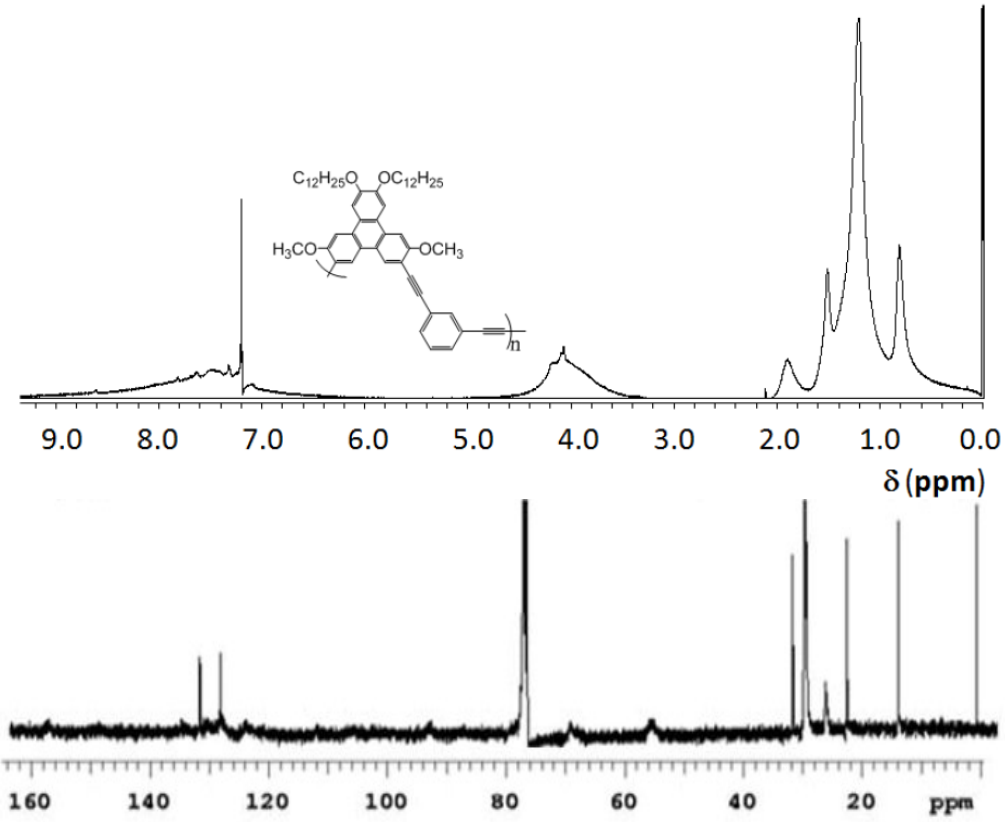

Figure 4.7. ^{1}H and ^{13}C NMR spectrum of mPPET in $CDCl_3$.

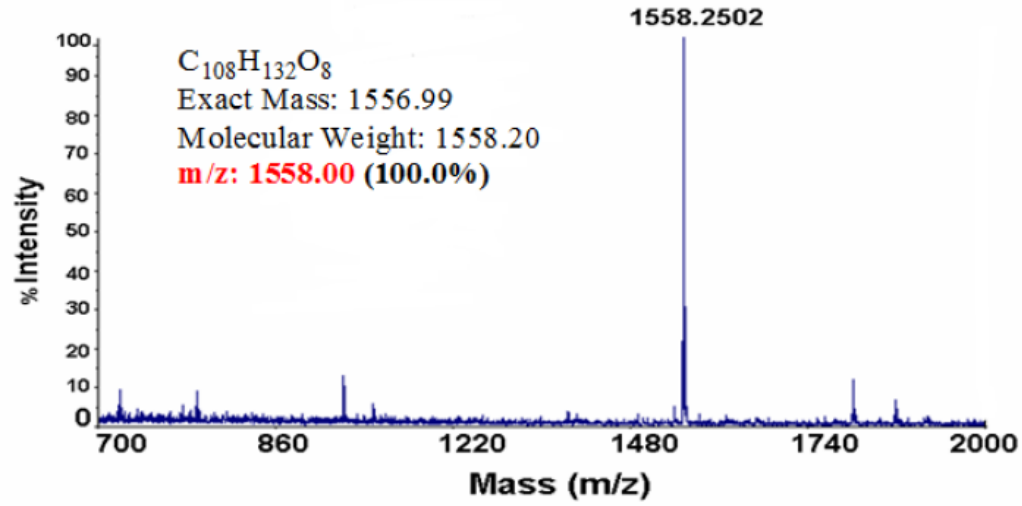

Figure 4.8. MALDI-TOF MS of model compound **II**

The ^{1}H NMR spectrum of **I** in $CDCl_3$ gives well resolved sharp signals in the aromatic region, which all can be unambiguously assigned (Figure 4.6). **II** and mPPET, however, both show an extremely broad hump all the way from 6.2 ppm to 8.4 ppm. The signal corresponding to $–OCH_2–$ and $–OCH_3$ at around 4.0 ppm is also very broad (from 3.5 ppm to 4.4 ppm). Other alkyl signals show no such atypical broadness. Apparently, the closer the proton to the aromatic π-system, the broader its signal becomes, indicating it is the π–π stacking that leads to the signal broadening. The π-stacking-induced signal up-field shift is also apparent.[188] For example, the broad aromatic signal of mPPET extends down to 6.2 ppm while model compound **I** shows no aromatic signal below 7.3 ppm. Sitting on the broad hump, one can identify a few discernible aromatic signals

whose chemical shifts match well with those of compound **I**, indicating the coexistence of some non-aggregated polymers in solution. The ^{13}C NMR spectrum of the polymer shows four sharp signals in the aromatic region and sharp signals in the aliphatic region. All the other aromatic and OCH_2–, OCH_3 ^{13}C signals are however broad, reflecting again strong aggregation. The sharp aromatic signals may be attributed to ethynyl phenyl end groups which exhibit rotational flexibility. The fact that these sharp signals were observed in the ^{13}C NMR spectrum of **I**, but not that of 2,3-bis(dodecyloxy)-7,10-diethynyl-6,11-dimethoxyltriphenylene provides additional support that these signals come from phenyl carbons, not triphenylene carbons.

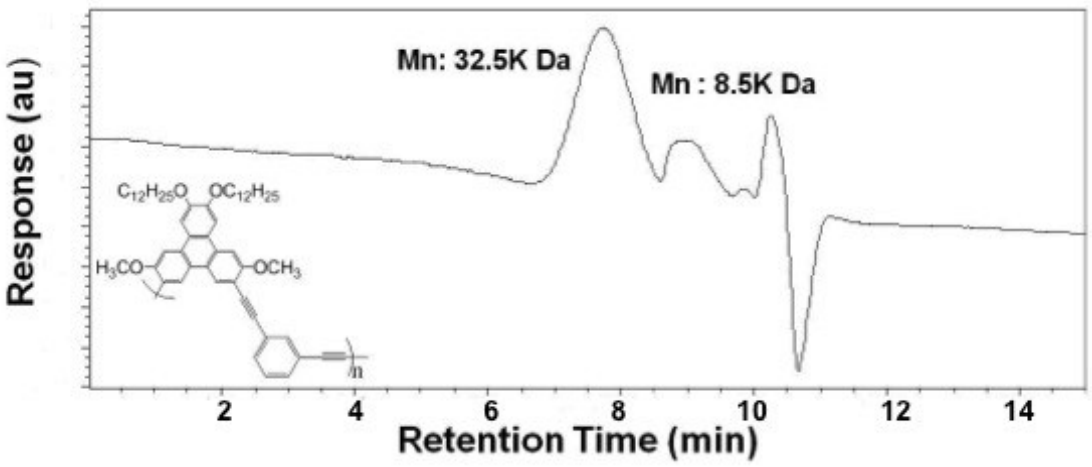

Figure 4.9. GPC trace of mPPET.

4.5 Results and Discussions

Compound **I** is soluble in most common organic solvents, such as chloroform, THF, benzene, hexane, acetonitrile, DMSO, etc. Compound **II** and mPPET, however, are soluble in chloroform, THF and benzene, but show negligible solubility in hexane, acetonitrile and DMSO. Their absorption spectra in chloroform (a good solvent) and acetonitrile (a poor solvent for II and mPPET) are shown in Figure 4.10. The acetonitrile solution of **II** or mPPET was prepared by adding one drop of its chloroform solution into acetonitrile. In chloroform, mPPET and the two model compounds all show two absorption peaks at around 300 nm and 344 nm. In the longer wavelength range, compound **I** shows another clear peak at 392 nm while **II** and mPPET give a corresponding shoulder. There is a 4-nm red shift in band edge from **I** to **II** and from II to mPPET. Other than these minor differences, mPPET and the model compounds show very similar absorption spectra, as expected by the meta-linkage of the phenyl ring which breaks π-conjugation. In acetonitrile, compound **II** and mPPET show nearly identical spectra beyond 300 nm and possess the same band edge. The red shift in band edge for **II** is attributed to the inter-ring π–π stacking. Compound **I**, which is soluble in acetonitrile, gives essentially identical spectrum in both chloroform and acetonitrile.

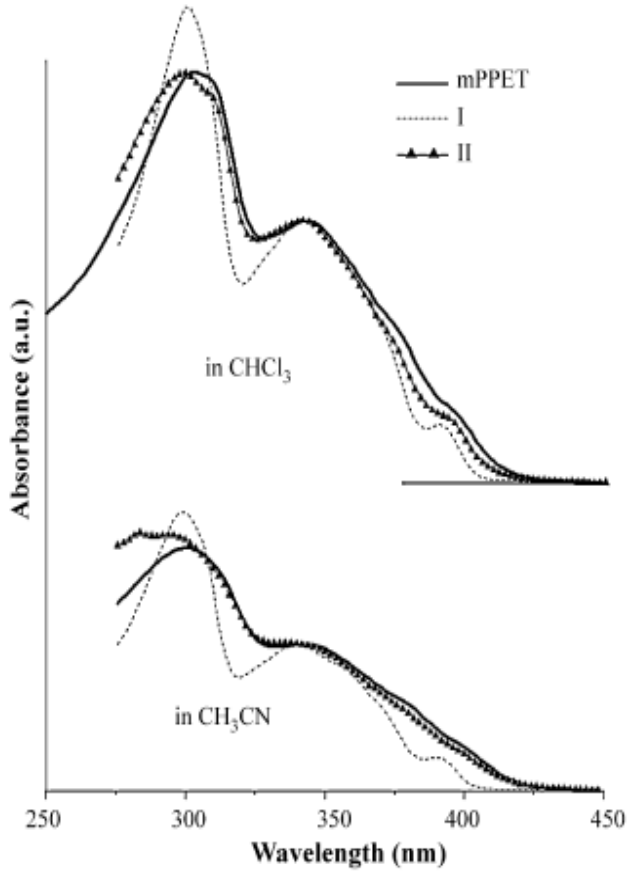

Figure 4.10. UV–vis absorption spectra of mPPET, **I** and **II** in chloroform (top) and acetonitrile(bottom).

While mPPET exhibits very a similar absorption spectrum, particularly to that of **II**, their fluorescence emission spectra are vastly different, as shown in Figure 4.11. In dilute chloroform solutions, where they are all soluble, **I** and **II** give identical structured emissions with λ_{max} at 400 nm and 422 nm. Further dilution results in no change in spectral shape or emission wavelengths. Such an emission (with λ_{max} at 400 nm) should therefore be attributed to the non-aggregated monomer species for **I** and **II** and should also represent the emission of mPPET when it is in the non-aggregated and non-folded

random coil conformation. Interestingly, the dominant emission of mPPET in chloroform is a broad structureless emission centered at 440 nm, although a shoulder at 400 nm is noticeable, indicating that the majority of the mPPET polymer is not in the random coil conformation. In CH_3CN, compound **I** shows the same structured monomer emission. Compound **II** however gives, in addition to emissions peaked at 400 nm and 422 nm, a broad significantly red-shifted hump at 480 nm. For mPPET, such a significantly red shifted broad peak with a λ_{max} at 492 nm is the only one seen in its emission spectrum. As mentioned earlier, acetonitrile is a poor solvent for both **II** and mPPET. **II** is a planar (or at least close to planar) conjugated macrocycle with two triphenylene units as anchoring components. Considering the fact that even mPE-based macrocycles are prone to intermolecular stacking to form self-assembled tubes,[190] compound **II** is expected to have even higher tendency for intermolecular aggregation.[191] The broad red-shifted peak of **II** can thus be assigned to an excimer emission from its intermolecular aggregates. Such an assignment is consistent with the observation that films made of I or mPPET show very similar broad and red-shifted emissions (Figure 4.11(c)). For mPPET, one may conclude with a similar argument that the broad and significantly red-shifted emissions of mPPET in acetonitrile are dominated by interchain aggregates, although intra-chain folding cannot be excluded. One remaining question is what conformation then contributes to the broad emission at 440 nm when mPPET is dissolved in chloroform. The broadness and the lack of vibronic feature of the signal excludes monomeric emission and points to some sort of aggregation. The fact that under even extremely dilute conditions this broad emission still dominates indicates that the aggregation is an intra-chain process, suggesting a possible folding conformation in chloroform.

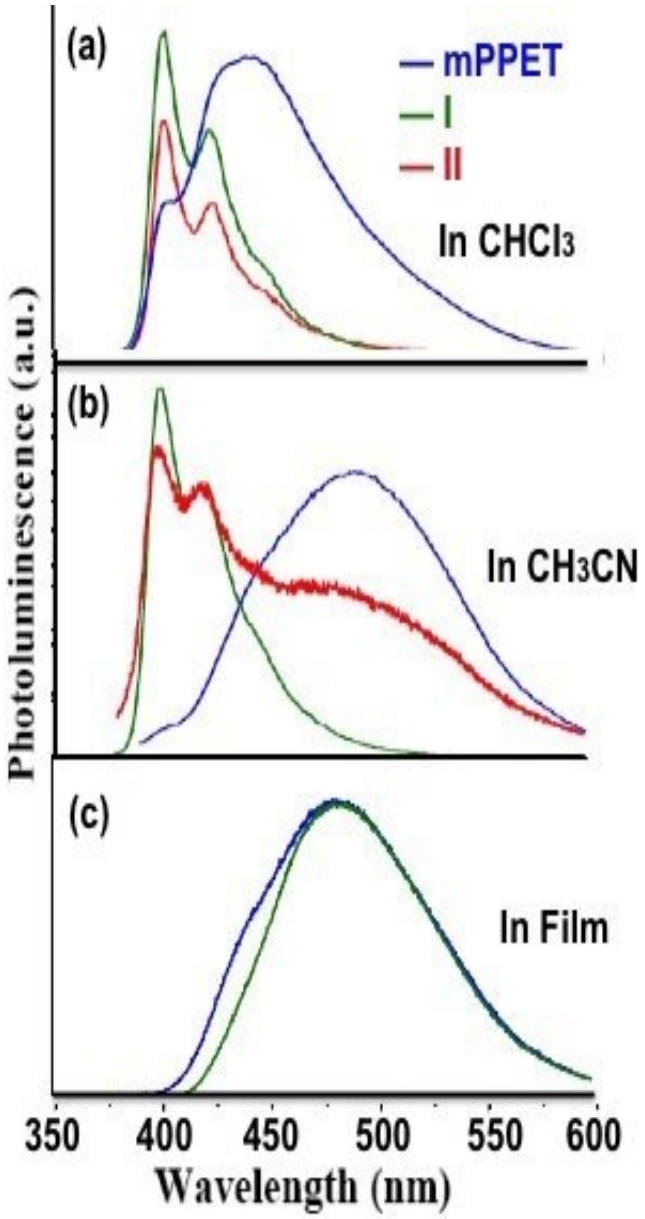

Figure 4.11. Fluorescence emission spectra of mPPET, **I** and **II** in CHCl3 (a), CH3CN (b) and as thin films (c).

To confirm that the exciton giving the broad emission at around 440 nm is different from that yielding the 400 nm emission for mPPET, the excitation spectra corresponding to emission wavelengths at 400 nm and 450 nm were recorded for both model compound **I** and mPPET in dilute chloroform solutions. As shown in Figure 4.12(a), the two excitation spectra for model compound **I**, after normalization, match each other perfectly, indicating that the two emission peaks come from the same excited state. For mPPET, however, the two excitation spectra (Figure 4.12(b)) do not match each other, particularly in the long wavelength region, indicating that the species responsible for the emission at 450 nm is different from that responsible for the 400 nm emission.

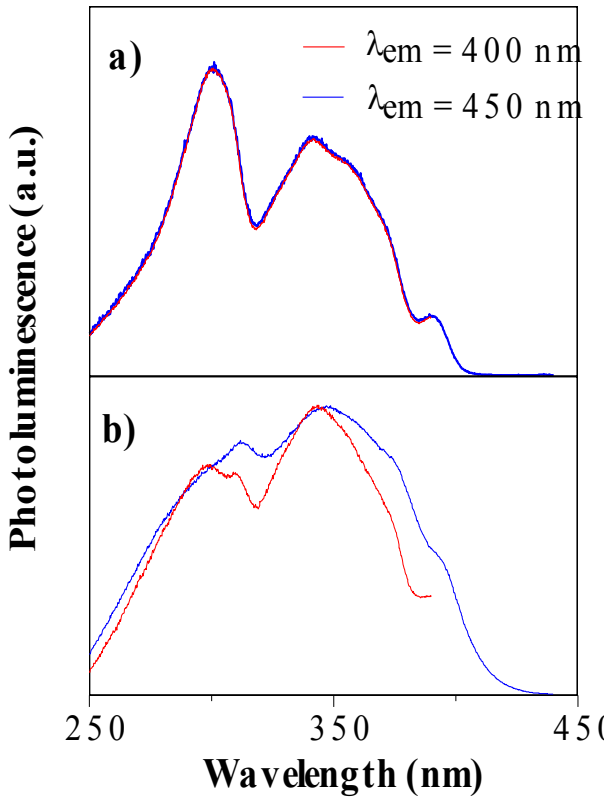

Figure 4.12. Excitation spectra of **I** (a) and mPPET (b) in chloroform.

To see how emissions change when solvent composition is varied, an acetonitrile solution of mPPET was continuously diluted with chloroform and the solution emission spectra were recorded. The opposite dilution process, meaning diluting a chloroform solution with acetonitrile was also carried out. The emission spectra, after concentration correction, are shown in Figure 4.13. As stated earlier, mPPET in acetonitrile shows a broad emission at 492 nm. As the chloroform content increases, the monomeric emission (λ_{max} = 400 nm) increases. When the chloroform content is in the range 18–40%, the monomeric emission dominates. As the chloroform content further increases, the presumed foldamer emission (broad emission with λ_{max} around 442 nm) starts to dominate. It is also noted that the fluorescence quantum yields continue to increase as the chloroform content increases. If the two solvents are switched where a chloroform solution is continuously diluted with acetonitrile, the spectral change is reversed. As shown in Figure 4.13(b), as acetonitrile is added and the chloroform content decreases, the emission changes from foldamer emission (λ_{max} at 440 nm) to monomeric emission (λ_{max} at 400 nm) and to interchain aggregate emission (λ_{max} at 492 nm). The conformation change is clearly reversible and reproducible.

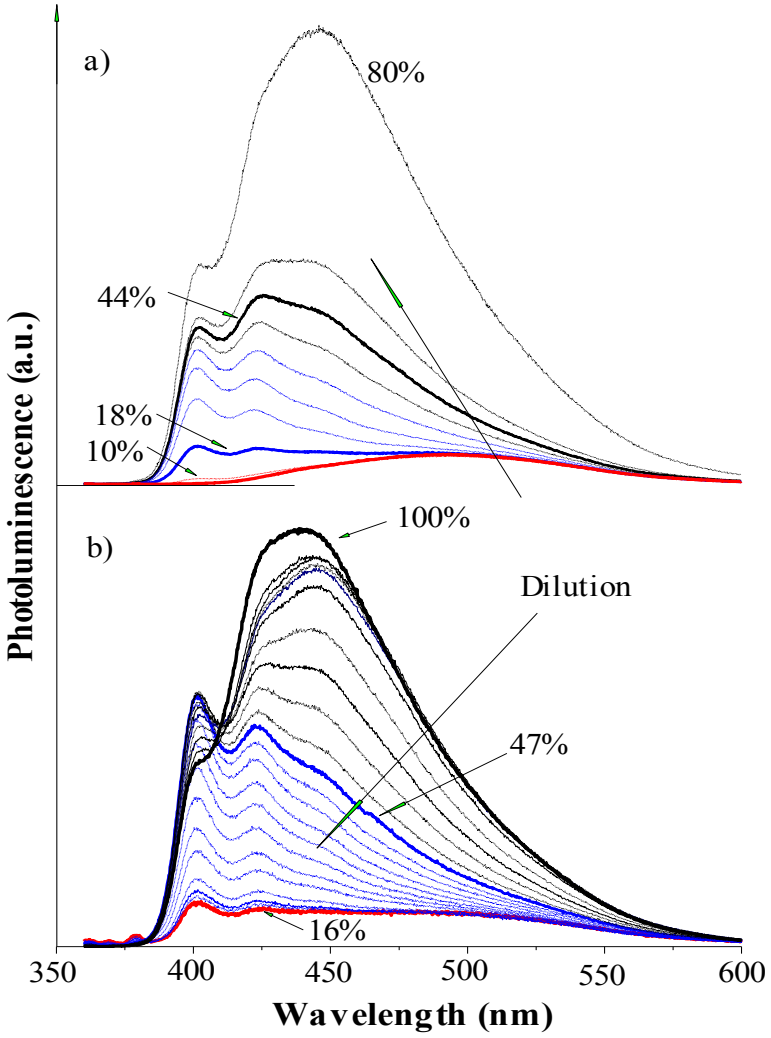

Figure 4.13. Emission spectra of mPPET in (a) CH_3CN diluting with $CHCl_3$ and (b) $CHCl_3$ diluting with CH_3CN. The percentage shown in the figure indicates chloroform content.

Realizing that both the polymer concentration and the solvent content were changed in the above dilution experiments, we prepared three mPPET solutions, one in chloroform, one in acetonitrile and one in a mixed solvent with a 1:2 chloroform/acetonitrile ratio, with identical absorbance at 344 nm (~0.1) so that all three polymer solutions have close concentrations. Their UV–vis absorption spectra and their fluorescence emission spectra are shown in Figure 4.14. Except for a slightly high extinction coefficient for the two solutions with acetonitrile as part or the sole solvent, all three solutions give very similar absorption spectra. Their emission spectra are however clearly different and consistent with the previously discussed dilution experiments. In pure chloroform, the broad emission at λ_{max} 440 nm dominates, while in acetonitrile, emission from interchain aggregates is overwhelming. In the mixed solvent, monomeric emission is dominant. Not only different conformations give very different emission spectra, their fluorescence quantum yields are also vastly varied. The fluorescence quantum yields of mPPET in chloroform, acetonitrile, and the chloroform–acetonitrile 1:2 mixture are 15%, 1% and 4%, respectively. In other words, the folding conformation, among the three, is mostly emission.

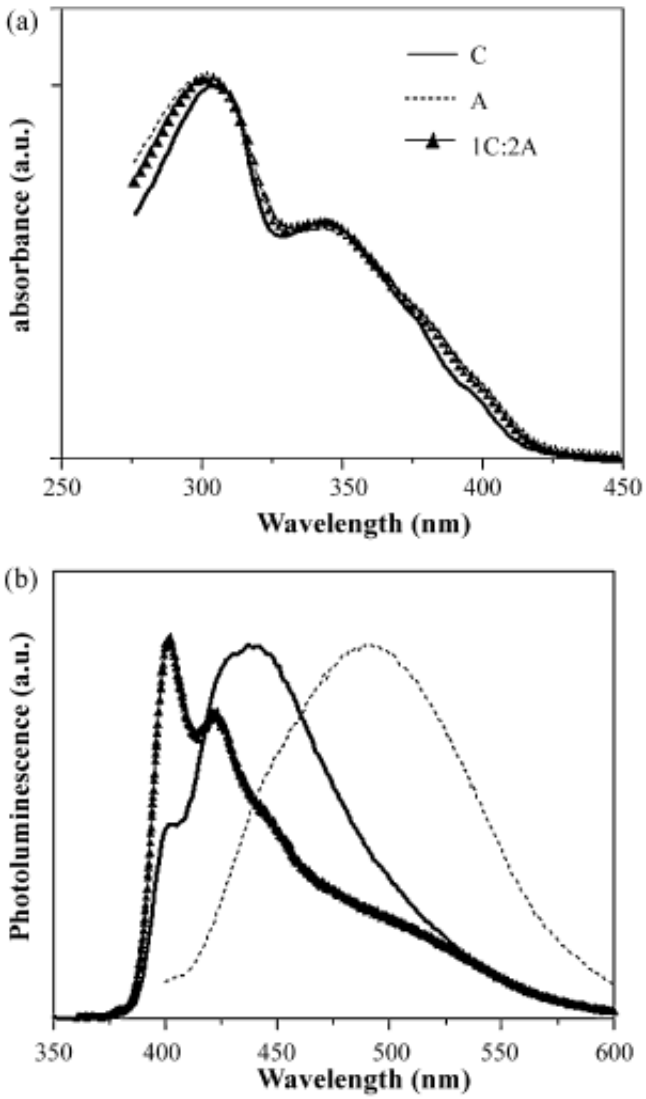

Figure 4.14. Absorption (top) and fluorescence emission (bottom) spectra of mPPET in chloroform (C), acetonitrile (AN), and a 1:2 chloroform/acetonitrile mixture.

It is expected that mPPET in acetonitrile exhibits the lowest fluorescence quantum yield, as interchain aggregation usually brings about fluorescence quenching. In the mixture solvent, while emissions from non-aggregated random coil conformation dominate, emissions from interchain aggregates are nonetheless clearly observable (Figure 4.15), which may account for its low fluorescence quantum yield. In chloroform, mPPET shows a surprisingly high fluorescence quantum yield, which seems to contradict with its presumed folding conformation. Coupled with the fact that a much smaller red-shift is observed for intra-chain folding than that of interchain π-stacking, it appears possible that different π–π interactions are involved in intra-chain folding vs interchain stacking. For mPPET and model compounds **I** and **II**, intermolecular aggregation involves offset co-facial π-stacking which quenches fluorescence and leads to significantly red-shifted emissions. The emissions may be excimer-like through triphenylene–triphenylene stacks or exciplex-origin through triphenylene–phenylene alternate stacking. For intrachain folding of mPPET, due to the small 60◦ angle at the triphenylene linkage and the small number of vertex points (4) for a folded full turn, significant twisting of the π systems is expected. To help elucidate the folding conformation, we have taken tetramer III, whose structure is shown in Figure 4.16, as the model for mPPET and explored its lowest energy conformation in both gas phase and aqueous solution. The conformational searches were performed using the Monte Carlo molecular mechanics (MC/MM) algorithm, within the OPLS-2005 force field[192-193] as implemented in the MacroModel program of the Maestro 8.5 molecular modeling environment.[194]

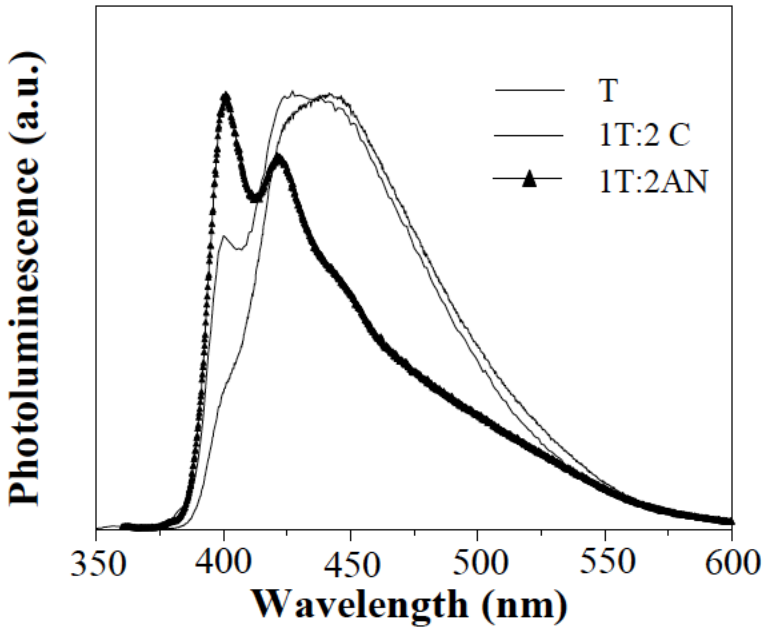

Figure 4.15. FL emission spectra of mPPET in THF (T), THF/Chloroform mixture (1T:2C) and THF/acetontrile mixture (1T:2AN).

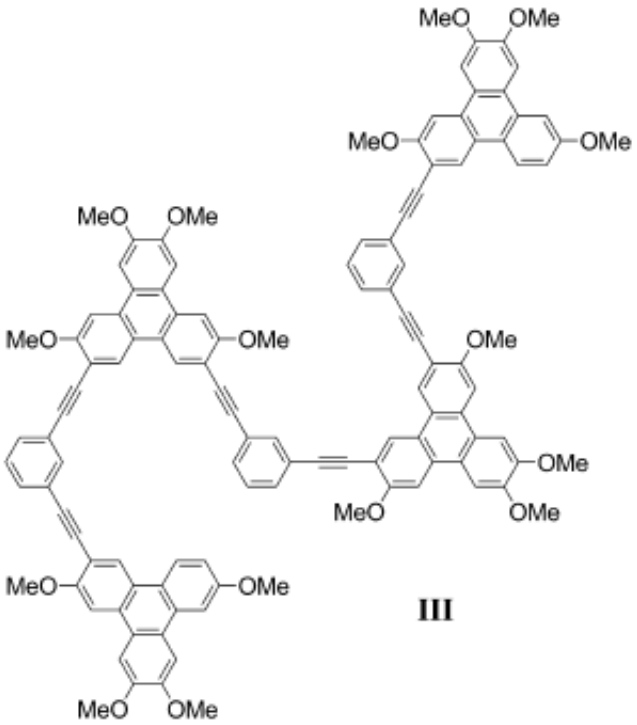

Figure 4.16. The structure of a model tetramer for molecular modeling studies.

In both gas phase and aqueous solution, calculations show that the conformations with triphenylene rings stacked are more stable than their coiled counterparts. There are two possible modes for triphenylene stacks, as shown in Figure 4.17. Interestingly, in gas phase the triphenylene rings favor a staggered orientation over an eclipsed orientation by 10.46 kJ/mol, whereas in aqueous solution the situation is reversed and the eclipsed orientation is favored by 3.39 kJ/mol. A breakdown of the potential energy of III in water is listed in Table 4.1. Apparently the solvation effect accounts for this difference in the lowest energy conformation. In gas phase the eclipsed conformation enjoys a slightly stronger dispersion interaction (Van der Waal energy), presumably due to a larger contact surface between two adjacent triphenylene rings, but incurs a much stronger electrostatic repulsion because of the close distance between the oxygen substituents, resulting in a higher potential energy (Figure 4.17). In aqueous solution, on the other hand, the aligned oxygen substituents of an eclipsed stacking maximize the solvation effect and compensates for the repulsion energy. This is an indication that the structure of polymers in solution is indeed under the combined influence of both the intramolecular forces and solvation effect.

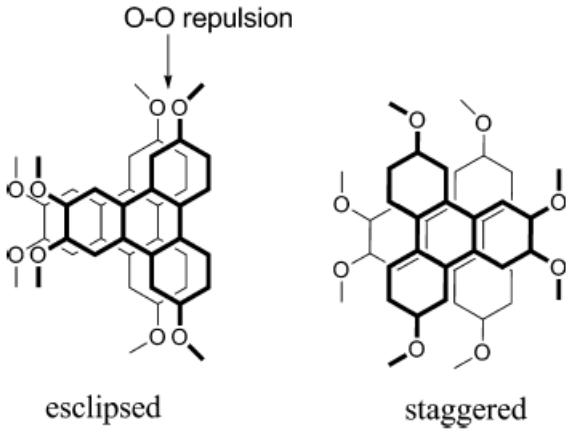

Figure 4.17. Eclipsed and staggered triphenylene stacking modes.

Table 4.1. Breakdown of III's potential energy (kJ/mole) in aqueous solution.

Orientation	Stretch energy	Bend energy	Torsional energy	Improper torsional energy
Staggered	75.23	173.27	15.74	0.30
Eclipsed	74.96	169.57	14.91	0.11

Orientation	Van del Waal energy	Electrostatic energy	Solvation energy	Total potential energy
Staggered	322.97	-142.11	-156.58	287.71
Eclipsed	317.67	-116.70	-176.21	284.32

For the optimized structure of III in water, the dihedral angle between the triphenylene plane and the adjacent phenyl plane is twisted in order to assume the triphenylene-stacked configuration (Figure 4.18). The triphenylene rings are parallel to each other with the interplane distance of 3.56 Å. Meanwhile, the bond angle of the acetylene linkage is also slightly bent to accommodate the parallel-displaced stacking. These distortions in the folding conformation presumably contribute to its blue-shifted emissions in comparison to that of interchain aggregated. According to the DFT calculation by Grimme, the parallel-displaced stacking of triphenylenes is typical for π–π interactions, and the interplane distance of our calculation agrees with that of tetracene dimer (3.314 Å) very well.

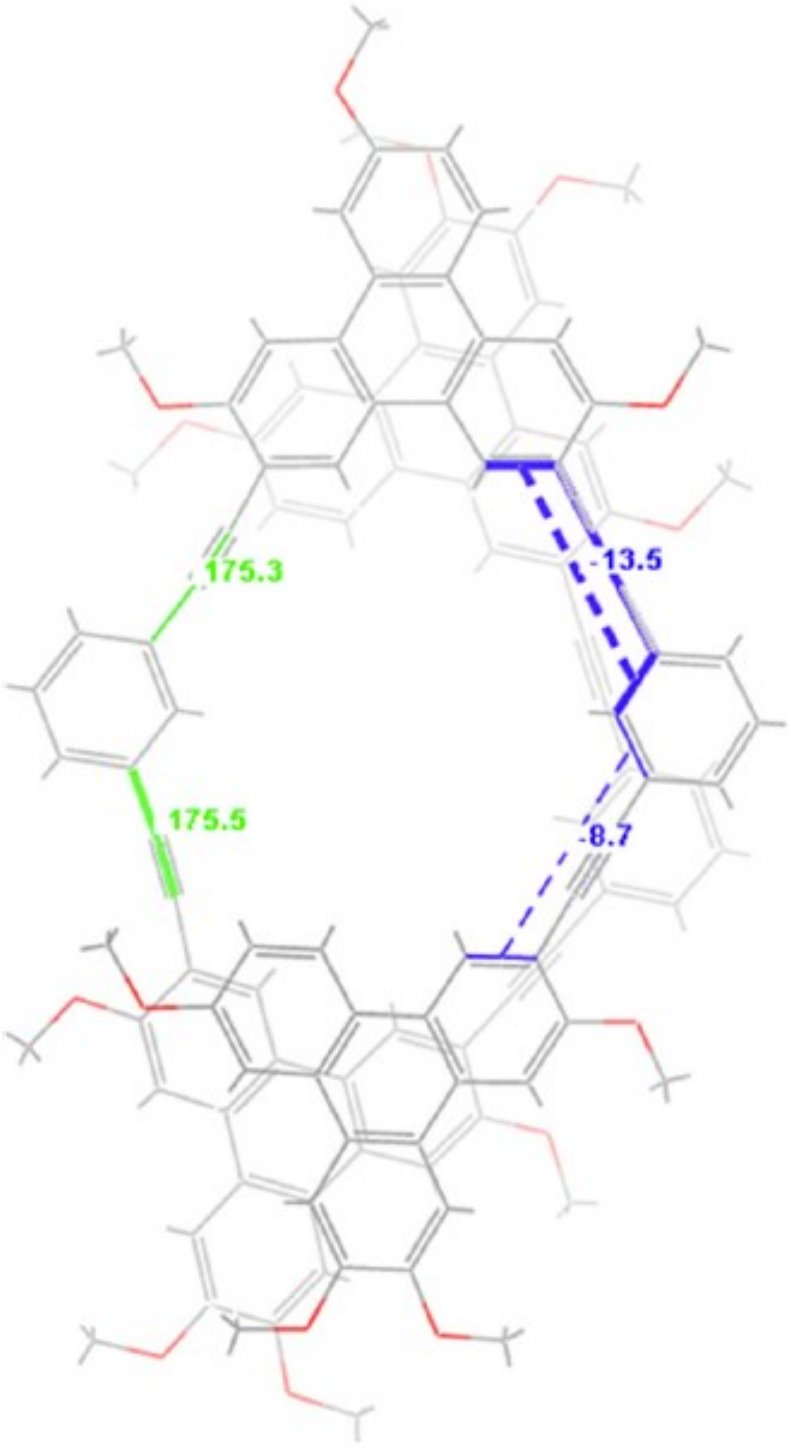

Figure 4.18. Lowest energy conformation of III in aqueous solution (green, bond angle; blue, dihedral angle).

It is worth noting that in other good solvents such as THF and benzene, mPPET shows similar foldamer-dominated emissions. When their solutions are diluted with acetonitrile, similar transition from 440 nm foldamer emission to 400 nm random coil emission and then to 490 nm aggregate emission is observed (Figure 4.19). If the dilution involves two good solvents, for example diluting a THF solution of mPPET with chloroform, no such transition is observed and the emission is always dominated by the folding conformation. It is particularly interesting to note that even benzene, a solvent known to significantly reduce π-stacking interactions, promotes folding of mPPET.[195] This may reflect again that the folding involves not so much of co-facial π-staking but rather some π–π interactions among twisted π-systems or even edge-to-face interactions.

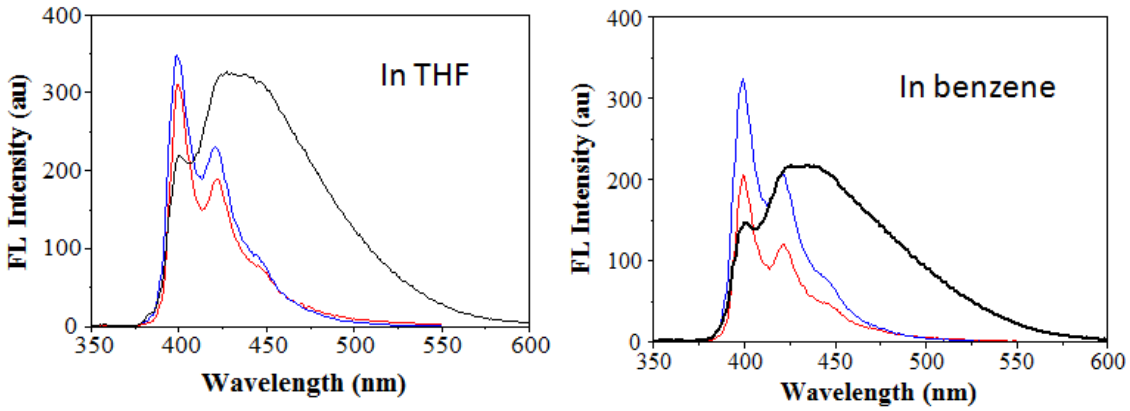

Figure 4.19. FL emission spectra of I (blue), II (red) and mPPET (black) in THF and benzene.

4.6 Conclusions

A new triphenylene-containing mPE polymer is synthesized. This polymer is found to fold into a helical conformation in a variety of solublizing solvents, but exhibit as interchain aggregates in poor solvents. In a solvent mixture containing a good solvent and a poor solvent in an appropriate ratio, the non-aggregating random coil conformation dominates. Among the three conformations, the folding conformation shows the highest fluorescence quantum yield. Due to the tight and abrupt turning, the co-facial-stacking of the π-systems (triphenylene and phenylene rings) is compromised. Nonetheless, mPPET still exhibits strong propensity for folding which is attributed to its bigger triphenylene π-system. Following the same approach, mPE polymers containing other even larger sized polycyclic aromatic structures may be synthesized which are expected to show even stronger folding propensity.

4.7 Experimental Section

General.

All the reactions were carried out under Nitrogen protection in flame-dried glassware. The solvents were used after fresh distillation over drying agents indicated and were transferred under nitrogen: THF (Na/benzophenone), CH_2Cl_2 (CaH_2). Compound **63** and **65** were prepared according to reported procedure.[187]

Instrumentation.

The ^1H and ^{13}C NMR spectra were recorded on a Varian INOVA 400 MHz FT NMR Spectrometer in the solvent indicated; chemical shifts (δ) are given in ppm relative to TMS, coupling constant (*J*) in Hz. The solvent signals were used as references[47] ($CDCl_3$: δ_C = 77.16 ppm; residual $CHCl_3$ in $CDCl_3$: δ_H = 7.26 ppm; Acetone-d6: δ_C = 206.26, 29.84 ppm; residual acetone in acetone-d6: δ_H = 2.05 ppm). UV-Vis absorption spectra were measured using a Hewlett-Packard 8452A Diode Array Spectrophotometer. Emission and excitation spectra were measured using a Shimadzu RF-5301PC Spectrofluorophotometer.

Compound I. Under a nitrogen atmosphere, 0.59 g of **63** (0.65 mmol), 0.46 g of 3 (1.63 mmol), 15 mg of $Pd(PPh_3)_4$ (0.026 mmol), 2.5 mg of CuI (0.026 mmol), 10 mL anhydrous toluene and 10mL anhydrous triethylamine were added to a round-bottom flask. The mixture was stirred at 60 ◦C under nitrogen for 24 h. After being cooled to room temperature, the mixture was filtered through Celite and the filtrate was stripped solvent. The resulting residue was recrystallized from dichloromethane/methanol to give a yellow solid. This crude product was dissolved in dichloromethane and to this solution

was added a solution of tetrabutylammonium fluoride (TBAF) in THF (1.3 mL, 1.0 M). The solution was stirred for 10 min, and then the solvent was evaporated. The crude product was purified by a short silica gel column chromatography eluting with ethyl acetate and hexane (1:3) to give a yellow solid (78%, m.p.: 138–141 ◦C). ^{1}H NMR ($CDCl_3$, 400 MHz, ppm): ı 8.54 (s, Ar-H, 2H), 7.83 (s, Ar-H, 2H), 7.79 (s, Ar-H, 2H), 7.68 (s, Ar-H, 2H), 7.63 (d, J = 9.2 Hz, Ar-H, 2H), 7.47 (d, J = 9.2 Hz, Ar-H, 2H), 7.37 (t, J = 7.8 Hz, Ar- H, 2H), 4.25 (t, J = 6.4 Hz, 4H), 4.14 (s, 6H), 3.12 (s, 2H), 1.94 (quintet, J = 7 Hz, 4H), 1.56 (quintet, J = 9 Hz, 4H), 1.27–1.43 (m, 16H), 0.88 (t, J = 6.8 Hz, 3H). ^{13}C NMR ($CDCl_3$, ppm): ı 158.0, 150.0, 135.2, 132.0, 131.8, 130.1, 128.7, 128.4, 124.4, 123.9, 122.4, 122.2, 112.0, 107.3, 103.0, 92.8, 87.0, 82.9, 69.6, 59.1, 56.1, 32.0, 29.8, 29.7, 29.6, 29.4, 26.0, 24.2, 22.2, 19.8, 14.2. Anal. calcd. for $C_{64}H_{72}O_4$: C, 84.91; H, 8.02. Found: C, 84.76; H, 8.13.

Compound II. Under a nitrogen atmosphere, 6 mg of $Pd(PPh_3)_2Cl_2$ and 3 mg of CuI were suspended in 20 mL anhydrous THF and 20 mL anhydrous diisopropylamine in a round-bottom flask. The suspension was heated up to 60 ◦C. 45.3 mg of compound **I** (0.05 mmol) and 45.4 mg of compound **63** (0.05 mmol) were dissolved in 20 mL anhydrous THF in a dropping funnel. The THF solution of reactants was added dropwise to the round-bottom flask over four days. After adding all reactants, the reaction was run at 80 ◦C under reflux for one more day. The reaction mixture was cooled down and then stripped solvent. The residue was dissolved in 30 mL dichloromethane and washed with 20 mL brine (3X) and 20 mL distilled water (3X). The organic phase was dried over anhydrous Na_2SO_4 and after filtration the solution was concentrated. The product was

purified by column chromatography using ethyl acetate as the eluent. After evaporating of solvent and drying under vacuum, 19 mg (25%) of the product was obtained as a yellow solid. ^{1}H NMR ($CDCl_3$, 400 MHz, ppm): δ 8.6 (b, weak), 6.4–8.4 (extremely broad, on top of the broad hump, signals at 7.6, 7.5, 7.4, 7.35 can be identified), 3.6–4.4 (extremely broad), 1.9 (b), 1.5 (b), 1.1 (b), 0.8 (b). Anal. calcd. for $C_{108}H_{132}O_8$: C, 83.25; H, 8.54. Found: C, 82.96; H, 8.47. MS (MALDI) calcd.: 1558.20, found: 1558.25.

mPPET. The mixture containing compound **63** (201.2 mg, 0.22 mmol), 1,3 diethynylbenzene (27.7 mg, 0.22 mmol), $Pd(PPh_3)_2Cl_2$ (12.7 mg, 0.011 mmol), and CuI (2.1 mg, 0.011 mmol) in anhydrous THF (2 mL) was stirred at 80 ◦C under nitrogen for 12 h. The dark brown solution was then filtered through a glass wool-stuffed pipette and the filtrate was dropped into methanol. The polymer precipitate was collected by filtration, washed with acetone, and dried under vacuum to give 137 mg of polymer (82%). ^{1}H NMR ($CDCl_3$, 400 MHz, ppm): δ 8.6 (b, weak), 6.2–8.6 (extremely broad, on top of the broad hump, signals at 7.6, 7.5, 7.4, 7.35 can be identified), 3.5–4.5 (extremely broad), 1.9 (b), 1.5 (b), 1.1 (b), 0.8 (b). ^{13}C NMR ($CDCl_3$, ppm): δ sharp signals observed at 132.0, 131.8, 128.7, 128.4, 31.9, 29.7, 26.2, 22.7, 14.1; and broad weak signals observed at 157.8, 134.2, 130.5, 124.0, 112.0, 106.0, 92.8, 69.8, and 55.2. Anal. calcd. for $C_{54}H_{66}O_4$: C, 83.25; H, 8.54. Found: C, 82.47; H, 8.14.

REFERENCES

1. Collings, P. J. Liquid Crystals, Nature's Delicate State of Matter. Princeton University, Press 1990.
2. Chan, C.; Crawford, G.; Gao, Y.; Hurt, R.; Jian, K.; Li, H.; Sheldon, B. Sousa; M.; Yang, N. *Carbon* **2005**, 43, 2431-2440.
3. Vorlander, D. *Ber. Dtsch. Chem. Ges.* **1907**, 40, 1970-1972.
4. Isihara, A. *J. Chem. Phys.* **1951**, 19, 1142-1147.
5. Brooks, G. H. T. *Carbon* **1965**, 3, 185-186.
6. Alben, R. *Phys. Rev. Lett.* **1973**, 30, 778-781.
7. Straley, J. P. *Phys. Rev. A* **1974**, 10, 1881-1887.
8. (a)J. Billard, J. C. D.; Huutinh, N.; Zann, A. Nouv. *J. Chim.* **1978**, 2, 535-540. (b)Levelut, A. M. *J. Phys. Lett.* **1979**, 40, L81-L84.
9. Kaafarani, B. R. *Chem. Mater.* **2011**, 23, 378-396.
10. Ohta, K.; Doonovan, K.; Sugibayashi, M.; Ariyoshi, M.; Ban, K.; Maeda, F.; Naito, R.; Nishizawa, K.; van de Craats, A. M.; Warman, J. M., *Mol. Cryst. Liq. Cryst.* **2003,** 397, 25-45.
11. (a) Schouten, P.G.; Warman, J.M.; de Haas, M. P.; Fox, M. A.; Pan, H.L. *Nature* **1991**, 353, 736-737; (b) Schouten, P.G.; Wenming, C.; Warman, J.M.; de Haas, M. P.; van der Pol, J.F.; Zwikker, J.W. *Synth. Met.* **1991**, 41-43, 2665-2668; (c) Schouten, P.G.; Warman, J.M.; de Haas, M. P.; van der Pol, J.F.; Zwikker, J.W. *J. Am. Chem. Soc.* **1992**, 114, 9028-9034; (d) Boden, N.; Borner, R.; Brown, D. R.; Bushby, R. J.; Clements, J. *Liq, Cryst.* **1992**, 11, 325-334; (e) Close, F.; Siemensmeyer, K. Frey, T.; Funhoff, D. *Liq, Cryst.* **1993**, 14, 629-634.

12. (a) Hennrich, G.; Cavero, E.; Barbera, J.; Gomez-Lor, B.; Hanes, R. E.; Talarico M.; Golemme, A.; Serrano, J. L. *Chem. Mater.* **2007**, 19, 6068-6070; (b) Zhang, Y.-D.; Jespersen, K. G.; Kempe, M.; Kornfield, J. A.; Barlow, S.; Kippelen, B.; Marder, S. R. *Langmuir* **2003**, 19, 6534–6536; (c) Meier, H.; Lehmann, M.; Holst, H. C.; Schwoppe, D. *Tetrahedron* **2004**, 60, 6881–6888.

13. Attias, A.-J.; Cavalli, C.; Donnio, B.; Guillon, D.; Hapiot, P.; Malthete, J. *Mol. Cryst. Liq. Cryst.* **2004**, 415, 169–177.

14. Ichihara, M.; Suzuki, H.; Mohr, B.; Ohta, K. *Liq. Cryst.* **2007**, 34, 401-410.

15. Roussel, O.; Kestemont, G.; Tant, J.; de Halleux, V.; Aspe, R. G.; Levin, J.; Remacle, A.; Gearba, I. R.; Ivanov, D.; Lehmann, M.; Geerts, Y. *Mol. Cryst. Liq. Cryst.* **2003**, 396, 35–39.

16. Kumar, S. (2010). *Chemistry of discotic liquid crystals: from monomers to polymers*. CRC PressI Llc.

17. Kastler, M.; Pisula, W.; Laquai, F.; Kumar, A.; Davies, R. J.; Baluschev, S.; Gutierrez, M. C. G.;Wasserfallen, D.; Butt, H. J.; Riekel, C.; Wegner, G.; Mullen, K. *Adv. Mater.* **2006**, 18, 2255-2259.

18. Hill, J. P.; Jin, W.; Kosaka, A.; Fukushima, T.; Ichihara, H.; Shimomura, T.; Ito, K.; Hashizume, T.; Ishii, N.; Aida, T. *Science* **2004**, *304*, 1481–1483.

19. Schmidt-Mende, L.; Fentenkötter, A.; Müllen, K.; Moons, E.; Friend, R. H.; MacKenzie, J. D.; *Science* **2001**, 293, 1119–1122.

20. Pisula, W.; Menon, A.; Stepputat, M.; Lieberwirth, I.; Kolb, U.; Tracz, A.; Sirringhaus, H.; Pakula, T.; Müllen, K. *Adv. Mater.* **2005**, *17*, 684–689.

21. Xiao, S.; Tang, J.; Beetz, T.; Guo, X.; Tremblay, N.; Siegrist, T.; Zhu, Y.; Steigerwald, M.; Nuckolls, C. *J. Am. Chem. Soc.* **2006**, *128*, 10700–10701.

22. Wong, W. W. H.; Ma, C.; Pisula, W.; Yan, C.; Feng, X., Jones, D. V.; Müllen, K.; Janssen, R. A. J.; Bauerle, P.; Holmes, A. B. *Chem. Mater.* **2010**, *22*, 457–466.

23. Jackel, F.; Watson, M. D.; Műllen, K.; Rabe, J. P. *Phys. Rev. Lett.* **2004**, *92*, 188303 1–4.

24. Horowitz, G. *Adv. Mater.* **1998**, *10*, 365–377.

25. Brabec, C. J.; Sariciftci, N. S.; Hummelen, J. C. *Adv. Funct. Mater.* **2001**, *11*, 15–26.

26. Lu, Y.; Moore, J. S. *Tetrahedron Lett.* **2009**, *50*, 4071–4077.

27. Müller, M.; Kübel, C.; Müllen, K. *Chem. – Eur. J.* **1998**, *4*, 2099–2109.

28. Alameddine, B.; Caba, S. M.; Schindler, M.; Jenny, T. A. *Sythesis* **2012**, 44, 1928–1934.

29. Miyaura, N.; Yamada, K.; Suzuki, A. *Tetrahedron lett.* **1979**, 20, 3437–3440.

30. Miyaura, N.; Suzuki, A. *Chem. Rev.* **1979**, 95, 2457–2483.

31. McOmie, J. F. W.; Watts, M. L.; West, D. E. *Tetrahedron* **1968**, 24, 2289–2292.

32. Lee, H.; Oh, J.; Chu, H. Y.; Lee, J. I.; Kim, S. H.; Yang, Y. S.; Kim, G. H.; Do, L. M.; Zyung, T.; Lee, J.; Park, Y. *Tetrahedron* **2003**, 59, 2773–2779.

33. Boden, N.; Bushby, R. J.; Cammidge, A. N.; Duckworth, S.; Headdock, G. *J. Mater. Chem.* **1997**, *7*, 601-605.

34. Boden, N.; Bushby, R. J.; Headdock, G.; Lozman, O. R.; Wood, A. *Liq. Cryst.* **2001**, *28*, 139-144.

35. Andersen, N. G.; Maddaford, S. P.; Keay, B. A. *J. Org. Chem.* **1996**, 61, 9556-9559.

36. Zang, Q.; Prins, P.; Jones, S. C.; Barlow, S.; Kondo, T.; An, Z.; Siebbeles, L. D.; Marder, S. R. *Org. Lett.* **2005**, *7*, 5019–5022.

37. Wadumethrige, S. H.; Rathore, R. *Org. Lett.* **2008**, *10*, 5139–5142.

38. King, B. T.; Kroulík, J.; Robertson, C. R.; Rempala, P.; Hilton, C. L.; Korinek, J. D.; Gortari, L. M. *J. Org. Chem.* **2007**, 72, 2279–2288.

39. Zhai, L.; Shukla, R.; Rathore, R. *Org. lett.* **2009**, 11, 3474–3477.

40. Clar, E. *Polycyclic Hydrocarbons Vol. 2*, Academic Press: London, **1964**, pp. 95–97, 283–284.

41. Clar, E.; Stewart, D. G. *J. Am. Chem. Soc.* **1952**, 74, 6235–6238.

42. Pisula, W.; Kastler, M.; Wasserfallen, D.; Pakula T.; Müllen, K. *J. Am. Chem. Soc.* **2004,** 126, 8074-8075.

43. (a) Laschat, S.; Baro, A.; Steinke, N.; Giesselmann, F.; Haegele, C.; Scalia, G.; Judele, R.; Kapatsina, E.; Sauer, S.; Schreivogel A.; Tosoni, M. *Angew. Chem., Int. Ed.* **2007**, 46, 4832-4887; (b) Zheng, H.; Lai, C. K.; Swager, T. M. *Chem. Matter.* 1995, **7**, 2067-2077; (c) Bushey, M. L.; Hwang, A.; Stephens P. W.; Nuckolls, C. *J. Am. Chem. Soc.* **2001**, 123, 8157-8158.

44. Hutter, J. L.; Bechhoefer, J. *J. Crystal Growth* **2000**, 217, 332-343.

45. Fürstner, A; Kennedy, J. W.J. *Chem. – Eur. J.* **2006**, 12, 7398–7410.

46. Gottlieb, H. E.; Kotlyar, V.; Nudelman, *J. Org. Chem.* **1997**, 62, 7512–7515.

47. Langhals, H. *Heterocycles* **1995**, 40, 477-500.

48. Forrest, S. R. *Nature* **2004**, 428,911-918.

49. Jurchescu, O. D.; Bass, J.; Palstra, T. T. M. *App. Phys. Let.* **2004**, 84, 3061-3063.

50. Podzorov, V.; Sysoev, S. E.; loginova, E.; Pudalov, V. M.; Gershenson, M. E. *App. Phys. Let.* **2003,** 83, 3504-3506.

51. Pisula, W.; Zorn, M.; Chang, J. Y.; Mullen, K.; Zental, R. *Opt. Quant. Electron.* **2009**, 41, 69-89.

52. Funahashi, M. *Polym. J. 2009*, 4, 459-469.

53. Sergeyev, S.; Pisula, W.; Geerts, Y. H. *Chem. Soc. Rev.* **2007**, 36, 1902–1929.

54. Monobe, H.; Kiyohara, K.; Terasara, N.; Heya. M.; Awazu, K.; Simishu, Y. *Adv. Funct. Mater.* **2003**, 13, 919-924.

55. Kumar, S. *Chem. Soc. Rev.* **2006**, 35, 83–109.

56. Li, Q. *Self-Organized Organic Semiconductors: From Materials to Device Applications* John Wiley & Sons: New York, **2011**.

57. Lever, L. J.; Kelsall, R. W.; Bushby, R. J. *Phys. Rev. B* **2005**, 72, 025130.

58. Eichhorn, E. H.; Adavelli, A.; Li, H. S.; Fox, N. *Mole. Cryst. Liq. Cryst.* **2003**, 397, 47-58.

59. Hatsusaka, K.; Ohta, K.; Yamamoto, I.; Shirai, H. *J. Mater. Chem*. **2001**, 11, 423-433.

60. Pisula, W.; Tomovic, Z.; Hamaoui, B. El; Watson, M. D.; Pakula, T.; Mullen, K. *Adv. Funct. Mater.* **2005**, 15, 893-904.

61. Vij, J. K.; Kocot, A.; Perova, T. S. *Mole. Cryst. Liq. Cryst.* **2003**, 397, 231-244.

62. Terasawa, N.; Monobe, H.; Kiyohara, K.; Shimizu, Y. *Chem. Commun.* **2003**, 1678-1679.

63. Zhou, X.; Kang, S. W.; Kumar, S.; Li, Q. *Liq. Cryst*. **2009**, 36, 269-274.

64. Grelet, E.; Bock, H. *Europhys. Lett.* **2006**, 73, 712-718.

65. Gearba, R. I.; Anokhin, D. V.; Bondar, A. I.; Bras, W.; Jahr, M.; Lehmann, M.; Ivanov, D. A. *Adv. Mater.* **2007**, 19, 815-820.

66. Charlet, E.; Grelet, E.; Brettes, P.; Bock, H.; Saadaoui, H.; Cisse, L.; Destruel, P.; Gherardi, N.; Seguy, I. *Appl. Phys. Lett.* **2008**, 92, 024107.

67. Steinhart, M. Zimmermann, S.; Goring, P.; Schaper, K.; Gosele, U.; Weder, C.; Wendorff, J. H. *Nano Lett.* **2005**, 5, 429-434.

68. Pouzet, E.; Cupere, V. D.; Heintz, C.; Andreasen, J. W.; Breiby, D. W.; Nielson, M. M.; Viville, P.; Lazzaroni, R.; Gbabode, G.; Geerts, Y. H. J. *Phys. Chem. C*. **2009**, 113, 14398-14406.

69. Zimmermann, S. Wendorff, J. H.; Weder, C. *Chem Mater.* **2002**, 14, 2218-2223.

70. Tracz, A.; Makowski, T.; Masirek, S.; Pisula, W.; Geerts, Y. H. *Nanotechnology* **2007**, 18, 485303.

71. Liu, C. Y.; Bard, A. J. *Chem. Mater.* **2010**, 12, 2353-2362.

72. Pisula, W.; Kastler, M.; Wasserfallen, D.; Pakula, T.; Mullen, K. *J. Am. Chem. Soc.* **2004**, 126, 8074-8075.

73. Mindyuk, O. Y.; Heiney, P. A. *Adv. Mater.* **1999**, 11, 341-344.

74. Smolenyak, P.; Peterson, R.; Nebesny, K.; Torker, M. *J. Am. Chem. Soc.* **1999**, 121, 8628-8636.

75. Reitzel, N.; Hassenkam, T.; Balashev, K.; Jensen, T. R.; Howes, P. B.; Kjaer, K.; Fechtenkotter, A.; Tchebotareva, S.; Ito, S.; Mullen, K. *Chem. Eur. J.* **2001**, 7, 4894-4901.

76. Benanti, T. L.; Venkataraman, D. *Photosynth. Res.* **2006**, 87, 73-81.

77. Tang, C. W. *App. Phys. Lett.* **1986**,48,183-185.

78. Yu, G.; Gao, J. C.; Hummelen, J. C.; Carroll, D. L. *Science* **1995**, 270, 1789-1791.

79. Gregg, B. A.; Fox, M. A.; Bard, A. J. *J. Phys. Chem.* **1990**, 94, 1586-1598.

80. Schmidt-Mende, L.; Fechtenkotter, A.; Mullen, K.; Moons, E.; Friend, R. H.; MacKenzie, J. D. *Science* **2001**, 293, 1119-1122.

81. Kang, S. J.; Ahn, S.; Kim, J. B.; Schenck, C.; Hiszpanski, A. M.; Oh, S.; Schiros, T.; Loo, Y. L.; Nuckolls, C. *J. Am. Chem. Soc.* **2013**, 135, 2207-2212.

82. Yamamoto, Y.; Fukushima, T.; Suna, Y.; Ishii, N.; Saeki, A.; Seki, S.; Tagawa, S.; Taniguchi, M.; Kawai, T.; Aida, T., *Science* **2006,** 314, 1761-1764.

83. Che, Y.; Yang, X.; Liu, G.; Yu, C.; Ji, H.; Zuo, J.; Zhao, J.; Zang, L. *J. Am. Chem. Soc.* **2010**, 132, 5743–5750.

84. Yamamoto, Y.; Zhang, G.; Jin, W.; Fukushima, T.; Ishii, N.; Saeki, A.; Seki, S.; Tagawa, S.; Minari, T.; Tsukagoshi, K.; Aida, T. *Proc. Natl. Acad. Sci.* U.S.A. **2009**, 106, 21051–21056.

85. Hizume, Y.; Tashiro, K.; Charvet, R.; Yamamoto, Y.; Saeki, A.; Seki, S.; Aida, T. *J. Am. Chem. Soc.* **2010**, *132*, 6628–6629.

86. Jiang, L.; Fu, Y.; Li, H.; Hu, W. *J. Am. Chem. Soc.* **2008**, *130*, 3937.

87. Luo, J.; Yan, Q.; Zhou, Y.; Li, T.; Zhu, N.; Bai, C.; Cao, Y.; Wang, J.; Pei, J.; Zhao, D. *Chem. Commun.* **2010**, *46*, 5725–5727.

88. Che, Y.; Huang, H.; Xu, M.; Zhang, C.; Bunes, B. R.; Yang, X.; Zang, L. *J. Am. Chem. Soc.* **2011**, *133*, 1087-1091.

89. Zang, L.; Che, Y.; Moore, J. S. *Acc. Chem. Res.* **2008**, *41*, 1596-1608.

90. Balakrishnan, K.; Datar, A.; Naddo, T.; Huang, J.; Oitker, R.; Yen, M.; Zhao, J.; Zang, L. *J. Am. Chem. Soc.* **2006**, *128*, 7390-7398.

91. Nguyen, L. H.; Hoppe, H.; Erb, T.; Günes, S.; Gobsch, G.; Sariciftci, N. S. *Adv. Funct. Mater.* **2007**, *17*, 1071-1078.

92. Datar, A.; Oitker, R.; Zang, L. *Chem. Commun. (Cambridge, U. K.)* **2006**, 1649-1651.

93. Dickey, K. C.; Anthony, J. E.; Loo, Y. L. *Adv. Mater.* **2006**, *18*, 1721-1726.

94. Lu, G.; Li, L.; Yang, X. *Small* **2008**, *4*, 601-606.

95. Chen, H.; Hu, S.; Zang, H.; Hu, B.; Dadmun, M. *Adv. Funct. Mater.* **2012**, 23, 1701-1710.

96. Chaudhuri, D.; Li, D.; Che, Y.; Shafran, E.; Gerton, J. M.; Zang, L.; Lupton, J. M. *Nano Lett.* **2011**, *11*, 488-492.

97. Che, Y.; Datar, A.; Yang, X.; Naddo, T.; Zhao, J.; Zang, L. *J. Am. Chem. Soc.* **2007**, *129*, 6354-6355.

98. Delgado, M. C. R.; Kim, E.-G.; Filho, D. t. A. d. S.; Bredas, J.-L. *J. Am. Chem. Soc.* **2010**, *132*, 3375-3387.

99. Coropceanu, V.; Cornil, J.; da Silva Filho, D. A.; Olivier, Y.; Silbey, R.; Brédas, J.-L. *Chem. Rev.* **2007**, *107*, 926-952.

100. Chua, L.-L.; Zaumseil, J.; Chang, J.-F.; Ou, E. C. W.; Ho, P. K. H.; Sirringhaus, H.; Friend, R. H. *Nature* **2005**, *434*, 194-199.

101. Yoon, M.-H.; Kim, C.; Facchetti, A.; Marks, T. J. *J. Am. Chem. Soc.* **2006**, *128*, 12851-12869.

102. Baeg, K.-J.; Facchetti, A.; Noh, Y.-Y. *J. Mater. Chem.* **2012**, *22*, 21138-21143.

103. Campoy-Quiles, M.; Ferenczi, T.; Agostinelli, T.; Etchegoin, P. G.; Kim, Y.; Anthopoulos, T. D.; Stavrinou, P. N.; Bradley, D. D. C.; Nelson, J. *Nat Mater* **2008**, *7*, 158-164.

104. (a) De Luca, G.; Liscio, A.; Battagliarin, G.; Chen, L.; Scolaro, L. M.; Mullen, K.; Samori, P.; Palermo, V. *Chem. Commun.* **2013**; (b) De Luca, G.; Liscio, A.; Maccagnani, P.; Nolde, F.; Palermo, V.; Müllen, K.; Samorì, P. *Adv. Funct. Mater.* **2007**, *17*, 3791-3798.

105. De Luca, G.; Liscio, A.; Nolde, F.; Scolaro, L. M.; Palermo, V.; Mullen, K.; Samori, P. *Soft Matter* **2008**, *4*, 2064-2070.

106. (a) Hoppe, H.; Sariciftci, N. S. *J. Mater. Chem.* **2006**, *16*, 45-61; (b) Kim, H. J.; Lee, H. H.; Kim, J.-J. *Macromolecular Rapid Communications* **2009**, *30*, 1269-1273; (c) Zhao, Y.; Xie, Z.; Qu, Y.; Geng, Y.; Wang, L. *Appl. Phys. Lett.* **2007**, *90*, 043504; (d) Bavel, S. S. v.; Sourty, E.; With, G. d.; Loos, J. *Nano. Lett.* **2008**, *9*, 507-513.

107. Hesse, H. C.; Weickert, J.; Al-Hussein, M.; Dössel, L.; Feng, X.; Müllen, K.; Schmidt-Mende, L. *Sol. Energ. Mat. Sol. Cells* **2010**, 94, 560-567.

108. (a) Berresheim, A. J.; Muller, M.; Mullen, K. *Chem. Rev.* **1999**, 99, 1747-1786; (b) Wu, J.; Pisula, W.; Mullen, K. *Chem. Rev.* **2007**, 107, 718-747. (c) Watson, M. D.; Fechtenkotter, A.; Mullern, K. *Chem. Rev.* **2001**, 101, 1267-1300. (d) Sarhan, A. A. O.; Bolm, C. *Chem. Soc. Rev.* **2009**, 38, 2730-2744.

109. Li, J.; Kastler, M; Pisula, W.; Roberson, J. W. F.; Wasserfallen, D.; Grimsdale, A. C.; Wu, J.; Mullen, K. *Adv. Funct. Mater*. **2007**, 17, 2528-2533.

110. Fischbach, I.; Ebert, F.; Spiess, H. W.; Schnell, I. *ChemPhsChem* **2004**, 5, 895-908.

111. Warman, J. M.; Piris, J., Pisula, W.; Kastler, M.; Wasserfallen, D.; Mullen, K. *J. Am. Chem. Soc.* **2005**, 127, 14257-14262.

112. Piot, L.; Marchenko, A.; Wu, J.; Mullen, K.; Fichou, D. *J. Am. Chem. Soc.* **2005**, 127, 16245-16250.

113. Piris, J.; Pisula, W.; Warman, J. M. *Synth. Met.* **2004**, 147, 85-59.

114. Kastler, M.; Pisula, W.; Wasserfallen, D.; Pakula, T.; Mullen, K. *J. Am. Chem. Soc.* **2005**, 127, 4286-4296.

115. Pisula, W.; Kastler, M.; Wasserfallen, D.; Davies, R. J.; Gutierrez, M. C. G.; Mullern, K. *J. Am. Chem. Soc.* **2006**, 128, 4424-14425.

116. Kirkpatrick, J.; Marcon, V.; Kremer, K.; Nelson, J.; Andrienko, D. J. *Chem. Phys.* **2008**, 129, 094506.

117. Marcon, V.; Vehoff, T.; Kirkpatrick, J.; Jenog, C.; Yoon, D. Y.; Kremer, K.; Andrienko, D. *J. Chem. Phys.* **2008**, 129, 094505.

118. Androenko, D.; Marcon, V.; Kremer, K.; *J. Chem. Phys.* **2006**, 125, 124902.

119. Clar. E.; Ironside, C. T. *Proc. Chem. Soc.* **1958**, 150-151.

120. Clar. E.; Ironside, C. T.; Zander, M. J. *Chem. Phys.* **1959**, 142-147.

121. Clar. E.; Stephen, J. F. *Tetrahedron* **1965**, 21, 467-470.

122. Hendel, W.; Khan, Z. H.; Schmidt, W. *Tetrahedron* **1986**, 42, 1127-1134.

123. Halleux, A.; Martin, R. H.; King, G. S. D. *Helv. Chim. Acta.* **1958**, 129, 1177-1183.

124. Herwig, P.; Kayser, C. W.; Muller, K.; Spiess, H. W. *Adv. Mater.* **1996**, 8. 510-513.

125. Weiss, K.; Beernink, G.; Dotz, F.; Birkner, A.; Mullen, K.; Woll, C. H. *Angew Chem. Int. Ed.* **1999**, 38, 3748-3752.

126. (a) Wadumethrige, S. H.; Rathore, R. *Org. Lett.,* **2008***,* 10, 5139-5142. (b) Frng, X.; Pisula, W.; Takase, M.; Dou, X.; Enkelmann, V.; Wagner, M.; Ding, N.; Mullen, K. *Chem. Mater.* **2008**, 20, 2872-2874.

127. van de Craats, A. M.; Warman, J. M.; Mullen, K.; Greets, Y.; Brand, J. D. *Adv. Mater.* **1998**, 10, 36-38.

128. Rakotonodradany, F.; Fenniri, H.; Rahimi, P.; Gawrys, K. L.; Kilpatric, P. K.; Gray, M. R. *Energy Fuels* **2006**, 20, 2439-2447.

129. Wadumethrige, S. H.; Rathore, R. *Org. Lett.* **2008**, 10, 5139-5142.

130. Fechtenkotter, A.; Tchebotareva, N.; Watson, M.; Mullen, K. *Tetrahedron* **2008**, 57, 3769-3783.

131. Grimsdale, A. C.; Bauer, R.; Weil, T.; Tchebotareva, N.; Wu, J.; Watson, M. D.; Mullen, K. *Synthesis* **2002**, 1229-1238.

132. Tchebotareva, N.; Yin, X.; Watson, M. D.; Samori, P.; Rabe, J. P.; Mullen, K. *J. Am. Chem. Soc.* **2003**, 125, 9734-9739.

133. Samori, P.; Yin, X.; Tchenotareva, N.; Wang, Z.; Pakula, T.; Jackel, F.; Watson, M. D.; Venturini, A.; Mullen, K.; Rabe. J. P. *J. Am. Chem. Soc.* **200**, 126, 3567-3575.

134. Mio, M. J.; Kopel, L. C.; Braun, J. B.; Gadzikwa, T. L.; Hull, K. L.; Brisbois, R. G.; Markworth, C. J.; Grieco, P. A. *Org. Lett.* **2002**, 4, 3199-3202.

135. Ito, S.; Wehmeier, M.; Brand, J. D.; Kubel, C.; Epsch, R.; Rabe, J. P.; Mullen, K. *Chem. Eur. J.* **2000**, 6, 4327-4342.

136. Cammidge, A. N.; Gopee, H. *J. P. P.* **2009**, 13, 235-246.

137. Ray, C.R.; Moore, J.S. *Adv. Polym. Sci.* **2005,** 177, 91-149.

138. Hill, D. J.; Mio, M. J.; Prince, R. B.; Hughes, T. S.; Moore, J. S. *Chem. Rev.* **2001**, 101, 3893-4012

139. (a) Goto, K.; Moore, J. S. *Org. Lett.* **2005**, 7, 1683-1686; (b) Prince, R. B.; Barnes, S. A.; Moore, J. S. *J. Am. Chem. Soc.* **2000**, 122, 2758-2762.

140. Sinkeldam, R. W.; Hoeben, F. J. M.; Pouderoijen, M. J.; De Cat, I.; Zhang, J.; Furukawa, S.; Feyter, S.D.; Vekemans, J. A. J. M.; Meijer, E. W. *J. Am. Chem. Soc.* **2006**, 128, 16113-16121.

141. Smaldone, R. A.; Moore, J. S. *J. Am. Chem. Soc.* **2007**, 129, 5444-5450.

142. Watson, M. D.; Fechtenkötter, A.; Müllen, K. *Chem. Rev.* **2001**, 101, 1267-1300.

143. (a) Jones, T. V.; Blatchly, R. A.; Tew, G. N. *Org. Lett.* **2003**, 5, 3297-3299; (b) Orita, K.; Alonso, E.; Yaruva, J.; Otera, J.; *Synlett* **2000**, 9, 1333-1335.

144. (a) Inouye, M.; Waki, M.; Abe, H. *J. Am. Chem. Soc.* **2004**, 126, 2022-2027; (b) Heemstra, J. M.; Moore, J. S. *Org. Lett.* **2004**, 6. 659-662.

145. Grimme, S. *Angew. Chem. Int. Ed.* **2008**, 47, 3430-3434.

146. Pauling, L.; Corey, R. B.; Branson, H. R. *Proc. Natl. Acad. Sci U.S.A.* **1951**, 378, 205-211.

147. Watson, J. D.; Crick, F. H. C. *Nature* **1953**, 171, 737-738.

148. Saenger, W. Principles of Nucleic Acid Structure; Springer-Verlag: New York, 1984.

149. Schulz, G. E.; Schirmer, R. H. Principles of Protein Structure; Springer-Verlag: New York, 1979.

150. Natta, G.; Pino, P.; Corradini, P.; Danusso, F.; Mantica, E.; Mazzanti, G.; Moraglio, G. *J. Am. Chem. Soc.* **1955**, 77, 1708-1710.

151. Tadokoro, H. Structure of Crystalline Polymers; Wiley: New York, 1979.

152. Pino, P.; Lorenzi, G. P. *J. Am. Chem. Soc.* **1960**, 82, 4745-4747.

153. Green, M. M.; Jha, S. K. *Chirality* **1997**, 9, 424-427.

154. Gomez-Lor, B.; Alonso, B.; Omenat, A.; Serrano, J. L. *Chem., Commun.,* **2006**, 5012-5014.

155. Bligin-Eran, B.; Tschierske, C.; Siegmar, D.; Baumeister, U. *J. Mater. Chem.* **2006**, 16, 1145-1153.

156. Achalkumar, A. S.; Yelamaggad, C. V. *Tetrahedron Lett.* **2007**, 53, 7108-7112.

157. Gihm, S. H.; Kim, B. G.; Kim, S.; Seo, J.; Park, S. Y.; Park, C. R. *J. Mol. Struct.*. **2010**, 984, 371-375.

158. Hayer, A.; De Halleux, V.; Koehler, A.; El-Garoughy, A.; Meijer, E. W.; Barbera, J.; Tant, J.; Levin, J.; Lehmann, M.; Gierschner, J.; Cornil, J.; Geerts,

Y. H. *J. Phys. Chem. B* **2006**, 110, 7653–7659.

159. (a) Chaudhuri, R.; Hsu, M.-Y.; Li, C.-W.; Wang, C.-I.; Chen, C.-J.; Lai, C. K.; Chen, L.-Y.; Liu, S.-H.; Wu, C.-C.; Liu, R.-S. *Org. Lett.* **2008**, 10, 3053–3056; (b) Kumar, S.; Varshney, S. K. *Mol. Cryst. Liq. Cryst.* **2002**, 378, 59–64.

160. Kumar, S.; Naidu, J. J.; Shankar Rao, D. S. *J. Mater. Chem.* **2002**, 12, 1335–1341.

161. Cristiano, R.; Gallardo, H.; Bortoluzzi, A. J.; Bechtold, I. H.; Campos, C. E. M.; Longo, R. L. *Chem. Commun.* **2008**, 5134–5136.

162. Yashima, E.; Maeda, K.; Lida, H.; Furusho, Y.; Nagai, K. *Chem. Rev.* **2009**, 109, 6102-6211.

163. Nolte, R. J. M.; Van Beijnen, A. J. M.; Drenth, W. *J. Am. Chem. Soc.* **1974**, 96, 5932-5933.

164. Okamoto, Y.; Suzuki, K.; Ohta, K.; Hatada, K.; Yuki, H. *J. Am. Chem. Soc.* **1979**, 101, 4763-4765.

165. Yuki, H.; Okamoto, Y.; Okamoto, I. *J. Am. Chem. Soc.* **1980**, 102, 6356-6358.

166. Corley, L. S.; Vogl, O. *Polym. Bull.* **1980**, 3, 211-217.

167. Ute, K.; Hirose, K.; Kashimoto, H.; Hatada, K.; Vogl, O. *J. Am. Chem. Soc.* **1991**, 113, 6305-6306.

168. Ute, K.; Hirose, K.; Kashimoto, H.; Nakayama, H.; Hatada, K.; Vogl, O. *Polym. J.* **1993**, 25, 1175-1186.

169. Green, M. M.; Andreola, C.; Munoz, B.; Reidy, M. P.; Zero, K. *J. Am. Chem. Soc.* **1988**, 110, 4063-4065.

170. Fujiki, M. Macromol. *Rapid Commun.* **2001**, 22, 539-563.

171. Yashima, E.; Maeda, K. Macromolecules 2008, 41, 3-12.

172. Yashima, E.; Maeda, K.; Furusho, Y. *Acc. Chem. Res.* **2008**, 41, 1166-1180.

173. Gellman, S. H. *Acc. Chem. Res.* **1998**, 31, 173-180.

174. Hamuro, Y.; Geib, S. J.; Hamilton, A. D. *J. Am. Chem. Soc.* **1996**, 118, 7529-7541.

175. Berl, V.; Huc, I.; Khoury, R. G.; Krische, M. J.; Lehn, J. M. *Nature* **2000**, 407, 720-723.

176. Nelson, J. C.; Saven, J. G.; Moore, J. S.; Wolynes, P. G. *Science* **1997**, 277, 1793-1796.

177. Moore, J. S. *Acc. Chem. Res.* **1997**, 30, 402-413.

178. Jones, T. V.; Slutsky, M. M.; Laos, R.; de Greef, T. F. A.; Tew, G. N. *J. Am. Chem. Soc.* **2005,** 127, 17235-17240.

179. (a) Dhar, R.; Kumar, S.; Gupta, M.; Agrawal, V. K. *J. Mol. Liq.* **2008**, 141, 19–24; (b) Bisoyi, H. K.; Kumar, S. *New J. Chem.* **2008**, 32, 1974–1980; (c) Murschell, A. E.; Sutherland, T. C. *Langmuir* **2010**, 26, 12859–12866.

180. Hou, J.-L.; Jia, M.-X.; Jiang, X.-K.; Li, Z.-T.; Chen, G.-J. *J. Org. Chem.* **2004**, 69, 6228-6237.

181. Negita, K.; Kawano, C.; Moriya, K. *Phys. Rev. E: Stat., Nonlinear, oft Matter Phys.* **2004**, 70, 021702/1–021702/5.

182. Crispin, X.; Cornil, J.; Friedlein, R.; Okudaira, K.K.; Lemaur, V.; Crispin, A.; Kestemont, G.; Lehmann, M.; Fahlman, M.; Lazzaroni, R.; Geerts, Y.; Wendin, G.; Ueno, N.; Brédas, J.-L.; Salaneck, W.R. *J. Am. Chem. Soc.* **2004**, 126, 11889-11899.

183. Warman, J. M.; de Haas, M. P.; Dicker, G.; Grozema, F. C.; Piris, J.; Debije, M. G.; *Chem. Mater.* **2004**, 16, 4600-4609.

184. Jaiswal, M.; Menon, R. *Polym. Int.* **2006**, 55, 1371-1384.

185. Cross, S. J.; Goodby, J. W.; Hall, A. W.; Hird, M.; Kelly, S. M.; Toyne, K. J.; Wu, C. *Liq. Cryst.* **1998**, 25, 1-11.

186. Adam, D.; Schuhmacher, P.; Simmerer, J.; Haussling, L.; Siemensmeyer, K.; Etzbach, K. H.; Rinsdorf, H.; Haarer, D. *Nature* **1994**, 371, 141-143.

187. Wang, D.; Hsu, J. F.; Bagui, M.; Dusevich, V.; Wang, Y.; Liu, Y.; Holder, A. J.; Peng, Z. *Tetrahefron Lett.* **2009**, 18, 2147-2149.

188. Lahiri, S.; Thompson, J. L.; Moore, J. S. *J. Am. Chem. Soc.* **2000**, 122, 11315-11319.

189. (a) Ahn, T. S.; Thompson, A. L.; Bharathi, P.; Muller, A.; Bardeen, C. J. *J. Phys. Chem. B* 2006, 110, 19810-19819; (b) Ranasinghe, M. I.; Hager, M. W.; Gorman, C. B.; Goodson III, T. *J. Phys. Chem. B* **2004**, 108, 8543-8549.

190. (a) Höger, S. *Chem. Eur. J.* **2004**, 10, 1320-1329; (b) Kahr, M.; Xu, Z.; Walker, K. L.; Wilkins, C. L.; Moore, J. S. *J. Am. Chem. Soc.* **1994**, 116, 4537-4550.

191. Wang, D.; Hsu, J.; Bagui, M.; Dusevich, V.; Wang, Y.; Liu, Y.; Holder, A. J.; Peng, Z. *Tetrahedron Lett*. **2009**, 50, 2147-2149.

192. Jorgensen, W. L.; Tirado-Rives, J. *J. Am. Chem. Soc.* **1988**, 110, 1657-1666.

193. Kaminski, G. *J. Phys. Chem. B* **2001**, 105, 6474-6487.

194. Maestro 8.5, Schrodinger, LLC: Portland. https://www.schrodinger.com.

195. Prince, R. B.; Saven, J. G.; Wolynes, P. G.; Moore, J. S. *J. Am. Chem. Soc.*

1999, 121, 3114-3121.

196. van der Beek, D.; Petukhov, A. V.; Davidson, P.; Ferré, J.; Jamet, J. P.; Wensink, H. H.; Vroege, G. J.; Bras, W.;Lekkerkerker H. N. W. Phys. Rev. E **2006**, 73, 041402.

197. (a) Luo, J.; Zhao, B.; Shao, J.; Lim, K. A.; Chan, H. S. O.; Chi, C. *J. Mater. Chem.* **2009**, 19, 8327–8334; (b) Talarico, M.; Termine, R.; Garcia-Frutos, E. M.; Omenat, A.; Serrano, J. L.; Gomez-Lor, B.; Golemme, A. *Chem. Mater.* **2008**, 20, 6589–6591.

198. (a) Kadam, J.; Faul, C. F. J.; Scherf, U. *Chem. Mater.* **2004**, 16, 3867–3871; (b) Boden, N.; Bushby, R. J.; Donovan, K.; Liu, Q.; Lu, Z.; Kreouzis, T.; Wood, A. *Liq. Cryst*. **2001**, 28, 1739–1748.

199. (a) Ong, C. W.; Liao, S.-C.; Chang, T. H.; Hsu, H.-F. *Tetrahedron Lett.* **2003**, 44, 1477–1480; (b) Lehmann, M.; Kestemont, G.; Aspe, R. G.; Buess-Herman, C.; Koch, M. H. J.; Debije, M. G.; Piris, J.; de Haas, M. P.; Warman, J. M.; Watson, M. D.; Lemaur, V.; Cornil, J.; Geerts, Y. H.; Gearba, R.; Ivanov, D. A. *Chem.;Eur. J.* **2005**, 11, 3349–3362.

200. An, Z.; Yu, J.; Domercq, B.; Jones, S. C.; Barlow, S.; Kippelen, B.; Marder, S. R. *J. Mater. Chem.* **2009**, 19, 6688–6698.

201. (a) Deibel, C.; Janssen, D.; Heremans, P.; De Cupere, V.; Geerts, Y.; Benkhedir, M. L.; Adriaenssens, G. *J. Org. Electron.* **2006**, 7, 495–499; (b) Sergeyev, S.; Debever, O.; Pouzet, E.; Geerts, Y. H. *J. Mater. Chem.* **2007**, 17, 3002–3007; (c) Kimura, M.; Narikawa, H.; Ohta, K.; Hanabusa, K.; Shirai, H.; Kobayashi, N. *Chem. Mater.* **2002**, 14, 2711–2717; (d) Miao, J.; Zhu, L.

Soft Matter. **2010**, 6, 2072–2079.

202. (a) Kroeze, J. E.; Koehorst, R. B. M.; Savenije, T. J. *Adv. Funct. Mater.* **2004**, 14, 992–998; (b) Qi, M.-H.; Liu, G.-F. *J. Mater. Chem.* **2003**, 13, 2479–2484.

VITA

Ching-En Chou was born on Nomember 23, 1980 in Taipei, Taiwan, where he attended elementary, middle school, high school and college. He interest in chemistry was enlightened by the topic of Octet rule in the chemistry course during high school. In 1999, Ching-En got the addmission from Tamkang University, Taiwan where he chose the Chemical and Material Engineering as his major. He received his bachloar's degree in 2003. In order to explore and challenge the profound chemistry, he joined the Chemistry Department of University of Missouri-Kansas City for his Ph.D. study in January 2007, and joined Prof. Peng's research labortory in end of May 2007.

During his Ph.D. study in Prof. Peng's group, he has devoted in the research on the foldable polymers, mainly tribenzophentaphene derivatives and triphenylene polymers. He received Graduate Student Travel Award in 2013 and served as a volunteer in 245th ACS National Meeting, in New Orleans, Louisiana. The list of publication which he had co-authored and the list of presentations at various regional and national conferences are shown below.

PUBLICATIONS

- Morphology control of nanofibril donor-acceptor heterojunction to achieve high photoconductivity: exploration of new molecular design rules, **Chou, Ching-En**; Huang, Heling; Che, Yanke; Ligui Li, Chen Wang, Xiaomei YangPeng, Zhonghua*; Zhang, Ling* *Journal of the American Chemistry Society* **2013**, 135, 16490-16496.

- Synthesis, Self-assembly and Applications of Tribenzopentaphene Derivatives, **Chou, Ching-En**; Li, Yong.; Che, Yanke; Zhang, Ling; Peng, Zhonghua* *RSC Advances* **2013**, 3, 20666-20672.

- Synthesis and optical properties of triphenylene-coating conjugated polymer. **Chou, Ching-En**; Wang, Degang; Bagui, Mahuya; Hsu, Charkraborty, Sanjiban; Jeffery; Peng, Zhonghua* *Journal of Luminescence* **2010**, 130, 986–994.

- Synthesis and optical properties of poly(2,11-triphenyleneethynylene-*alt*-m-phenyleneethynylene)s. **Chou, Ching-En**; Wang, Degang; Hsu, Jeffery; Liu, Yi; Peng, Zhonghua* *Synthetic Metal* **2009**, 159, 1657-1663.

ORAL AND POSTER PRESENTATIONS

- **Chou, Ching-En**; Wang, Degang; Hsu, Jeffery; Liu, Yi; Peng, Zhonghua. 'Synthesis and Optical properties of Poly(2,11-triphenyleneethynylene-alt-m-phenyleneethynylene)s'. **44th Midwest regional meeting of the American Chemical Society, Iowa City, IA, October 21-24 2009.**

- **Chou, Ching-En**; Li, Shaohua; Dutta, Tanmoy; Peng, Zhonghua. 'Conjugated foldamers based on Polycyclic aromatic hydrocarbons'. **45th Midwest regional meeting of the American Chemical Society. Wichita, KS, October 27-30 2010.**

- **Chou, Ching-En**; Li, Yong; Che, Yanke; Zang, Ling; Peng, Zhonghua. 'Synthesis and Applications of Tribenzopentaphene Derivatives'. **47th Midwest regional meeting of the American Chemical Society, Omaha, NE, October 24-26 2012.**

- **Chou, Ching-En**; Li, Yong.; Che, Yanke; Zang, Ling Peng, Zhonghua. 'Synthesis, self-assembly, and applications of tribenzopentaphene derivatives'. **ACS 245th National Meeting of American Chemical Society in New Orleans, LA, April 7-11 2013.**

- **Chou, Ching-En**; Che, Yanke; Zang, Ling; Peng, Zhonghua. Synthesis, self-assembly, and application of diphenyl tribenzopentaphene derivatives**. 48th Midwest regional meeting of the American Chemical Society, Springfield, MO, October 16-19, 2013**.